SYNTHESIS AND CHARACTERIZATION OF POLYCRYSTALLINE SEMICONDUCTOR $CsSnI_3$ THIN-FILMS

by

ZHUO CHEN

A dissertation submitted to the Graduate Faculty in Physics in partial fulfillment of the requirements for the degree of Doctor of Philosophy, The City University of New York

2013

This manuscript has been read and accepted by the
Graduate Faculty in Physics in satisfaction of the
dissertation requirement for the degree of Doctor of Philosophy.

Date
Dr. Kai Shum
Chair of Examining Committee

Date
Dr. Steven Greenbaum
Executive Officer

Dr. Gregory S. Boutis

Dr. Micha Tomkiewicz

Dr. Mim Nakarmi

Dr. Shi Jin

Dr. Jian J. Wang

Supervision Committee

THE CITY UNIVERSITY OF NEW YORK

ABSTRACT

SYNTHESIS AND CHARACTERIZATION OF POLYCRYSTALLINE SEMICONDUCTOR $CsSnI_3$ THIN-FILMS

by

Zhuo Chen

Advisor: Kai Shum

This thesis deals with a virtually unexplored semiconductor material $CsSnI_3$ from material synthesis, structural, optical, and electrical characterization to the fabrication and validation of $CsSnI_3$ thin-film solar cells.

We started with synthesizing $CsSnI_3$ thin films based on CsI and $SnCl_2$ (or SnI_2) by using an apparatus which consists of e-beam and thermal evaporators. The quality of polycrystalline $CsSnI_3$ thin-films were studied by scanning electron microscopy (SEM), transmission electron microscopy (TEM), and X-ray diffraction (XRD). Experimental data on XRD and electron diffraction patterns taking from the synthesized thin-films match very well to the theoretically calculated ones based the first principles calculations, confirming that the synthesized $CsSnI_3$ thin-films have an orthorhombic crystal structure. With the well-defined crystal structure, we theoretically studied the electronic band structure of $CsSnI_3$. Extensive optical characterizations of $CsSnI_3$ thin-films were then carried out revealing many extraordinary properties such as 1)

direct band gap energy of 1.32 eV at 300 K with its abnormal temperature dependence, 2) extremely high photoluminescence quantum yield, 3) large exciton binding energy, and 4) strong two-phonon assisted excitonic absorption near band edge. These properties are interpreted in terms of the unique electronic and structural properties of $CsSnI_3$.

The value of 1.3 eV for the energy band gap of $CsSnI_3$ suggests a unique application of $CsSnI_3$ thin-films on solar cells. This is because this value is right in the small range of the optimal band gaps for the Shockley-Queisser maximum efficiency limit of a single-junction solar cell. A prototype Schottky solar cell was designed, fabricated, and validated. The measured power conversion efficiency (PCE) is 0.9 % which is presently limited by the series and shunt resistance. The improvement strategy on PCE is given at the end of my thesis.

In order to make the $CsSnI_3$ thin-film solar cells cost effective, various low cost materials synthesis methods for $CsSnI_3$ are also described in this thesis. $CsSnI_3$ thin-films can be now inexpensively deposited on to glass or other low-cost substrates. I believe that the $CsSnI_3$ based materials are ideally suited for many applications such as lasers, light-emitting diodes, integrated photonic devices such as infrared electro-optic modulator, solar cells, and even more specialized applications such as spectral solar concentrators.

ACKNOWLEDGEMENTS

I would like to thank Professor Kai Shum for his patience and understanding in guiding me throughout my PhD thesis work at The City University of New York. Thanks are specially to be given to my parents for their support in achieving my goals. I would also extend my appreciations to Jian J. Wang, Tom Salagaj, Jawad Qureshi, Piao Liu, and Chonglong Yu for their professional helps.

TABLE OF CONTENTS

LIST OF FIGURES

CHAPTER 1

CHAPTER 2

CHAPTER 3

CHAPTER 4

CHAPTER 5

CHAPTER 6

CHAPTER 7

CHAPTER 8

CHAPTER 9

CHAPTER 10

LIST OF TABLES

CHAPTER 2

CHAPTER 3

LIST OF EQUATIONS

CHAPTER 3

CHAPTER 4

CHAPTER 7

CHAPTER 8

CHAPTER 1: Introduction

1.1 Motivation

While a majority of the world's current electricity supply is generated from fossil fuels such as coal, oil and natural gas, these traditional energy sources face a number of challenges including rising prices, security concerns over dependence on imports from a limited number of countries which have significant fossil fuel supplies, and growing environmental concerns over the climate change risks associated with power generation using fossil fuels. As a result of these and other challenges facing traditional energy sources, governments, businesses and consumers are increasingly supporting the development of alternative energy sources and new technologies for electricity generation. Renewable energy sources such as solar, biomass, geothermal, hydroelectric and wind power generation have emerged as potential alternatives which address some of these concerns. As opposed to fossil fuels, which draw on finite resources that may eventually become too expensive to retrieve, renewable energy sources are generally unlimited in availability.

Solar power generation has emerged as one of the most rapidly growing renewable sources of electricity. Solar power generation has several advantages over other forms of electricity generation:

Reduced dependence on fossil fuels - Solar energy production does not require fossil fuels and is therefore less dependent on this limited and expensive natural resource. Although there is variability in the amount and timing of sunlight over the day, season and year, a properly sized and configured system can be designed to be highly reliable while providing long-term, fixed price electricity supply.

Environmental advantages - Solar power production generates electricity with a limited impact on the environment as compared to other forms of electricity production.

Modularity and scalability - As the size and generating capacity of a solar system are a function of the number of solar modules installed; applications of solar technology are readily scalable and versatile.

Flexible locations - Solar power production facilities can be installed at the customer site which reduces required investments in production and transportation infrastructure.

Government incentives - A growing number of countries have established incentive programs for the development of solar and other renewable energy sources, such as (i) net metering laws that allow on-grid end users to sell electricity back to the grid at retail prices, (ii) direct subsidies to end users to offset costs of photovoltaic (PV) equipment and installation charges, (iii) low interest loans for financing solar power systems and tax incentives; and (iv) government standards that mandate minimum usage levels of renewable energy sources.

Despite the cost, another advantage of photovoltaic systems is that they can be used in remote areas. Anywhere a diesel generator is the technology of choice, many times a photovoltaic system is a much better life-cycle cost option.

Stand-alone photovoltaic systems produce power independently of the utility grid. In some off-the-grid locations even one half kilometer from power lines, stand-alone photovoltaic systems can be more cost-effective than extending power lines. They are especially appropriate for remote, environmentally sensitive areas, such as national parks, cabins, and remote homes.

The solar power market has grown significantly in the past decade. Solar cell generated power will account for 3.6% of installed power generation globally by 2020, according to market analyst and advisor, Frost & Sullivan's Annual Renewable Outlook 2013. Solar PV's share in total installed power generation globally was 0.7% in 2010; it is predicted to reach 2.4% by 2015 and 3.6% by 2020. PV's annual growth rate will also continue to overtake other renewable energies in installed capacity, with the report also predicting that solar PV installations will account for 10.9% of all renewable energy production by 2020.

Efficiency versus cost is the trade-off that bedevils researchers and developers of solar cells. Multi-junction photovoltaic cells are good at absorbing photons and converting them to electricity, but they cost a lot to fabricate, not suitable for terrestrial use. In contrast, crystalline silicon cells are much cheaper, but efficiency is relatively low due to the low band gap. The semiconductor chosen for a solar cell has to absorb as many photons as possible in the full solar spectrum; therefore a low band gap is desirable. However, this is counter-balanced by the desire to have as large a built-in voltage as possible which requires a large band gap. The Shockley Queisser (SQ) Limit refers to the maximum theoretical efficiency of a perfect solar cell using a single p-n junction to extract electrical power.[1] It was first calculated by William Shockley and Hans Queisser in 1961. A solar cell's energy conversion efficiency is the percentage of power converted from sunlight to electrical energy under "standard test conditions" (STC). The STC conditions approximate solar noon at the spring and autumn equinoxes in the continental United States with the surface of the solar cell aimed directly at the sun. The modern SQ Limit calculation is a maximum efficiency of 33% for any type of single junction solar cell. Current solar cell production efficiencies vary by the band gap of the semiconductor material as shown below.

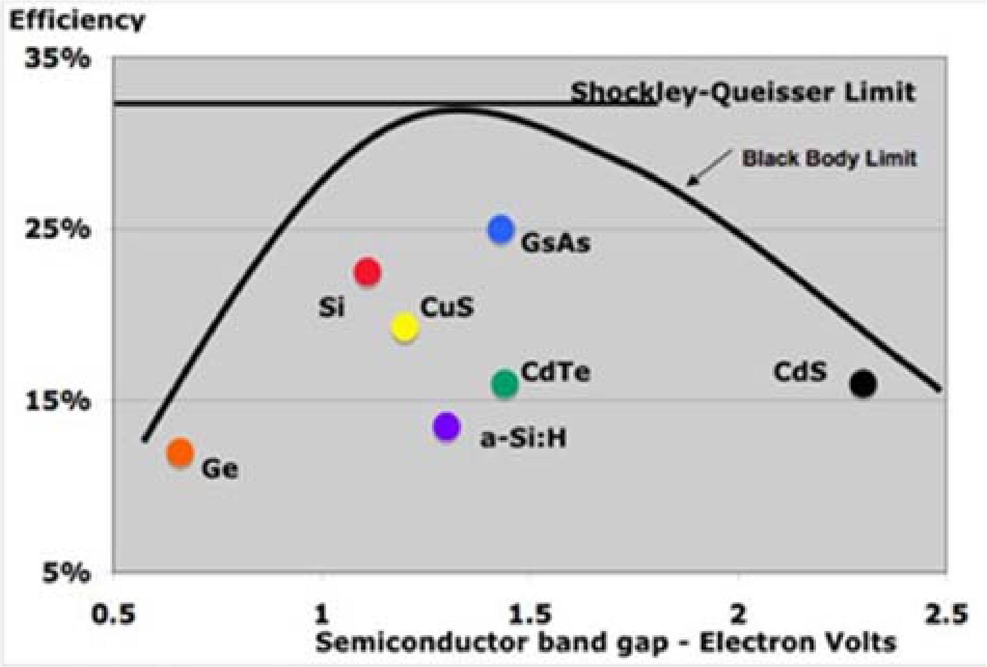

Figure 1.1: Shockley–Queisser limit: Maximum PV efficiency in theory vs. semiconductor band gap.

From Figure 1.1, we can see that the optimal band gap is between 1.3 and 1.35 eV. Thin-film solar cells are candidates for large-volume and low-cost production for industrial-scale power generation in the megawatt to gigawatt capacity range since the consumption of raw materials is reduced and the manufacturing processes are relative simple. High quality photovoltaic materials are essential for thin-film solar cell.

By surveying a group of raw materials for potential photovoltaic applications, our group found a perovskite material – $CsSnI_3$. It was confirmed that $CsSnI_3$ possesses a direct band-gap of 1.32 eV at room temperature by optical spectroscopic methods and by first principles calculations.

1.2 Background on CsSnI$_3$

An early study on the structural information of CsSnI$_3$ compound in form of powders was reported by Scaife *et al*[2] in 1974. A few years later, a yellow, needle-like CsSnI$_3$ microcrystal was synthesized and its crystal structure was independently studied by Mauersberger and Huber.[3] No additional information was available until the discovery of another polymorph of this compound in 1991 by Yamada et al.[4] This polymorph was named as black CsSnI$_3$ since it had a lustrous black color. They found that the black polymorph of CsSnI$_3$ could be obtained through a sequential phase transitions from the yellow CsSnI$_3$ by decreasing its temperature from 425 K. It was further demonstrated by differential thermal analysis and X-ray diffraction that during the cooling of the black CsSnI$_3$ from 450 K, its ideal cubic perovskite structure (B-α) deformed to a tetragonal structure (B-β) at 426 K, and became an orthorhombic structure (B-γ) below 351 K. Experimental studies of electrical and optical properties of this compound have been hindered by lack of high quality CsSnI$_3$ samples either in bulk or thin film format. Only recently, aiming at the unique properties of hybrid organic-inorganic perovskite based on tin halides, Borriello et al.[5] calculated band structures of B-α, B-β, and B-γ from the first principles using the crystal structures published by Yamada et al.[4] It was concluded that all three structures had direct band gap (E_g) at Z, R, and Γ points for B-α, B-β, and B-γ, respectively, with E_g (B-α) < E_g (B-β) < Eg (B-γ).

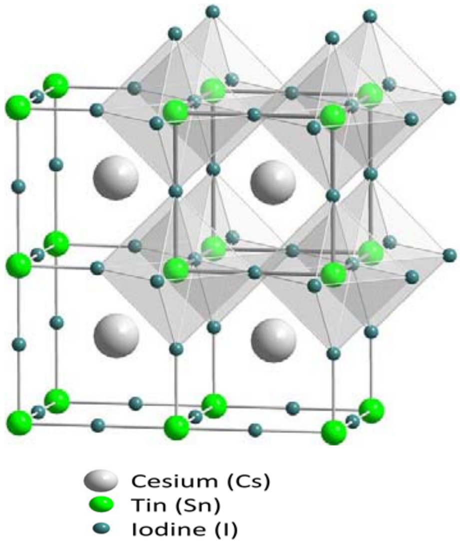

Figure 1.2: Schematic crystal structure of perovskite semiconductor CsSnI$_3$.

CHAPTER 2: Crystal and Band Structure of $CsSnI_3$

Quantum simulation method was employed to determine the equilibrium crystal structure at 0 K and its associated electronic band structure. All the calculations were performed with the CASTEP simulation tool,[6] which is based on the density function theory. The Perdew−Burke−Ernzerhof (PBE) parameterization of the generalized gradient approximation (GGA) was employed and core-valence electron interactions were described using the Troullier-Martin norm-conserving pseudo-potentials.[7] The cutoff for the plane wave basis was 400 eV and a 3 × 3 × 2 Monkhorst-Pack grid was chosen for sampling the Brillouin Zone.

2.1 Determination of γ crystal structure

The PNAM crystal group for $CsSnI_3$ has 10 degrees[8] of freedom with 7 of the freedoms represented by the fractional coordinates in Table 2.1.

Atom	Position	x	y	z
Cs	4c(m)	CsX	CsY	0.25
Sn	$4b(\bar{1})$	0	0	0.5
I1	4c(m)	I1X	I1Y	0.25
I2	8d(1)	I2X	I2Y	I2Z

Table 2.1: The fractional coordinates for the four atomic groups in $CsSnI_3$.

These include two degrees of freedom for the Cs-offset (CsX, CsY), two degrees of freedom for the Iodine group (with 2 atoms at z = 0.25 and 2 atoms at z = 0.75), (I1X, I1Y) and three for the Iodine group in the near-xy plane (I2X, I2Y, I2Z) (with 4 atoms near z = 0.0 and 4 atoms near z = 0.5). The values of I1X, I1Y, I2X, I2Y, and I2Z depend on the relative tilts of the underlying octahedrons shown in Figure 2.1. The lattice constants in the x, y, and z directions complete the ten freedoms.

The basic structure within the crystal is an octahedron structure represented by SnI_6. The tin atom sits at the center of the octahedron and the iodine atoms are at the six vertices. To simplify the structure, we assume that internal angles of two neighboring Iodine with the tin at center is 90^o. This is shown in Figure 2.1.

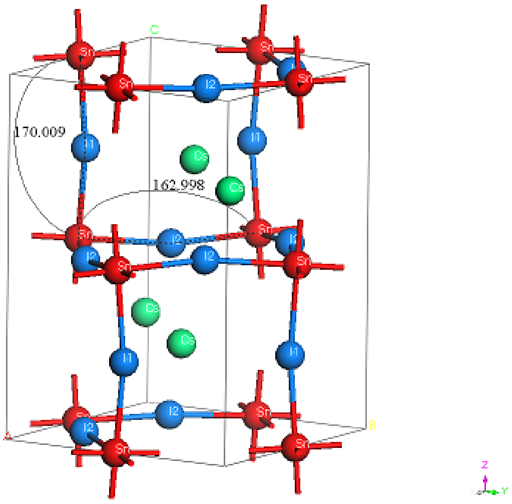

Figure 2.1: Calculated $CsSnI_3$ unit cell with 20-atom orthorhombic structure. I-Sn-I angles are 90^o. Here Sn-I-Sn angle θ_{XY} is 163^o and θ_Z is 170^o.

This simplifies that problem leading to only 5 degrees of freedom; a lattice scaling factor, the angles θ_{XY} and θ_Z, (Sn-I-Sn angle in the near-xy plane for the I2 group and Sn-I-Sn angel on the z axis for the I1 group as shown in Figure 2.1), and Cs-offset (CsX, CsY). Rather than relying on energy minimization algorithm with the 5 degrees of freedom, we attempted energy minimization by the following technique. First, for a particular set of θ_{XY} and θ_Z values, we found the lattice scaling factor, assuming zero Cs-offset, in minimum energy procedure. Once we found the lattice scaling factor (in a one-dimensional calculation), we changed the Cs-offset (in a 2-dimensional calculation) to find a new minimum energy. We also assume that Cs atoms act as a small perturbation with the larger energy contribution due to the lattice size. It should be understood that even though there are three lattice constants, after all the angles are fixed we end up with one scaling factor. This minimum energy, found after the two procedures, yields the value of E (θ_{xy}, θ_z). The plot of this energy as a function of angle combinations is shown in Figure 2.2.

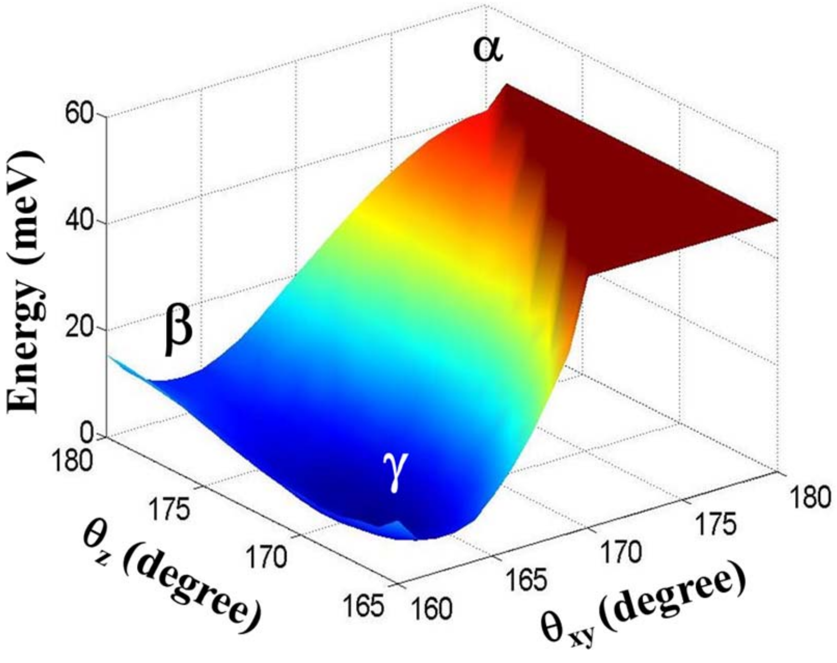

Figure 2.2: Energy landscape plotted as the Sn-I-Sn bond angles of θ_{XY} and θ_Z. It shows the values of θ_{XY} and θ_Z at which the crystal has a minimum total energy and also demonstrates how the total crystal energy changes as θ_{XY} and θ_Z are varied.

2.2 Band Structure of $CsSnI_3$

The band structure of $CsSnI_3$ based on the energy-minimized structural coordinates is shown in Figure 2.3. Three salient features of the electronic states near the band edges should be pointed out. First, it is clearly a direct band-gap semiconductor with a band gap at Γ symmetry point. Second, the curvature of the lowest conduction band (CB1) is about 2 times smaller than the top valance band (VB1) indicating that the electron effective mass is larger than that of holes. Third, there is another conduction band (CB2) closely adjacent to CB1. They are parallel to each other in momentum space from Γ to S point. The electronic states of the CB1 is the p-orbital of the central tin atom of the SnI_6 octahedron; while the p- and s-orbital of the 6 outer iodine atoms of the octahedron equally contribute to the CB2 states. The electronic states of VB1 originate mainly from the p-orbital of iodine atoms.

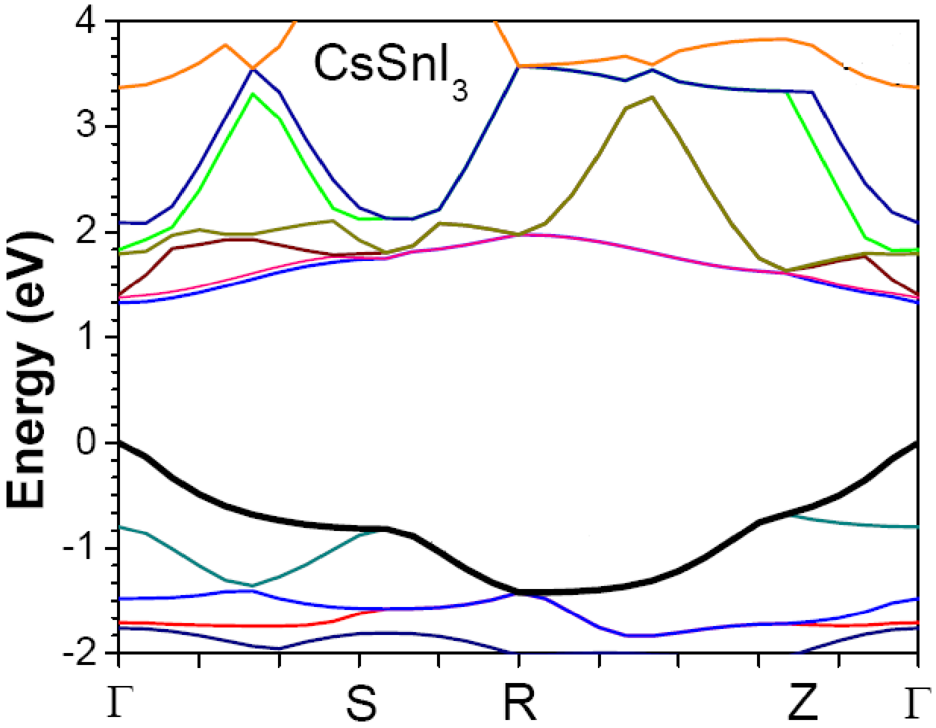

Figure 2.3: Band diagram of $CsSnI_3$. It shows a direct band gap structure at Γ symmetry point with an energy gap 1.3 eV at room temperature. The top valence band indicates the hole effective mass is smaller than the effective mass of conduction electrons. Moreover, the two parallel conduction bands have an energy difference of 64 meV.

CHAPTER 3: Synthesis of $CsSnI_3$

3.1 Material precursors

To synthesize $CsSnI_3$, a direct way is binary compound reaction by CsI and SnI_2. CsI and SnI_2 are ionic compounds. In order to determine the reaction condition for the synthesis, thermo-analytic techniques were used to study the properties of the raw materials and compound.

Method of Differential thermal analysis (or DTA) is a thermo-analytic technique, in which the material under study and an inert reference are made to undergo identical thermal cycles, while recording any temperature difference between sample and reference.[9,10] This differential temperature is then plotted against time, or against temperature (DTA curve or thermo-gram). Changes in the sample, either exothermic or endothermic, can be detected relative to the inert reference. Thus, a DTA curve provides information on the transformations that may have occurred, such as glass transitions, crystallization, melting and sublimation. The area under a DTA peak is the enthalpy change and is not affected by the heat capacity of the sample.

Thermo-gravimetric analysis or thermal gravimetric analysis (TG or TGA) is a type of testing performed on samples that determines changes in weight in relation to a temperature variation in a controlled atmosphere.[11,12] Such analysis relies on a high degree of precision in three measurements: weight, temperature, and temperature change. As many weight loss curves look similar, the weight loss curve may require transformation before results may be interpreted. A derivative weight loss curve can identify the point where weight loss is most apparent. Again, interpretation is limited without further modifications and de-convolution of the overlapping peaks may be required. To determine composition and purity one must take the mass of the substance in the mixture by using thermal gravimetric analysis. Thermal gravimetric analysis is the act of heating a mixture to a high enough temperature so that one of the components decomposes into a gas, which dissociates into the air. It is a process that utilizes heat and stoichiometry ratios to determine the percent by mass ratio of a solute. If the compounds in the mixture that remain are known, then the percentage by mass can be determined by taking the weight of what is left in the mixture and dividing it by the initial mass. Knowing the mass of the original mixture and the total mass of impurities liberating upon heating, the stoichiometric ratio can be used to calculate the percent mass of the substance in a sample. TGA is commonly employed in research and testing to determine characteristics of materials such as polymers, to determine degradation temperatures, absorbed moisture content of materials, the level of inorganic and organic components in materials, decomposition points of explosives, and solvent residues. It is also often used to estimate the corrosion kinetics in high temperature oxidation.

Simultaneous TGA-DTA/DSC measures both heat flow and weight changes (TGA) in a material as a function of temperature or time in a controlled atmosphere. Simultaneous measurement of these two material properties not only improves productivity but also simplifies interpretation of the results. The complementary information obtained allows differentiation between endothermic and exothermic events with no associated weight loss (e.g. melting and crystallization) and those that involve a weight loss (e.g. degradation).

The analyzer usually consists of a high-precision balance with a pan (generally platinum) loaded with the sample. That pan resides in a furnace and is heated or cooled during the experiment. A different process using a quartz crystal microbalance has been devised for measuring smaller samples on the order of a microgram (versus milligram with conventional

TGA).[13] The sample is placed in a small electrically heated oven with a thermocouple to accurately measure the temperature. The atmosphere may be purged with an inert gas to prevent oxidation or other undesired reactions. A computer is used to control the instrument.

This techniques described above were applied to study the thermal properties of the precursors, cesium iodide (CsI) and stannous iodide (SnI_2), for $CsSnI_3$ synthesis. 0.03g CsI or SnI_2 was filled in a corundum crucible, and the same weight of the reference material Al_2O_3 was filled in the other. TGA and DTA were both measured at the same time. As illustrated in Figure 3.1, the melting point of CsI is around 629 ^oC. CsI starts to evaporate as temperature goes up higher than 629 ^oC. SnI_2's melting point is 312.4^o C, but the weight starts to lose as temperature goes up higher than 137.5^{o}C. This is because water exits in SnI_2 crystal due to hydration. Calculation result showed the weight lost due to water was around 20%. For the compound, 0.018g SnI_2 was first transferred into the crucible covered by 0.013g CsI, which is because the melting point of CsI is higher. 0.031g Al_2O_3 was used as the reference material. As shown in Figure 3.1 (c), CsI reacted with SnI_2 at 394.2 ^oC, yielded $CsSnI_3$ which was verified by XRD. The result also shows that $CsSnI_3$ melts at around 389.4 ^oC from the cooling curve, and it evaporates when temperature is higher than ~ 500 ^oC.

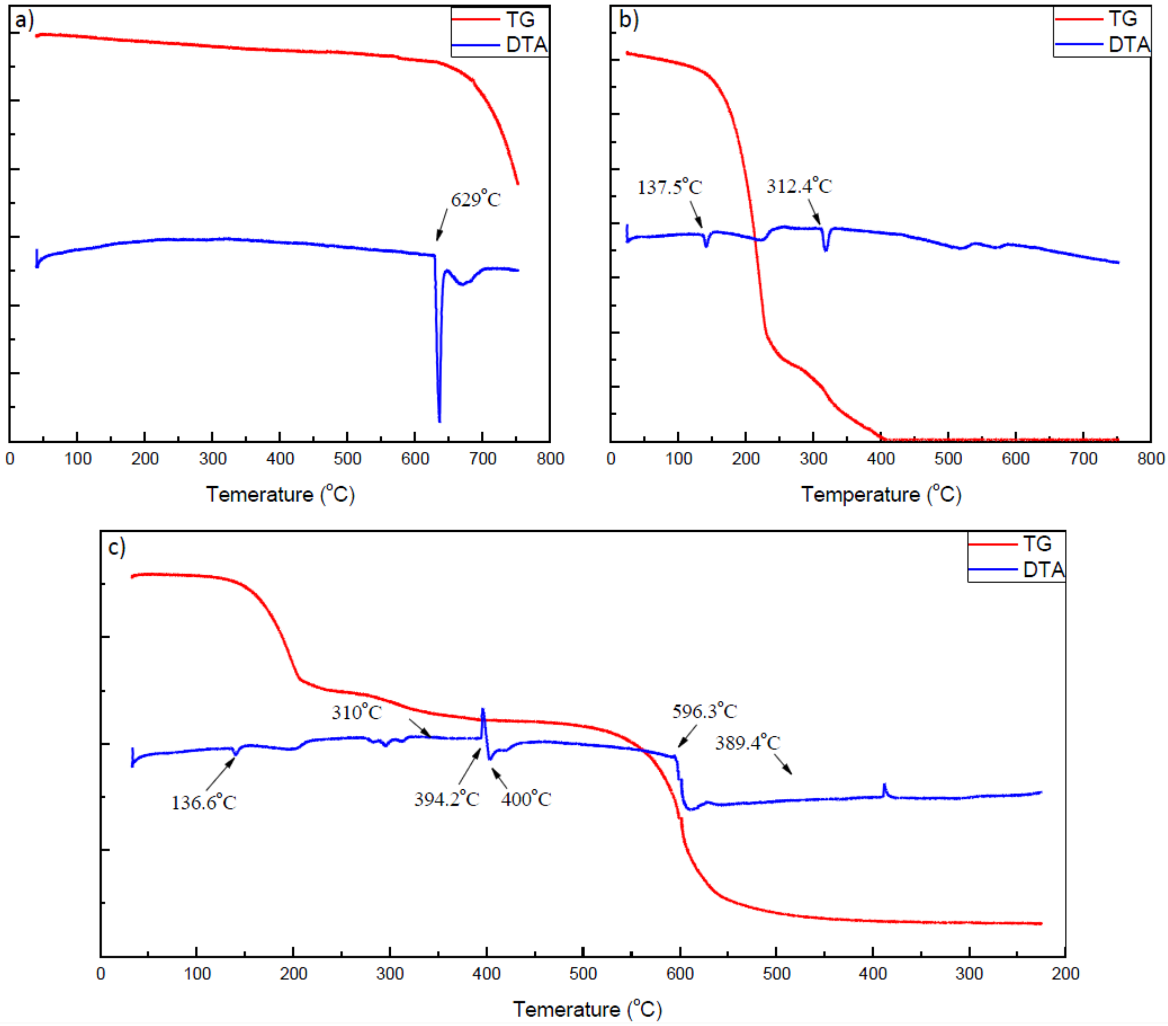

Figure 3.1: TGA/DTA data vs. temperature. (a) TGA/DTA of CsI measured from room temperature to 750 °C; (b) TGA/DTA of SnI_2 measured from room temperature to 750 °C; (c) TGA/DTA of mixed CsI and SnI_2 powder, measured from room temperature to 600 °C, then cooled naturally to 225 °C.

Other parameters of CsI and SnI_2 are shown below:

Molecular formula	**Molar mass**	**Appearance**	**Density**	**Melting point**	**Refractive index**
CsI	259.81 g/mol	white crystalline solid	4.51 g/cm^3	629 °C	1.739
SnI_2	372.519 g/mol	red to red-orange solid	5.28 g/cm^3	312 °C	----

Table 3.1: Properties of CsI and SnI_2.

3.2 Synthesis of $CsSnI_3$ material

3.2.1 Binary compound fusion

Based on our TGA-DTA results, $CsSnI_3$ were synthesized by slowly heating CsI and SnI_2 [Sn(IV)-free] mixed powder in vials to a temperature about 50 °C above the reaction temperature, 450 °C, for about 1 hour. Sample was slowly cooled to room temperature. Reaction yielded a whole piece of black polycrystalline block with a lot of holes on it, which was due the reason that some of the SnI_2 vapor escaped from the mixture while the other reacted with CsI yielding $CsSnI_3$. XRD measurement was taken on a part of this product by breaking it into small pieces and grinding in to powder. Besides the features from $CsSnI_3$, CsI, the measured XRD profile also showed a peak from Cs_2SnI_6, in which Sn(II) was transformed to Sn(IV). Cs_2SnI_6 is also black, solid form at room temperature with a higher melting point than $CsSnI_3$. It may possess metallic nature.

To avoid the Sn(II)-to-Sn(IV) transformation, the raw materials must be carefully dried. The mixed powder was first ground in a N_2 glove box, then heated up to 280 °C to remove the water from SnI_2 hydrate and evacuated at the same time to 10^{-6} torr, then to be sealed in a quartz tube. The quartz tube was 15 inch long and designed to have the shape shown in Figure 3.2. Tube was placed in a two-zone quartz tube furnace. The distance between the centers of the two temperature zones is about 13 inch, and the target temperature was set to be higher than 450 °C for the hot-zone where the source material was located, 300 °C for the cool-zone where the other end of the tube was located. In this way, CsI and SnI_2 can react sufficiently in the hot-zone, and residue SnI_2 will condense at the other end of the tube which is in the cool-zone. Since CsI and SnI_2 was mixed carefully and preheated and reacted under high vacuum, no Sn(IV) showed up. Pure $CsSnI_3$ was obtained from the hot-zone.

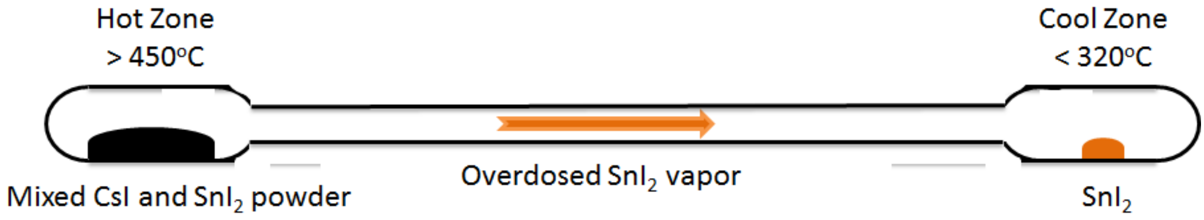

Figure 3.2: Schematic of the quartz tube for binary compound fusion method. Tube must be sealed under high vacuum while the mixed CsI and SnI_2 powder is heated to avoid trace quantity of water.

3.2.2 Precipitation from solution

$CsSnI_3$ can also be synthesized by solution method. Both of CsI and SnI_2 can be dissolved in polar organic solvents, such as N, N-di-methyl-formamide (DMF). CsI reacts with SnI_2 in polar organic solvents, yields $CsSnI_3$. $CsSnI_3$ also dissolves in polar organic solvents. In DMF, the solution is orange, but after being dried, the solid product changes to black. The reaction equation is:

$$SnI_2\ (aq) + CsI\ (aq) \rightarrow CsSnI_3\ (aq) \qquad [1]$$

The solubility of SnI_2 is relatively low, only 0.003 g in 1 mL. Moreover, most of the polar organic solvents have to be operated in inert gas. Another raw material, $SnCl_2$, is also a candidate to produce $CsSnI_3$. $SnCI_2$ can be easily dissolved in water and ethanol, therefore, the reaction condition is much simpler.

Is this method, CsI (99.9% powder) was dissolved in deionized water first (0.8 g/L). Since $SnCl_2$ (99.9% powder) reacts with water as:

$$SnCl_2\ (aq) + H_2O\ (l) \leftrightarrow Sn(OH)Cl\ (s) + HCl\ (aq) \qquad [2]$$

$$6\ SnCl_2\ (aq) + O_2\ (g) + 2\ H_2O\ (l) \rightarrow 2\ SnCl_4\ (aq) + 4\ Sn(OH)Cl\ (s) \qquad [3]$$

In order to avoid Sn(II)'s reaction with water or oxidization before mixed with Cesium iodide, it was first dissolved in anhydrous ethanol instead (0.65 g/mL). Half an hour stirring was made to both of them for fully dissolvent. Certain CsI solution was first transferred to a reaction vial, and stoichiometric amount of $SnCl_2$ ethanol solution was dropped into it by a transfer pipet. After 1 min sonication in an ultrasonic cleaner, the black product in the solution became uniform. The black ink was uniformly dropped on a suitable substrate such as a microscope slide or a piece of ceramic, and then heated to 80 ^oC to remove solvents. Annealing these coated layers at 200 ^oC yielded black $CsSnI_3$ films on various substrates. Procedure is displayed in Figure 3.3. Both $SnCl_2$ solution and CsI solution are colorless. When $SnCl_2$ solution was dropped into CsI solution, black product was formed immediately. The black product was proved to be the direct band gap material $CsSnI_3$ by PL measurement. Chemical reaction equation is:

$$SnCl_2\,(aq) + 3\,CsI\,(aq) \rightarrow CsSnI_3\,(s) + 2\,CsCl\,(aq) \qquad [4]$$

When the product was being dried on a hotplate, the color gradually changed from black to yellow. After annealing, the color of the film became black again.

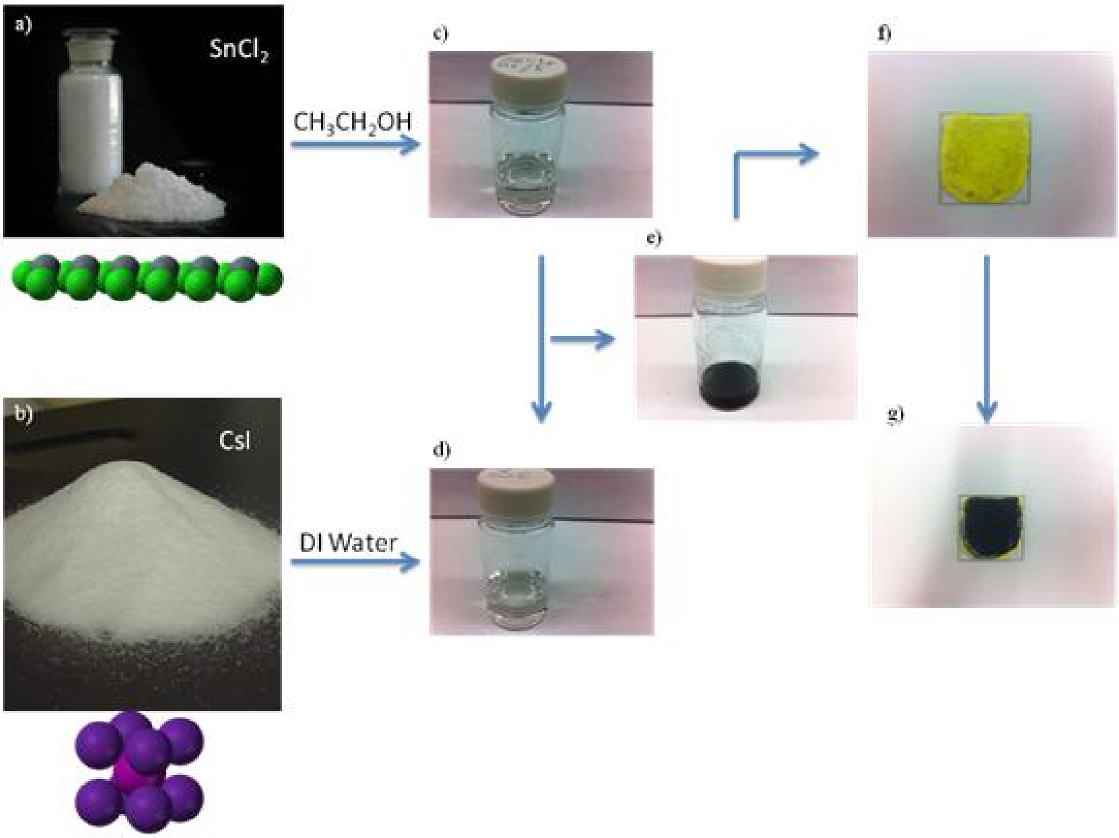

Figure 3.3: Procedure of drop-coating $CsSnI_3$ precipitation from solution. a) Anhydrous $SnCl_2$ powder (99.9%); b) Anhydrous CsI powder (99.9%); c) $SnCl_2$ ethanol solution; d) CsI aqueous solution; e) $CsSnI_3$ ink; f) Drop-coated film on a piece of quartz dried at 80 ^oC; g) Drop-coated film on a piece of quartz annealed at 200 ^oC.

Although water is not good for $SnCl_2$, it is necessary for the reaction between $SnCl_2$ and CsI. If we use anhydrous ethanol for both of $SnCl_2$ and CsI, they will not react. Moreover, the solubility of CsI in ethanol is not as good as in water. In the mixed $SnCl_2$/CsI ethanol solution, if we add a few drops of water, black $CsSnI_3$ was precipitated immediately. The black-γ $CsSnI_3$ in solution is not very stable; it will change to yellow eventually. But the time for it to maintain black phase is due to the ratio of water in the solution. If just a few drops of water, it can stay black up to 12 hours, but if the solution is pure water, it will not stay for more than 30 seconds. Therefore, if we use the maximum concentration for CsI aqueous solution (74g/100mL 20 ^oC as reported, and up to 80g/100mL with half an hour stirring), we have enough water for reaction and the "ink" would maintain black long enough for drop coating.

3.2.3 Single crystal growth

Single crystal $CsSnI_3$ preparation was reported by Scaife et al.[2] The Bridgman-Stockbarger technique was used with a vertical furnace containing two 30 cm heating zones in their report. Schematics of the growth furnace and the heating distribution are displayed in Figure 3.4. The top hot zone temperature was controlled at 490 ^{o}C and the bottom cool zone at about 300 ^{o}C. The temperature gradient was about 16~20 ^{o}C/cm in the crystallization region between the two zones. They first sealed the pre-melted water-free sample in Pyrex or quartz tubes under vacuum or under ½ atm N_2 or Ar. After positioning in the hot zone region, the sample were heated at 490 ^{o}C for 1-2 hr, then lowered through the temperature gradient at 1-5 cm/hr and finally annealed at about 280 ^{o}C for 2-3 hr. The temperature was then reduced from 280 ^{o}C to about 50 ^{o}C in 4 or 5 steps over a period of 4 to5 hours. The color of products was shiny black.

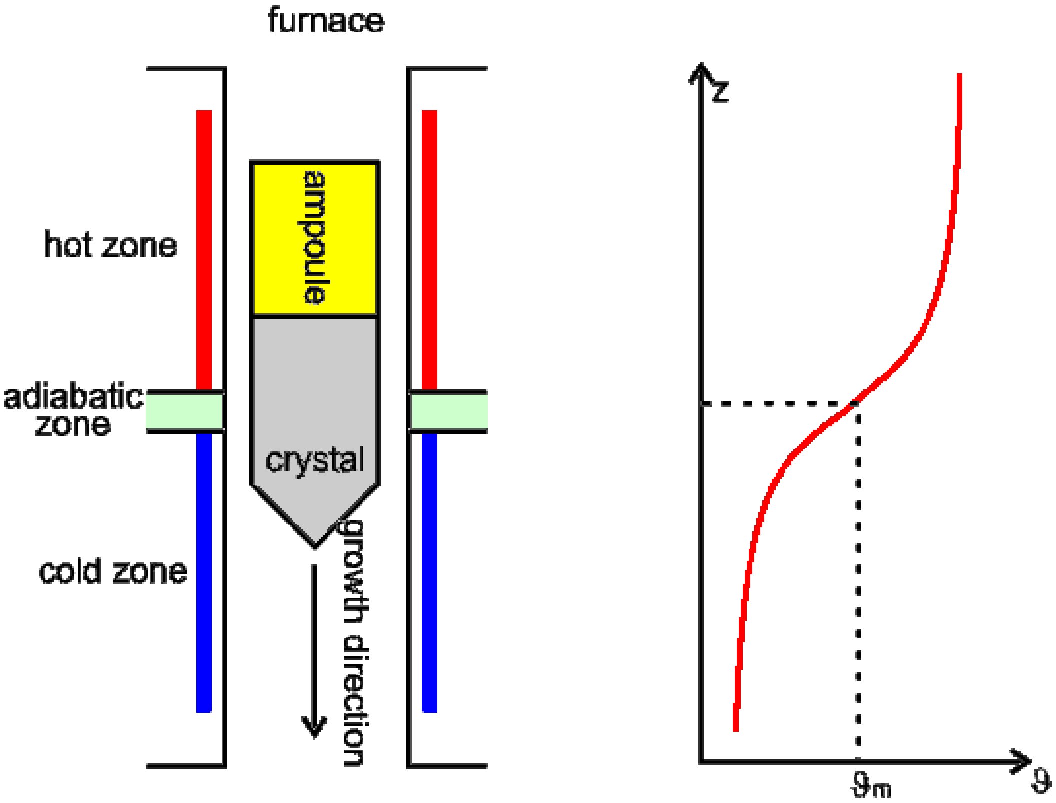

Figure 3.4: Schematic of Bridgman-Stockbarger technique growth furnace and heating distribution.

Another method to prepare single crystal is chemical vapor transport (CVT).[14-17] In a CVT process, a temperature gradient is used to achieve mass transport which occurs using a chemical reaction between the solid to be transported and a gaseous transporting agent. In my study, CVT of $CsSnI_3$ crystals using SnI_2 as a gaseous transporting agent have been carried out in a closed system. SnI_2 has been chosen because it's easily vaporized, reacting with CsI yealds $CsSnI_3$, transport will proceed down the temperature gradient. As we studied in TGA and DTA, $CsSnI_3$'s melting point is higher than SnI_2, which means SnI_2 does not condense with $CsSnI_3$, but at a lower temperature down the gradient. With carefully controlled temperature gradient, reaction of CsI can be sufficient, so that the product can be pure $CsSnI_3$.

Precursor materials of CsI (99.9% powder) and SnI_2 (99.999% beads, ground to powder in N_2 box) were used in this method. Powder was mixed and ground, then carefully dried and evacuated to 10^{-6} torr, to remove trace quantity of water, then sealed in a 15 inch long quartz tube. Tube was then placed in a two-zone quartz tube furnace. The distance between the centers of the two temperature zones is about 13 inch, and the target temperature was set to be higher than 600 ^{o}C for the hot-zone where the source material was located, 300 ^{o}C for the cool-zone where the other end of the tube was located. The tube was designed to have a “sausage” shape, as shown in Figure 3.5, so that the product and the residue materials won’t stick together, and the different parts of the tube can be easily separated. Single crystal $CsSnI_3$ can be obtained on the wall of the tube between the hot zone and cool zone, but the amount is tiny.

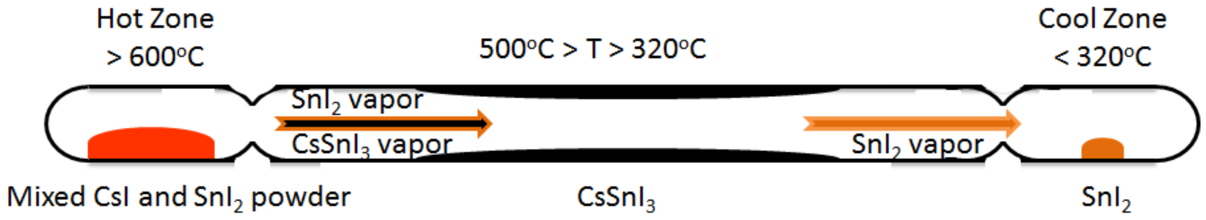

Figure 3.5: Schematic of the “sausage” tube design for chemical vapor transport method to grow single crystal $CsSnI_3$.

3.3 Synthesis of $CsSnI_3$ thin films

3.3.1 Vacuum method

The Vacuum Thermal Evaporation Deposition technique consists in heating until evaporation of the material to be deposited. The material vapor finally condenses in form of thin film on the cold substrate surface and on the vacuum chamber walls. Usually low pressures are used, about 10^{-6} or 10^{-5} Torr, to avoid reaction between the vapor and atmosphere. At these low pressures, the mean free path of vapor atoms is the same order as the vacuum chamber dimensions, so these particles travel in straight lines from the evaporation source towards the substrate. In thermal evaporation techniques, different methods can be applied to heat the material. The equipment available in the laboratory use either bombardment with a high energy electron beam, usually several KeV, from an electron beam gun (electron beam heating) or resistance heating (Joule effect).

The electron beam heating evaporation is also called Electron Beam Physical Vapor Deposition or EBPVD in which a target anode is bombarded with an electron beam given off by a charged tungsten filament under high vacuum. The electron beam causes atoms from the target to transform into the gaseous phase. These atoms then precipitate into solid form, coating everything in the vacuum chamber (within line of sight) with a thin layer of the anode material. The schematic of an EBPVD system is shown in Figure 3.6.

In an EBPVD system, the deposition chamber must be evacuated to a pressure of at least 7.5×10^{-5} Torr (10^{-4} hPa) to allow passage of electrons from the electron gun to the evaporation material which can be in the form of an ingot or rod.[18] The generated electron beam is accelerated to a high kinetic energy and directed towards the evaporation material. Upon striking the evaporation material, the electrons will lose their energy very rapidly.[19] The kinetic energy of the electrons is converted into other forms of energy through interactions with the evaporation material. The thermal energy that is produced heats up the evaporation material causing it to melt or sublimate. The resulting vapor can then be used to coat surfaces.

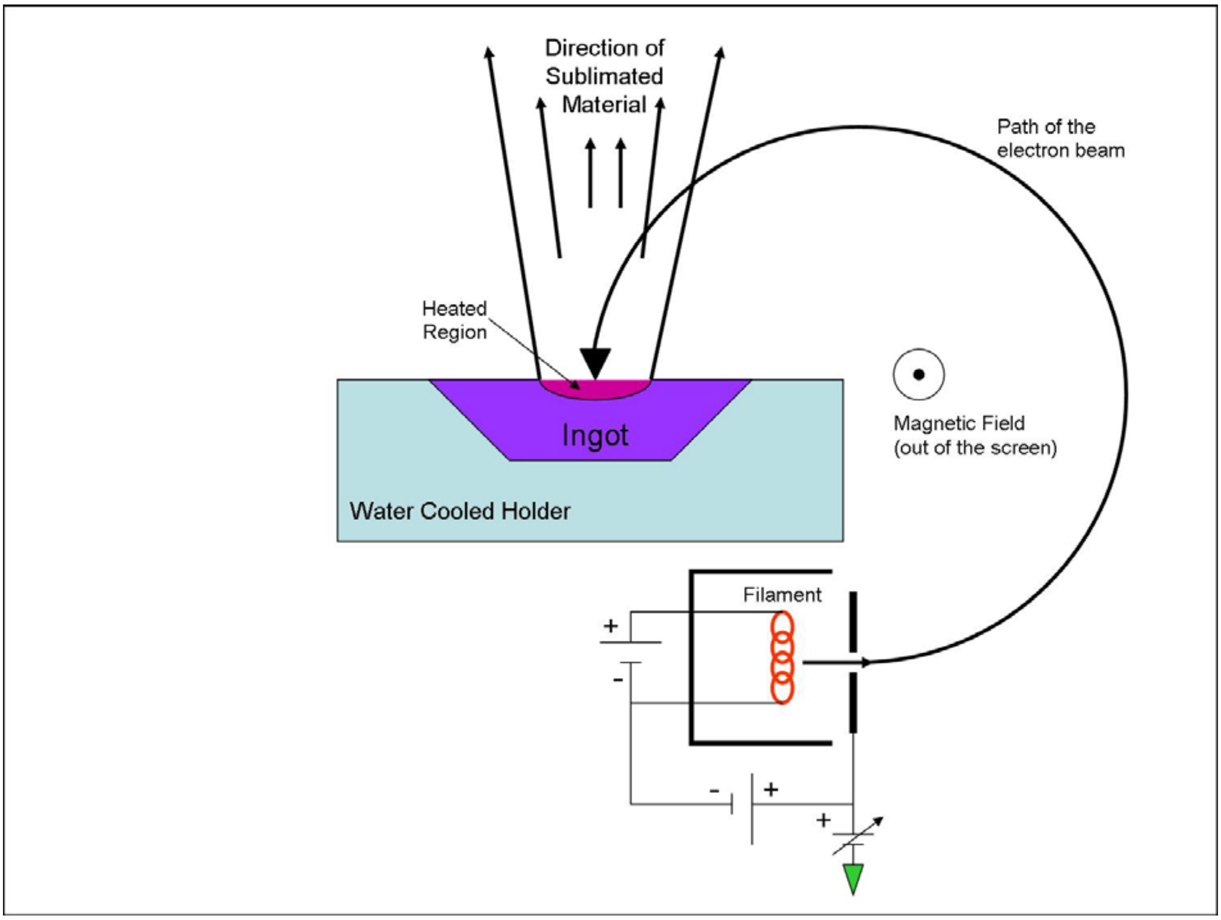

Figure 3.6: Schematic of an E-beam Evaporator. The ingot is held at a positive potential relative to the filament. To avoid chemical interactions between the filament and the ingot material, the filament is protected. A magnetic field is employed to direct the electron beam from its source to the ingot location. An additional electric field can be used to steer the beam over the ingot surface allowing uniform heating.

In the resistance heating thermal evaporation (RHTE), the evaporators known as "boats" due to their shape are the filaments between the two electrodes connected to a power supply. A pool of melted metal forms in the boat cavity and evaporates into a cloud above the source. Alternatively the source material is placed in a crucible, which is radiatively heated by an electric filament, or the source material may be hung from the filament itself (filament evaporation).[20]

In my study, a combination of EBPVD and RHTE is used. An E-beam Evaporator (Temescal BJD 1800) was redesigned as shown in Figure 3.7. Two electrical feedthroughs were added to the main chamber of the evaporator from the bottom ports. A Molybdenum "boat" (filament) was fixed on top to connect them inside the chamber while a current source was wired to them from the outside.

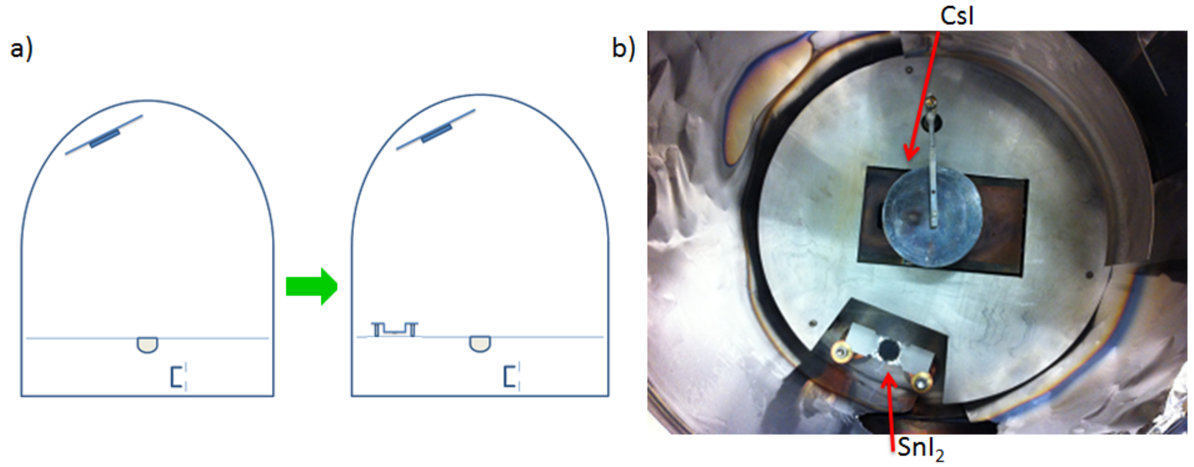

Figure 3.7: Reconfigured E-beam Evaporator. (a) Schematic of the E-beam Evaporator's reconfiguration. (b) Picture of the chamber from the reconfigured E-beam Evaporator.

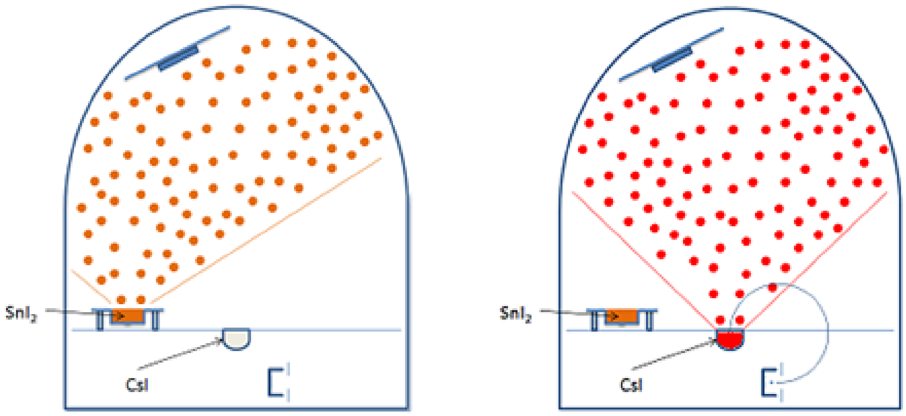

Figure 3.8: Schematic diagram of $CsSnI_3$ precursor deposition procedure by RHTE and EBPVD using two raw materials – SnI_2 and CsI.

The polycrystalline $CsSnI_3$ thin films can be synthesized by a two-step synthesis method. In the first step, high purity multiple layers of stannous iodide (SnI_2) and cesium iodide (CsI) are deposited in vacuum (~10^{-5} Torr) on various substrates by the combination of RHTE and EBPVD, respectively. A schematic of the deposition procedure is shown in Figure 3.8. In order to use EBPVD, CsI powder (99.9% purity) has to be compressed into pellets; otherwise, due to the electrostatic force, charged powder will get out of the crucible and contaminate the system. For thermal process, SnI_2 beads (-10 mesh, 99.99% purity) are placed in a molybdenum boat which both sides are fixed on the two copper electrodes. The RHTE of SnI_2 is usually preceded, because as a top layer CsI is more stable than SnI_2. For the Mo boat (DEEP CUT 4"L 1−3/16"W X 1"−1/4"DEEP), around 49 A DC current is usually used to maintain a deposition speed of 5 Å/s. A layer of SnI_2 with the thickness of 130 nm by thermal evaporation and then followed by a 150 nm E-beam evaporated CsI layer. Deposition speed is also controlled to be 5 Å/s. The same sequence is repeated twice more to have a three pairs of SnI_2/CsI layers. Figure 3.9 is the schematic diagram for the deposition sequence. The as-deposited sample was also verified by SEM, 6 layers with total thickness around 800 nm were shown clearly in the SEM image in Figure 3.10.

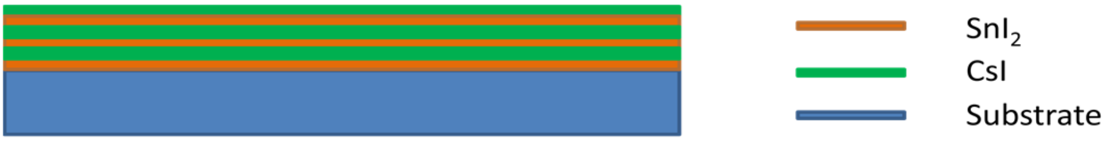

Figure 3.9: Schematic of $CsSnI_3$ precursor deposition procedure. SnI_2 and CsI are deposited alternately for 6 layers in total.

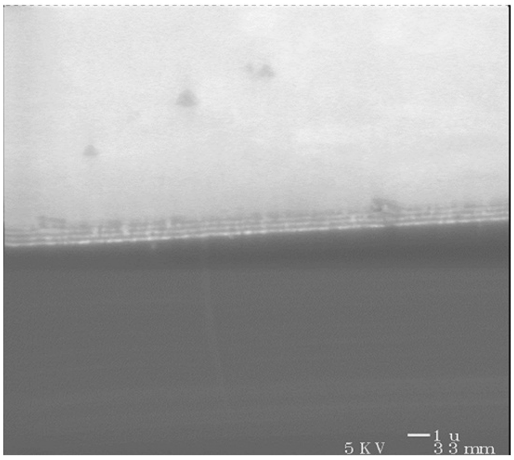

Figure 3.10: SEM image of as-deposited $CsSnI_3$ by E-beam evaporation and thermal evaporation. SnI_2 and CsI were deposited alternately, to form 6 layers in total as shown in the image.

The second step is annealing. The SnI_2/CsI samples need to be annealed under inert gas due to the following reaction at 140 °C in a dry atmosphere[21]:

$$SnI_2\ (s) + O_2\ (g) \rightarrow SnO_2\ (s) + I_2\ (g) \qquad [5]$$

And the following reaction at 150 °C in a moist atmosphere[22]:

$$2\ SnI_2\ (s) + O_2\ (g) + 2\ H_2O\ (g) \rightarrow 2\ SnO_2\ (s) + 4\ HI\ (g) \qquad [6]$$

Usually we anneal the SnI_2/CsI samples in a N_2 glove box with O_2 and H_2O both less than 0.1 ppm. SnI_2 and CsI react when they are heated up to the SnI_2's melting point around 320 °C in inert gas yielding black $CsSnI_3$:

$$SnI_2\ (s) + CsI\ (s) \rightarrow CsSnI_3\ (s) \qquad [7]$$

Figure 3.11 displays the photoluminescence (PL) spectra taken from the selected pieces of SnI_2/CsI samples cut from a Si substrate annealed at different temperatures for 20 s. The peak position of PL does not depend on either annealing temperature or time duration used for the annealing. However, the intensity of PL is strongly dictated by annealing conditions. The optimal condition for the strongest PL intensity depends on a given sample. For a film with SnI_2/CsI layers on Si substrates, the optimum annealing temperature is around 370 °C. The integrated area of PL spectrum at each annealing temperature is summarized in the inset of this figure. Below the melting point of SnI_2 – 320 °C, weak PL was detected and PL almost completely disappeared around the melting temperature, and then, strong band edge PL was measured after annealing with a temperature ~ 50 °C above the melting point of SnI_2. For SnI_2/CsI layers on Ceramic substrates, the optimum annealing temperature is around 400 °C.

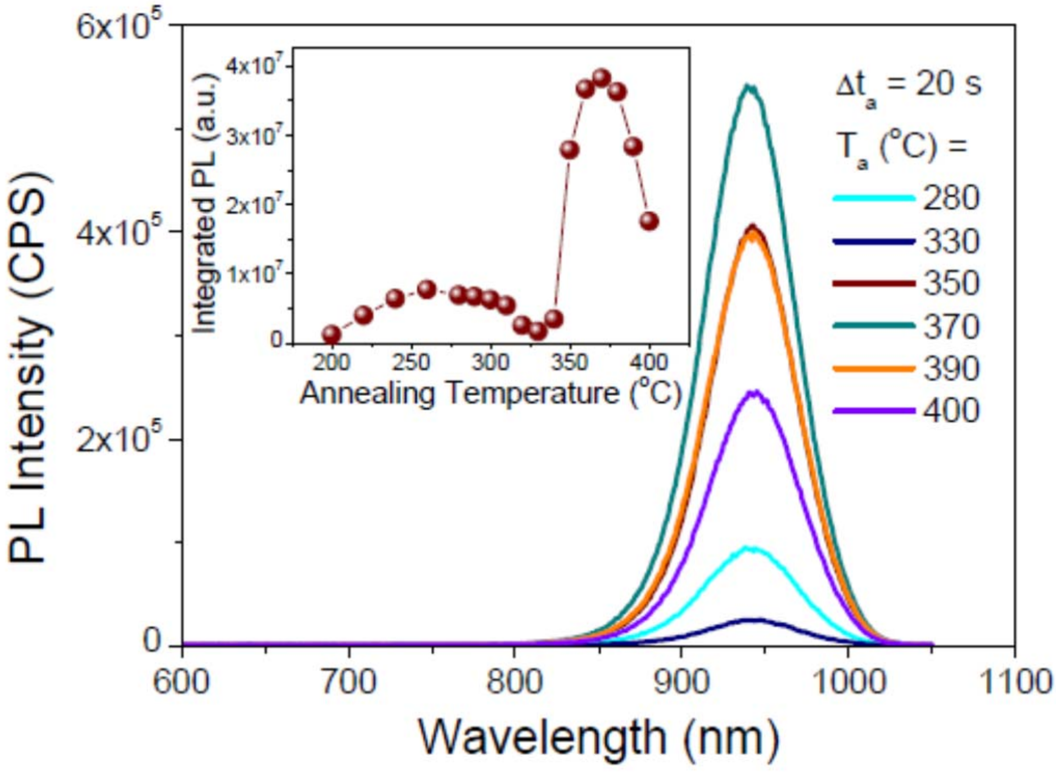

Figure 3.11: PL spectra of CsI/SnI_2 layered samples on a same silicon substrate taken at different thermal annealing temperatures of 370, 350, 400, 280, and 330 °C from top to bottom. The inset displays the integrated PL spectrum at different annealing temperatures.

$SnCl_2$ is also a candidate to synthesis $CsSnI_3$. $SnCl_2$ and CsI can react at around 190 ^{o}C in air. Since $SnCl_2$ is more stable than SnI_2 in air, it does not require an inert gas environment. PL spectrum and XRD proved that the product is also direct band gap material $CsSnI_3$, but it also brings the side product of CsCl:

$$SnCl_2\ (s) + 3CsI\ (s) \rightarrow CsSnI_3\ (s) + 2CsCl\ (s) \qquad [8]$$

3.3.2 Solution method: ultrasonic spray

Spray deposition has been used in the coating industry for a myriad of applications typically achieving uniform films at low cost.[23-25] Sono-Tek ultrasonic spraying system (Figure 3.12 a) can be also employed for $CsSnI_3$ thin-film coating. The system incorporates an ultrasonic atomizing nozzle, vibrating at ultrasound frequency (120 kHz) driven by piezoelectric transducers inside the nozzles' titanium housing. Solutions or inks were first inserted in a syringe (Figure 3.12 b) prior to be pumped (Figure 3.12 c) through the nozzle and were atomized into a fine mist at the nozzle tip (Figure 3.12 d) to produce highly repeatable thin films with micron-sized droplets (Figure 3.12 e), with coating thicknesses from 200 nm to 50 μm. Comparing to pressure spray nozzles and air atomizers, ultrasonic spray nozzles are advantageous in penetrating complex stent geometries, ensuring full coverage of all strut surfaces (Figure 3.12 f). Coatings are much thinner than that can be achieved with dip coating, also saving spray material while avoiding webbing.

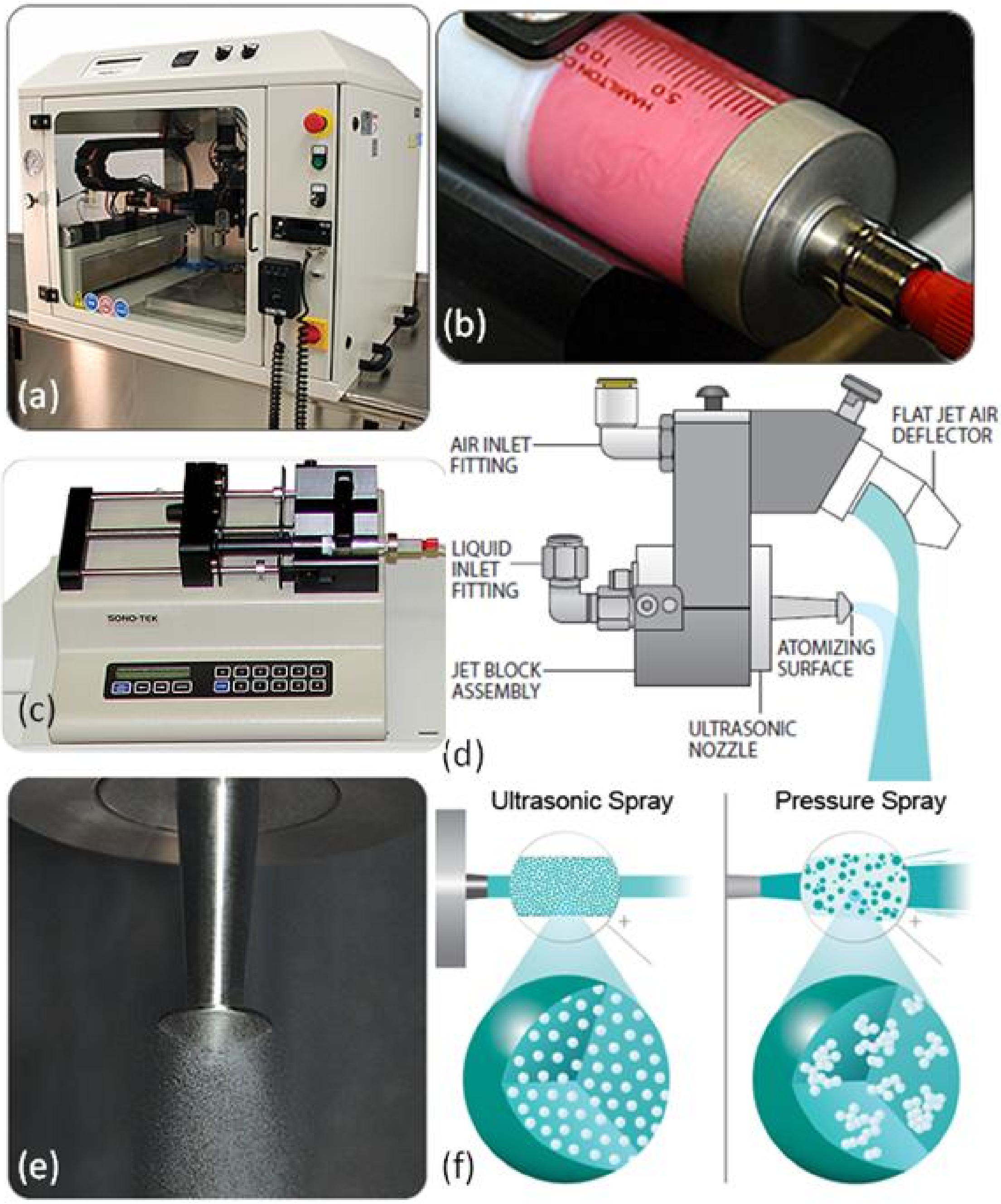

Figure 3.12: Ultrasonic Spray. (a) Sono-Tek ExactaCoat ultrasonic spraying system; (b) SonicSyringe™; (c) Precision Low Flow Liquid Delivery System; (d) Schematic of the spray head; (e) Picture showing mist formation of the liquid; (f) Schematic of de-agglomeration of nanoparticles by the ultrasonic-spray method compared with the air spray method.

The solution-based $CsSnI_3$ synthesis method employing ultrasonic techniques is to be described in this section.[26] Powders of CsI (99.9%) and $SnCl_2$ (99.9%) can be dissolved in deionized water and anhydrous ethanol, respectively. Half an hour stirring is required to fully dissolve both of them. For a particular bath of $CsSnI_3$ synthesis, an amount of 30 mL CsI aqueous solution is to be transferred into a syringe from the vial. The plastic tube connecting the syringe and the nozzle is required to be prefilled before operating the spray system. The valve controlling the connection has to be manually turned on. Then the syringe is to be pushed gently until solution comes out from the nozzle tip. After turning off the valve, the syringe has to be fixed on the syringe pump, so that the spray program can control the spray rate by controlling the rotation speed of the lead screw on the pusher block at the back of the syringe plunger. After setting up the flow rate, the program will control the position of the nozzle to follow the selected path designed by mapping software, meanwhile, turn on the valve and start to push the syringe plunger to achieve the preset flow rate. Microscope slides and ceramic substrates can be preheated to 80 ^oC by a built-in heat plate in the spraying system. The flow rate range can be varied from 0.001 to approximately 30 ml/min. Flow rates depend on the capacity of the syringe used and the speed at which the syringe plunger is moved forward. After CsI aqueous solution is sprayed, the syringe and the tube need to be cleaned by ethanol, to avoid reaction between $SnCl_2$ and residue CsI or H_2O. The same method is then used to prepare the $SnCl_2$ solution for spraying. The substrates with pre-sprayed CsI can be also preheated to 80 ^oC. After both CsI and $SnCl_2$ layers are sprayed, annealing from 200 ^oC will yield black $CsSnI_3$ thin-films.

Procedure is displayed in Figure 3.13. Both tin (II) chloride solution and cesium iodide solution are colorless. When $SnCl_2$ solution was sprayed on CsI, the color changed from white to light yellow. After annealing, the color of the film became black. Chemical reaction can be described as:

$$SnCl_2\,(s) + 3\,CsI\,(s) \rightarrow CsSnI_3\,(s) + 2\,CsCl\,(s) \qquad [8]$$

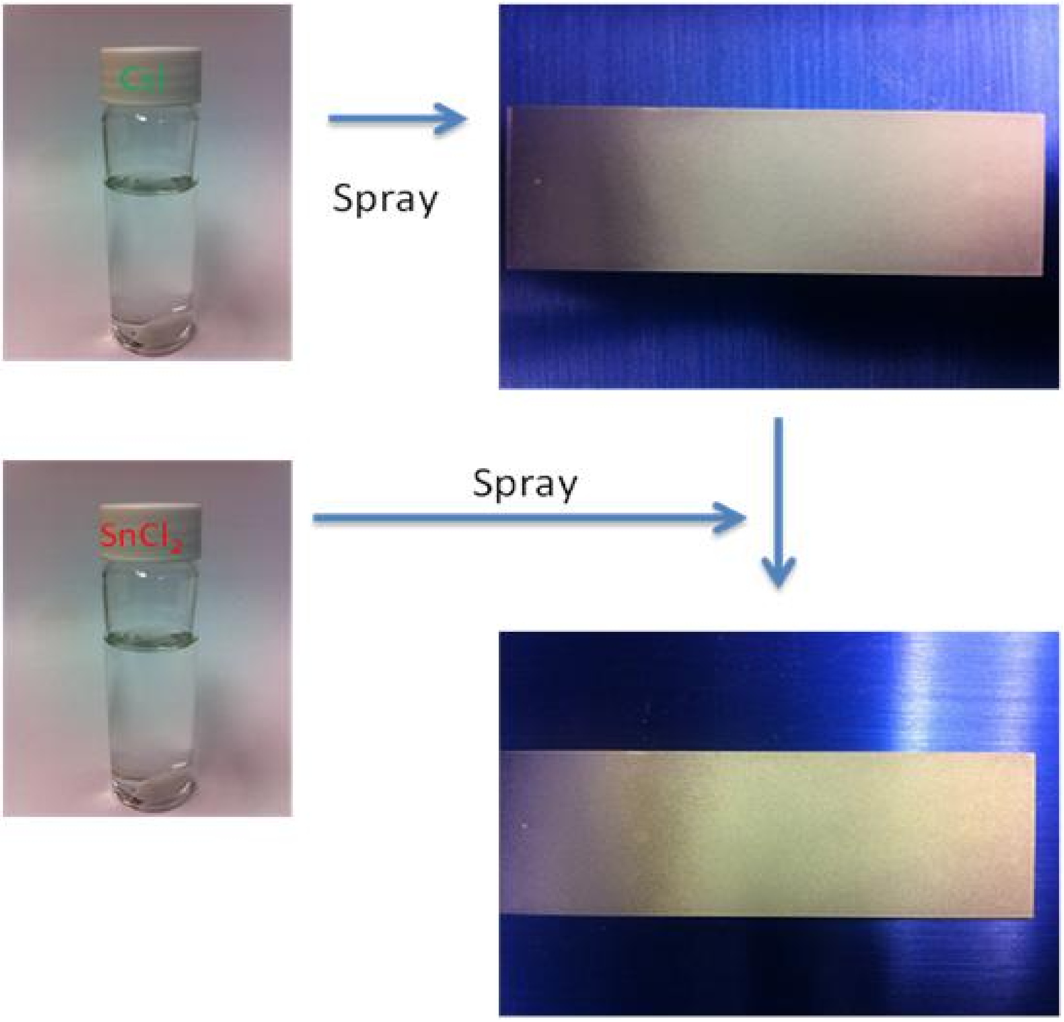

Figure 3.13: Procedure of ultrasonic-spraying $CsSnI_3$ thin film. CsI aqueous solution was first ultrasonic-sprayed to substrates (a microscope slide is used in the figure). Then $SnCl_2$ was ultrasonic-sprayed on top of CsI layer. Color changed to light yellow.

Here we have only used $SnCl_2$ for ultrasonic spray method, because SnI_2 is hardly soluble in H_2O and Ethanol, the concentration is too low for the reaction. Polar organic solvent can be used for this purpose, but it requires operating in inert gas.

3.3.3 Solution method: hybrid approach with chemical vapor deposition

Comparing the two candidates of the precursors - SnI_2 and $SnCl_2$ as used in vacuum method and solution method, there are a few advantages and disadvantages for either of them. From equation [7] and [8] in the vacuum method, we can see that SnI_2 and CsI react to yield $CsSnI_3$ directly, without side products, other than $SnCl_2$ which will yield CsCl. But the annealing process for SnI_2/CsI films is difficult due to reactions [5] and [6], while it is much easier to anneal $SnCl_2$/CsI films to get $CsSnI_3$. Moreover, in the solution method, we cannot easily use SnI_2 since it is barely soluble in water and ethanol. To use SnI_2 in solution method, we have to introduce polar organic solvents, which usually have to be operated in inert gas. For further research and applications, it is important to have pure $CsSnI_3$ material, in other words, it is preferred in using SnI_2 instead of $SnCl_2$.

We have also considered saving the annealing process from an extra step, using vacuum annealing during deposition is a good approach. A combination of spray method and chemical vapor deposition/annealing method has been studied.[27-30] In this method, we first use ultrasonic spray as introduced in the solution method to deposit a layer of CsI. A MTI tube furnace with two temperature zones was used for the reaction process. SnI_2 (99.99%, -10 mesh) beads were placed at the bottom of a smaller quartz tube (1 inch diameter 10 inch long). A pre-sprayed CsI sample was placed on a 1 inch by 4 inch graphite plate, and capped in the smaller tube by a beaker with a slightly greater diameter than the tube. The smaller tube was loaded into the chemical vapor deposition (CVD) quartz tube, so that the bottom of the smaller tube was at the center of the source zone of the CVD, while the sample was at the center of the reaction zone. Reaction and annealing was carried out in vacuum. The temperature of source zone was kept around 330 ^{o}C, a little higher than the melting point of SnI_2, while the reaction zone was a little higher for the reaction between CsI and SnI_2. Figure 3.14 is the schematic diagram of the described reaction process. PL method was used to characterize the samples prepared by this method. It was confirmed that the $CsSnI_3$ thin-films can be formed although a systematic optimization procedure is needed to further improve the film quality.

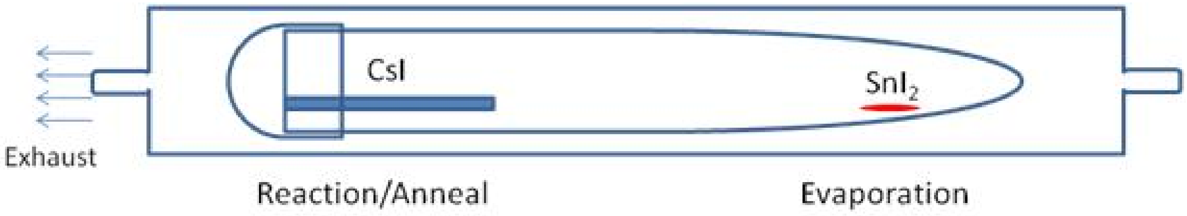

Figure 3.14: Schematic of the CVD reaction/annealing process in the "Ultrasonic Spray + CVD" hybrid method for $CsSnI_3$ deposition.

3.3.4 CVD method

Another approach to synthesize $CsSnI_3$ using CVD is described here, which uses organic precursors.[31,32] Cs_2O and CI_4 (CHI_3, CH_2I_2, CH_3I) will form CsI, $(CH_3)_4Sn$ and C_2H_5I will form SnI_2. Glass & Si samples were submerged in a saturated solution of cesium-containing compound and methanol. The samples are then to be heated on an 80 – 100 °C by a hotplate for 5 minutes. Upon drying, samples are then to be loaded into a horizontal chemical vapor deposition furnace, and heated to 300 to 500 °C for 30 minutes with tetramethyltin and ethyliodide passing through the chamber. Schematic diagram of the procedure is shown in Figure 3.15.

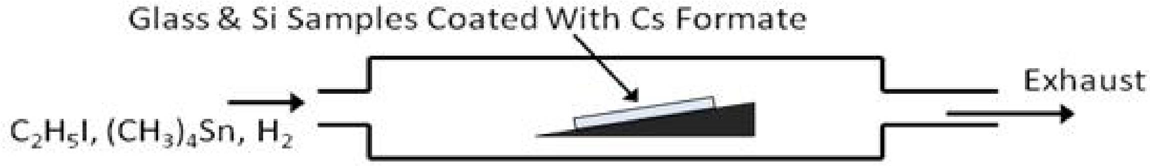

Figure 3.15: Schematic of CVD method. Cs formate was deposited first on the substrates, then loaded in the reaction zone of a CVD with C2H_5I, $(CH_3)_4Sn$, and H_2 passing through the chamber.

CHAPTER 4: Spectroscopic Techniques

4.1 Absorption of semiconductor films on scattering and absorbing substrates

Absorption spectroscopy refers to spectroscopic techniques that measure the absorption of radiation, as a function of frequency or wavelength, due to its interaction with a sample. The sample absorbs energy, i.e., photons, from the radiating field. The intensity of the absorption varies as a function of frequency, and this variation is the absorption spectrum. A material's absorption spectrum is primarily determined by the atomic and molecular composition of the material.[33-36] Radiation is more likely to be absorbed at frequencies that match the energy difference between two quantum mechanical states of the molecules. The absorption that occurs due to a transition between two states is referred to as an absorption line and a spectrum is typically composed of many lines. The frequencies where absorption lines occur, as well as their relative intensities, primarily depend on the electronic and molecular structure of the sample. The frequencies will also depend on the interactions between molecules in the sample, the crystal structure in solids, and on several environmental factors (e.g., temperature, pressure, electromagnetic field). The lines will also have a width and shape that are primarily determined by the spectral density or the density of states of the system.

There are a wide range of experimental approaches to measuring absorption spectra. The source, sample arrangement and detection technique vary significantly depending on the frequency range and the purpose of the experiment. The most common arrangement is to direct a generated beam of radiation at a sample and detect the intensity of the radiation that passes through it. The transmitted energy can be used to calculate the absorption. But for some materials there are also significant reflections which have to be counted to calculate the absorption. Moreover, a scattering caused by the material or sample structure is also hard to be collected by the detector normally fixed along the excited beam direction. Integrating spheres are used to collect the intensity of the radiation that both passes through the materials and is reflected back from them including the scattered ones.[37-40] An Integrating sphere (also known as an Ulbricht sphere) is an optical component consisting of a hollow spherical cavity with its interior covered with a diffuse white reflective coating, with small openings for entrance and exit ports. Its relevant property is a uniform scattering or diffusing effect. Light rays incident on any point on the inner surface are, by multiple scattering reflections, distributed equally to all other points. The effects of the original direction of light are minimized. Therefore, the total power (flux) of a light source can be measured without inaccuracy caused by the directional characteristics of the source. An integrating sphere can also be used to measure the diffuse reflectance of surfaces, providing an average over all angles of illumination and observation. Reflection and absorption of samples can be studied. Since all the light incident on the input port is collected, a detector connected to an integrating sphere can accurately measure the sum of the entire ambient light incident on a small circular aperture.

The optical properties of the lining of the sphere greatly affect its accuracy. Different coatings must be used at visible, infrared and ultraviolet wavelengths. Various coating materials are used. Early experimenters used a deposit of magnesium oxide. Barium sulfate has a usefully flat reflectance over the visible spectrum. Finely-deposited gold is used for infrared measurements. Various proprietary PTFE compounds are also used for visible light measurements. The theory of the integrating sphere assumes a uniform inside surface. Ports must be small, less than about 5% of the surface area of the sphere, for the theoretical assumptions to be valid. Unused ports have matching plugs, with the interior surface of the plug coated with the same material as the rest of the sphere.

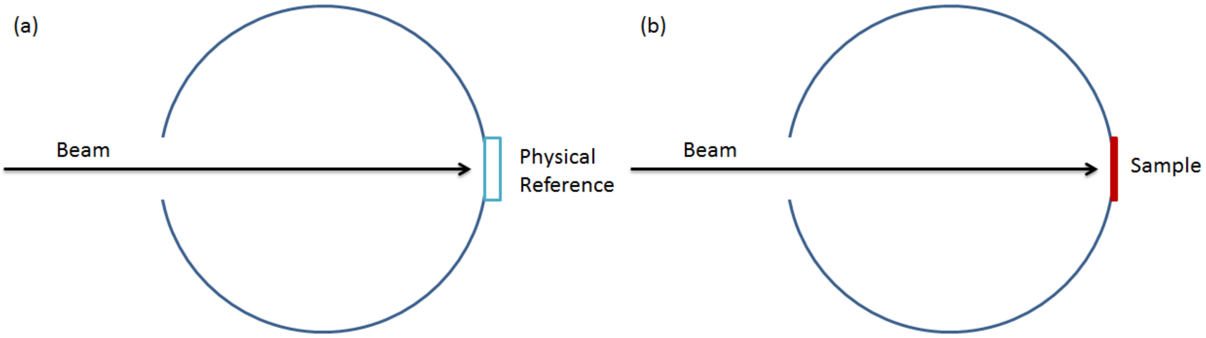

Figure 4.1: Schematic of a single beam integrating sphere. (a) Reference scan; (b) Sample scan.

A simple design of the spectrometer using an integrating sphere is a "single beam integrating sphere".[41] The schematic is shown in Figure 4.1. There is an entrance port for the beam and an exit port for the reference or the sample. A baseline is first measured with a physical reference displaced on the exit port. The transmission of the sample is measured by displacing the sample on the entrance port while the physical reference is still on the exit port. The reflection is measured while the physical reference is substituted by the sample. Then the measured transmission and reflection spectra will divide by the baseline, giving numbers between 0 and 1. Usually a percentage is used to describe transmittance and reflectance. Thereby absorptance can be calculated by subtracting them from 100%.

While reflectance and transmittance are measured in single beam integrating spheres, the single beam substitution error has to be considered, it is the systematic, predictable, and non-random error inherent in the spheres. [42,43] The error is caused by the difference in the throughput of the sphere when the reference makes up a portion of the sphere wall and when the sample is substituted for the reference (Figures 4.1). In reflectance measurements the throughput and corresponding measured reflectance is usually lower when the sample is present since a reference material of high reflectance (nearly 100%) is used. In transmittance measurements the throughput and the measured transmittance is usually higher when the sample is present since an open port (which has zero reflectance when viewed from inside the sphere) is typically used as a reference.

While with spectrophotometers that use a chopped signal between sample and reference this error does not occur. In double beam sphere accessories, the sample and reference beam each ‘see’ the same sphere. There is an active comparison between throughput with both sample and reference in place, thus there is no substitution error (Figure 4.2).

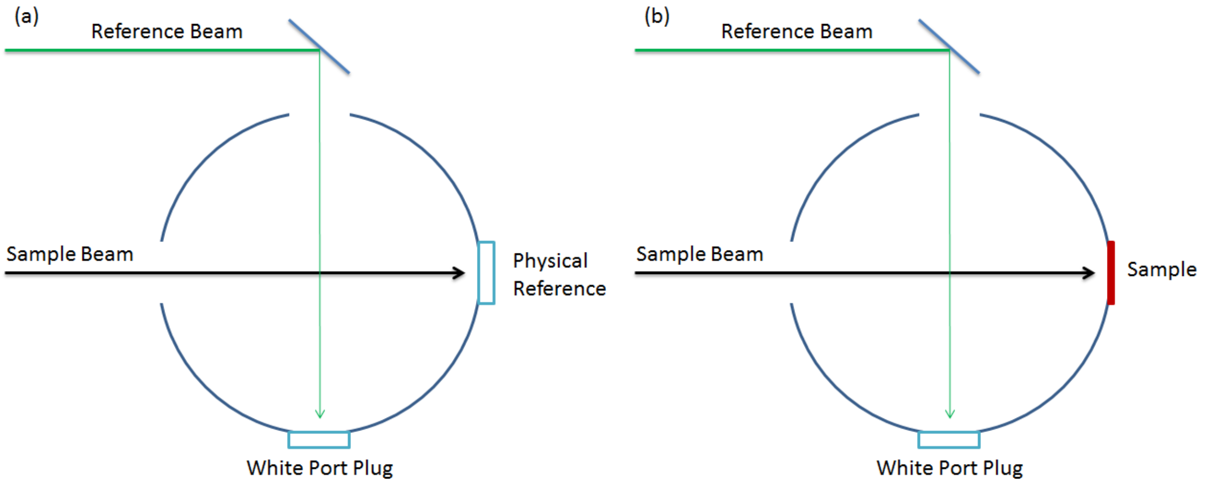

Figure 4.2: Schematic of a double beam integrating sphere. (a) Reference scan; (b) Sample scan.

In my study of $CsSnI_3$, absorption spectra were measured from a Lambda-950 UV-VIS-IR spectrophotometer equipped with a 60 mm integrating sphere from Perkin Elmer. The 60 mm integrating sphere accessory we used is a double beam sphere. A schematic block diagram is shown in Figure 4.3.

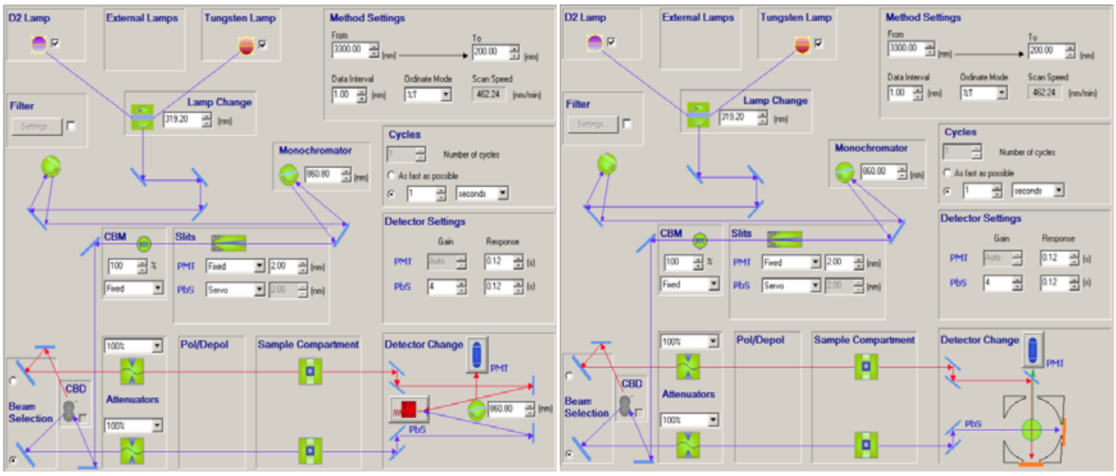

Method Settings
From 3300.00 (nm) To 200.00 (nm)
Data Interval 1.00 (nm)
Ordinate Mode %T
Scan Speed 462.24 (nm/min)
Lamp Change 319.20 (nm)
Monochromator 860.80 (nm)
Cycles
1 Number of cycles
○ As fast as possible
● 1 seconds
Detector Settings
PMT Gain Auto Response 0.12 (s)
PbS Gain 4 Response 0.12 (s)
CBM 100 %
Fixed
Slits
PMT Fixed 2.00 (nm)
PbS Servo 2.00 (nm)
100%
100%

Figure 4.3: Panel diagram for setting up parameters of the Lambda-950 UV-VIS-IR spectrophotometer.

The absorption spectra of $CsSnI_3$ thin films studied in this thesis were taken Lambda-950 UV-VIS-IR spectrometer. Since all the thin films were deposited on absorptive and scattering substrates, the substrate effects had to be properly removed to extract the net absorption spectra of $CsSnI_3$ thin films. This procedure is explained with the help of Figures of 4.4 and 4.5.

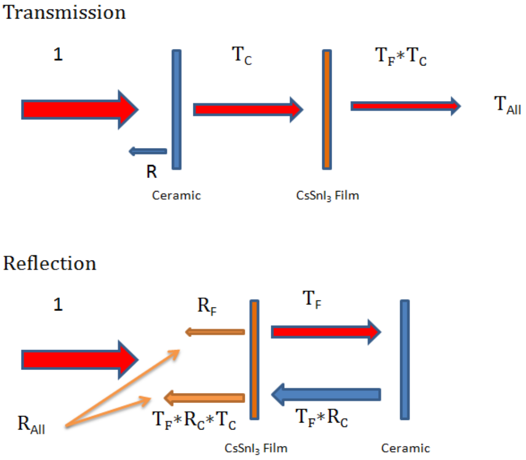

T_C: Transmission of Ceramic

T_F: Transmission of $CsSnI_3$ Film

T_{All}: Measured Transmission of Film on Ceramic

R_C: Reflection of Ceramic

R_F: Reflection of $CsSnI_3$ Film

R_{All}: Measured Reflection of Film on Ceramic

$T_{All} = T_F \times T_C$

$R_{All} = R_F + T_F \times R_C \times T_F$

Figure 4.4: Schematic diagram showing how the measured T_{All} and R_{All} with a substrate is related to the transmission (T_F) and reflection (R_F) of $CsSnI_3$ thin film.

When multiple reflections are neglected, from Figure 4.4, we obtain the transmission and reflection of a $CsSnI_3$ thin film as given by:

$$T_F = \frac{T_{All}}{T_C} \qquad [9]$$

$$R_F = R_{All} - \left(\frac{T_{All}}{T_C}\right)^2 \times R_C \qquad [10]$$

Once T_F and R_F are obtained, based on Figure 4.5, we can deduce the absorption spectrum from Eq. 12.

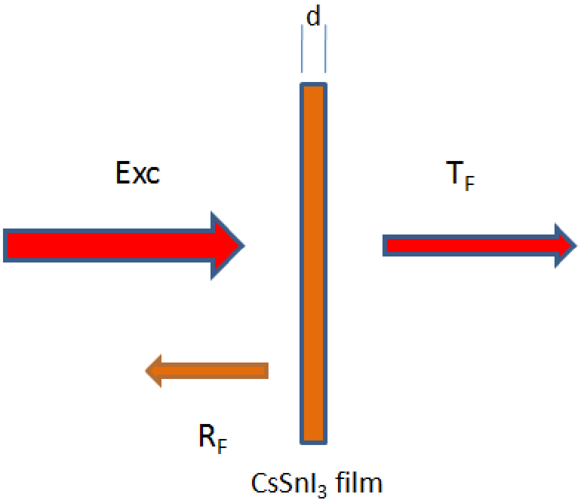

Figure 4.5: Schematic diagram showing how absorption spectrum can be reduced once the transmission and reflection of $CsSnI_3$ thin film are obtained.

$$e^{-\alpha d} = \frac{T_F}{Exc - R_F} \qquad [11]$$

$$\alpha = -\frac{1}{d}\ln\left(\frac{T_F}{Exc - R_F}\right) \qquad [12]$$

4.2 Photoluminescence and photoluminescence excitation techniques

Photoluminescence (abbreviated as PL) is a process in which a substance absorbs photons (electromagnetic radiation) and then re-radiates photons. Quantum mechanically, this can be described as an excitation to a higher energy state and then a return to a lower energy state accompanied by the emission of a photon. This is one of many forms of luminescence (light emission) and is distinguished by photoexcitation (excitation by photons), hence the prefix photo-.[44] The simplest photoluminescent processes are resonant radiations, in which a photon of a particular wavelength is absorbed and an equivalent photon is immediately emitted. This process involves no significant internal energy transitions of the chemical substrate between absorption and emission and is extremely fast, of the order of 10 nanoseconds.

Photoluminescence is an important technique for measuring the purity and crystalline quality of semiconductors such as GaAs and InP.[45-48] Several variations of photoluminescence exist, including photoluminescence excitation (PLE).[49] Time-resolved photoluminescence (TRPL) is a method where the sample is excited with a light pulse and then the decay in photoluminescence with respect to time is measured. This technique is useful in measuring the minority carrier lifetime of semiconductors.[50]

All steady state PL and PLE spectra were taken by a Nanolog system purchased from Horiba Jobin Yvon. A schematic block diagram is given in Figure 4.6 along with typical grating spectral responses for excitation (Figure 4.7 a) and emission (Figure 4.7 b). It consists of a light source (450 W Xe-lamp for PL and 250 W W-lamp for PLE), a double-grating excitation monochromator — which has a cutoff about one millionth of the peak value, the product of the two cutoffs of the individual sections — to select excitation wavelength and its bandwidth, a sample compartment either fiber-coupled or in free-space, and an emission monochromator to spectrally select desired emission to a photomultiplier tube (Hamamatsu P2658P) coupled with a single photon counting electronics.

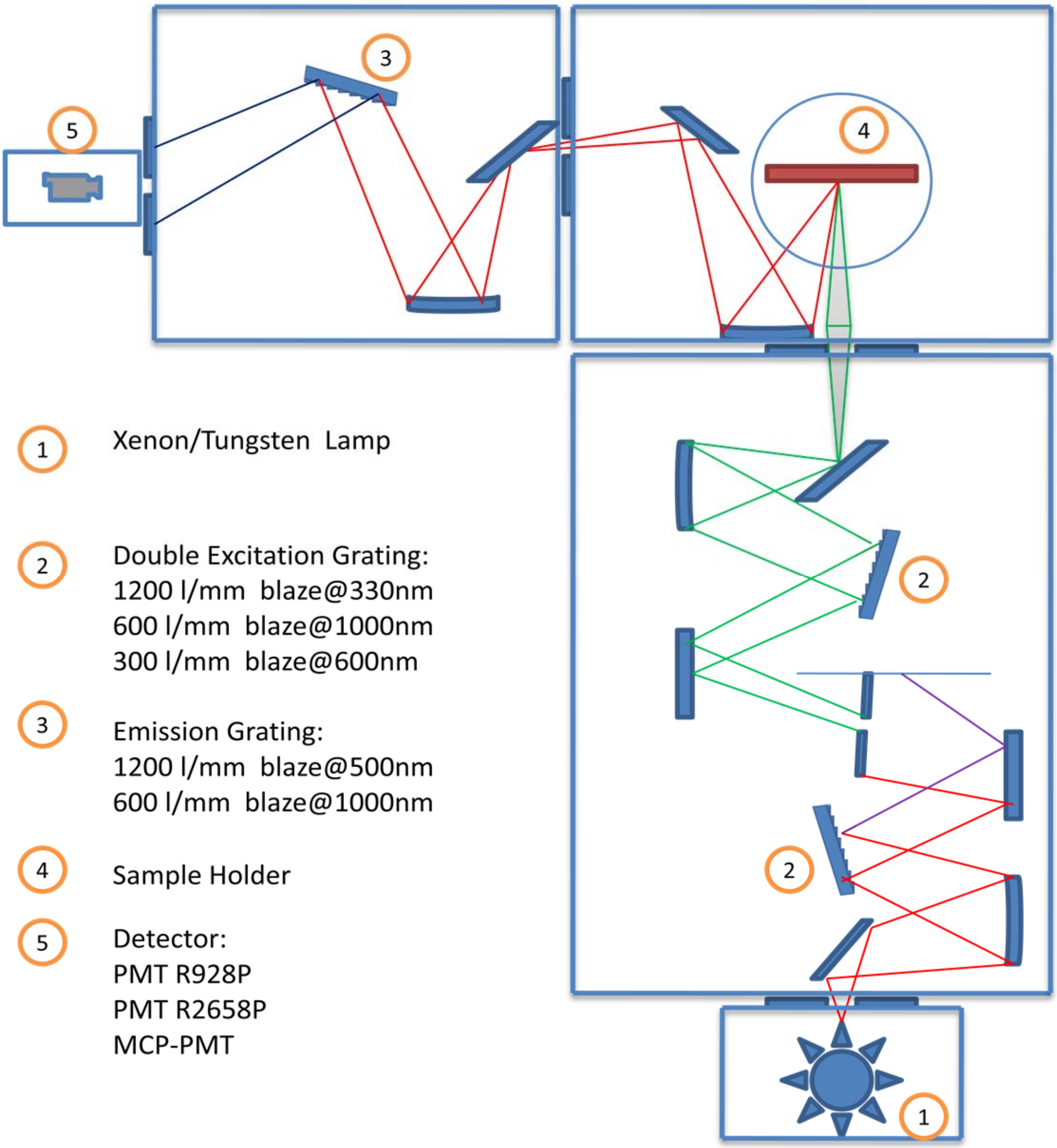

Figure 4.6: Schematic of Nanolog system from Horiba Jobin Yvon. Excitation comes from a Xenon Lamp or a Tungsten Lamp. Double grating was used in the monochromator to provide a cutoff about one millionth of the peak value, which is the product of two cutoffs of the individual sections. Different detectors are used to cover wavelength range from 190 nm to 1600 nm.

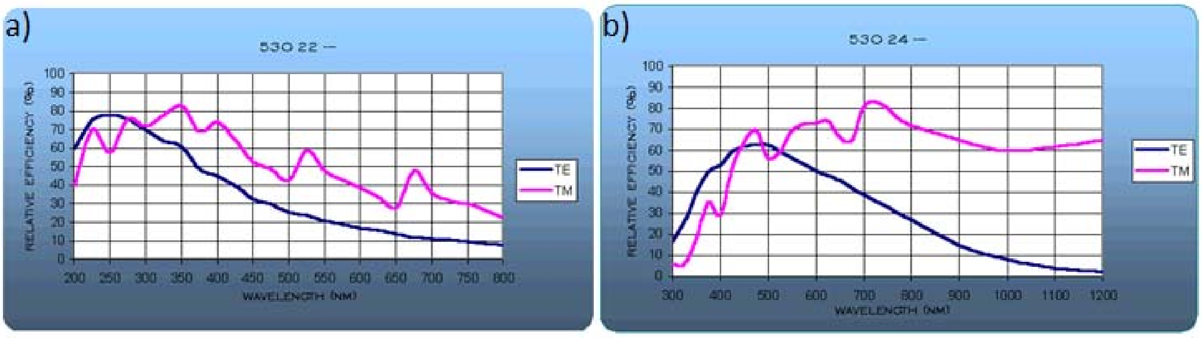

Figure 4.7: Responses of selected gratings: a) An excitation grating; b) An emission grating.

4.3 Time-resolved photoluminescence

TRPL is a contactless method to characterize the recombination and transport processes in various materials and devices.[51-54] TRPL is measured by exciting a sample with a pulsed light source, and then measuring the subsequent decay in PL intensity as a function of time. Various techniques have been used to measure TRPL such as up-conversion[55,56] and streak camera[57,58] methods. In this thesis work, the Time-Correlated Single-Photon Counting (TCSPC) technique was employed.

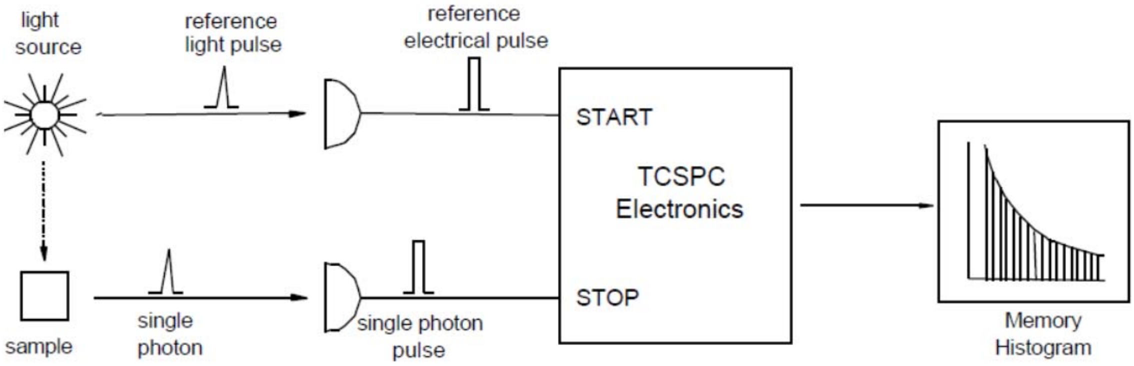

Figure 4.8: Schematic description of the time-correlated single-photon counting (TCSPC) technique.

The light source (laser pulses in our case) is split into two beams. The first beam is being directed to a built-in fast photodiode inside the laser system (High-Q picosecond laser) producing an electrical pulse, and then trigging a time-amplitude converter (TAC) to start (a clock) ramping up a voltage as time-axis. The second beam excites the sample under study generating PL. The majority of PL is passed through a long pass filter, then a monochromator for a selection PL at a given wavelength, and finally onto a PMT producing an amplified electrical signal corresponding a single photon arrival on the PMT. The detected single photon by the PMT sends a stop (the clock) signal to the TAC, and then the TAC voltage is read a y-axis voltage, finally stored by a pulse height analyzer.[59,60]

The principle of TCSPC is the detection of single photons and the measurement of their arrival times in respect to a reference signal, usually from the split excitation laser beam. It should be emphasized that it is a statistical method and a high repetitive light source is needed to accumulate a sufficient number of photon events for a required statistical data precision. The time measured for one START – STOP sequence will be represented by an increase of a memory value in a histogram, in which the channels on the x-axis represent the time. With a high repetitive light source millions of START – STOP sequences can be measured in a short time. The resulting histogram counts versus channels will represent the PL intensity versus time. Generally, one of the input pulses to the TCSPC electronics (either START or STOP) will be a pulse generated by a single photon. Single photons can be detected with photo-detectors having an intrinsic high gain. The majority of those photo-detectors is photomultipliers or micro-channel plate photomultipliers, but also could be single photon avalanche photodiodes. For statistical reasons it is important to ensure no more than one single photon event per light flash is detected. Multi-photon events will affect the histogram statistics and will yield to erroneous measurement results. TCSPC technique is particularly suitable for the condition when excitation power density is low (hence low PL intensity) and the excitation repeats itself with a high-repetition-rate. Under such a condition, light intensity is so low that the probability of detecting one photon in one repeating signal period is far less than one.

CHAPTER 5: Crystal Structure Characterization

5.1 SEM and TEM characterization of $CsSnI_3$ thin films

A scanning electron microscope (SEM) is a type of electron microscope that produces images of a sample by scanning it with a focused beam of electrons.[61-63] The electrons interact with electrons in the sample, producing various signals that can be detected and that contain information about the sample's surface topography and composition. The electron beam is generally scanned in a raster scan pattern, and the beam's position is combined with the detected signal to produce an image. SEM can achieve resolution better than 1 nm.

Transmission electron microscopy (TEM) is a microscopy technique whereby a beam of electrons is transmitted through an ultra-thin specimen, interacting with the specimen as it passes through.[63-67] An image is formed from the interaction of the electrons transmitted through the specimen; the image is magnified and focused onto an imaging device, such as a fluorescent screen, on a layer of photographic film, or to be detected by a sensor such as a CCD camera. TEMs are capable of imaging at a significantly high resolution, owing to the small de Broglie wavelength of electrons. This enables the instrument's user to examine fine detail—even as small as a single column of atoms. TEM forms a major analysis method in a range of scientific fields, in physical sciences. TEMs find application in cancer research, virology, materials science as well as pollution, nanotechnology, and semiconductor research.

SEM images were taken from various films on different substrates. Typical cross-sectional SEM images for films on glass and ceramic substrates are shown in Figure 5.1 (a) and 5.1 (b), respectively. Clear multiple domains are seen with an average domain size of ~ 300 nm.

TEM images were taken from several selected areas, showing different spacing in different orientation. One of TEM images from a film on a glass substrate is displayed in Figure 5.2 (a) showing a triple-domain area. Electron diffraction patterns were also measured. In the areas consisting of many small domains, patterns were typical ring-like, characteristics of polycrystalline crystals as shown in Figure 5.2 (b) and (c) displays a high resolution TEM image of a two-dimensional array of SnI_6 octahedra with a period of 4.2 ± 0.1 Å. This octahedra array matches with the theoretically generated counterpart with a period of 4.3 Å as displayed in Figure 5.2 (d).

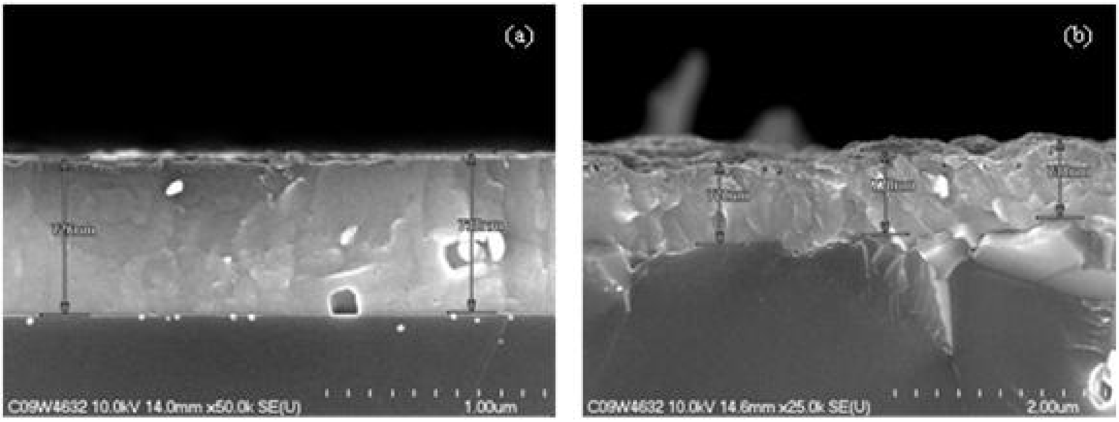

Figure 5.1: (a) SEM image of a $CsSnI_3$ film on a glass substrate. (b) SEM image of a $CsSnI_3$ film on a ceramic substrate.

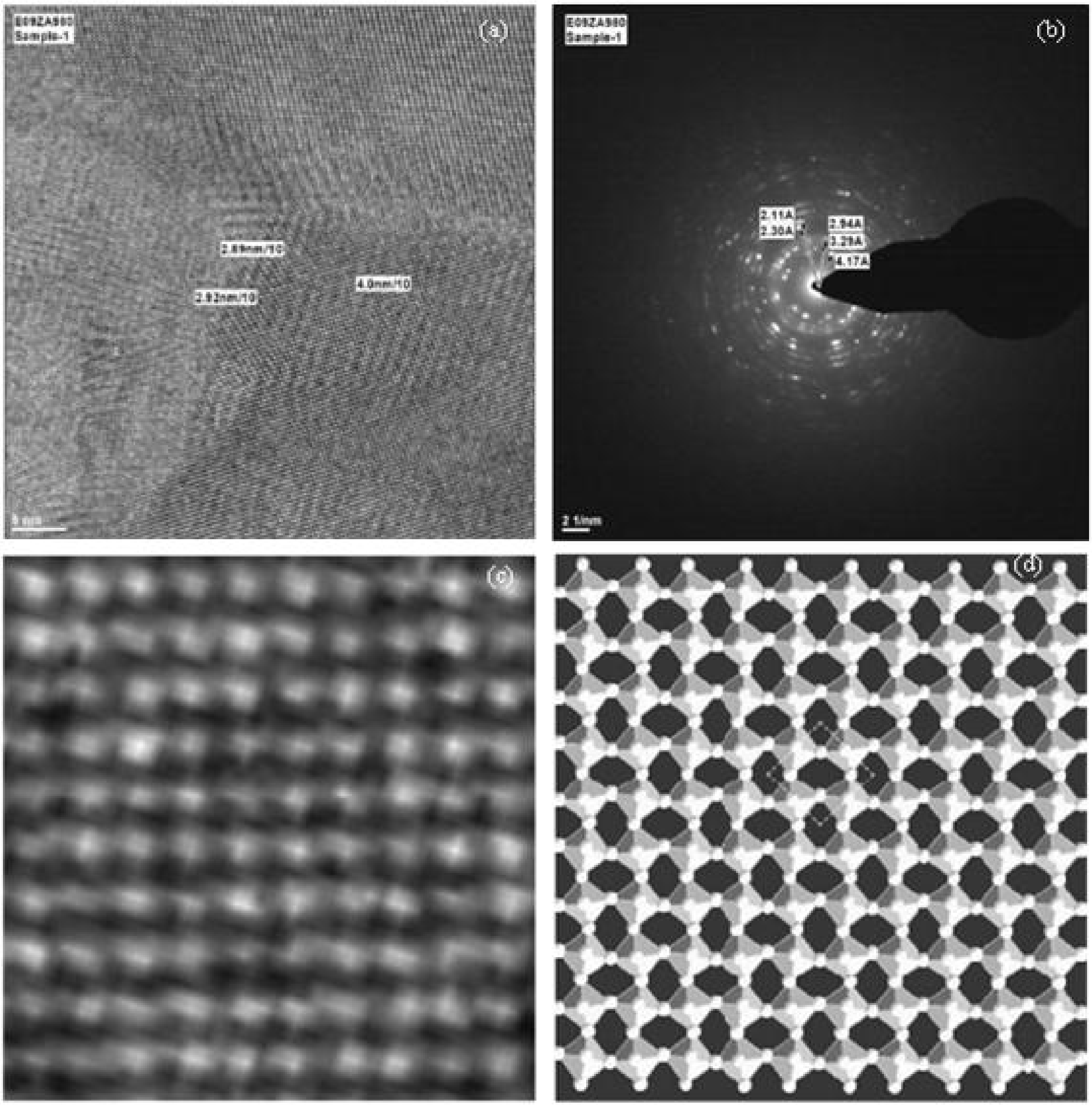

Figure 5.2: (a) High resolution TEM lattice image showing a multiple domain area with different lattice spacing in different orientation. (b) A ring pattern in a selected area where many small domains are gathered. (c) High resolution TEM in a selected area. (d) Theoretically generated 10 x 10 octahedra with tin atoms at the centers and iodine atoms at vertices, projected into an xy plane with x=[-1 1 0] and y=[1 1 0].

5.2 Crystal structure confirmation by X-ray diffraction

X-ray crystallography is a method used for determining the atomic and molecular structure of a crystal, in which the crystalline atoms cause a beam of X-rays to diffract into many specific directions. By measuring the angles and intensities of these diffracted beams, a crystallographer can produce a three-dimensional picture of the density of electrons within the crystal. From this electron density, the mean positions of the atoms in the crystal can be determined, as well as their chemical bonds, their disorder and various other information.[68-71] Since many materials can form crystals—such as salts, metals, minerals, semiconductors, as well as various inorganic, organic and biological molecules—X-ray crystallography has been fundamental in the development of many scientific fields. In its first decades of use, this method determined the size of atoms, the lengths and types of chemical bonds, and the atomic-scale differences among various materials, especially minerals and alloys. X-ray crystallography is still the chief method for characterizing the atomic structure of new materials and in discerning materials that appear similar by other experiments.

In an X-ray diffraction measurement, a crystal is mounted on a goniometer and gradually rotated while being bombarded with X-rays, producing a diffraction pattern of regularly spaced spots known as reflections. The two-dimensional images taken at different rotations are converted into a three-dimensional model of the density of electrons within the crystal using the mathematical method of Fourier transforms, combined with chemical data known for the sample. Poor resolution (fuzziness) or even errors may result if the crystals are too small, or not uniform enough in their internal makeup.

5.2.1 Black-γ phase

We have identified that our synthesized $CsSnI_3$ films have a stable γ-phase structure by the first principle calculation using a commercial software package CASETP[6]. The crystal's total potential energy per unit cell near its minimum (set to be zero) of the γ-phase structure is shown in Figure 2.2. Such a structure has a calculated X-ray diffraction data shown in Figure 5.3. The numbers "1" and "2" indicate XRD features of the Sn-I-Sn bond tilting in x, and y directions, respectively, while "3" represents the signature of the Sn-I-Sn bond tilting in z-direction. The unit cell consisting of 20 atoms used for all our theoretical calculations is displayed in the inset of Figure 5.3.

Measured X-ray diffraction data from pure $CsSnI_3$ synthesized by binary compound fusion method are shown in Figure 5.4 (a). Comparing to the calculated data in Figure 5.4 (b), all the peaks are matched perfectly. The peaks with numbers "1" "2" and "3" also verified the calculated structure. Measured X-ray diffraction data from another sample synthesized by vacuum method are shown in Figure 5.5 (a) with the calculated data in Figure 5.5 (b), main features of the **γ**-crystal structure of $CsSnI_3$ are matched including the tilted Sn-I-Sn bonds in xy-direction and z-direction as indicated by "1, 2, and 3". The XRD peaks from the ceramic substrate are removed for clarity. Structure of the films from solution method was also verified by the XRD. Figure 5.6 (a) shows the XRD data taking from a $CsSnI_3$ ink produced film on ceramic substrate. Figure 5.6 (b) is the calculated XRD intensity. All the calculated peaks can be matched including the main features of the **γ**-crystal structure of $CsSnI_3$ as indicated by "1, 2, and 3". Peaks other than the calculated ones are due to the residue of CsI ("4" and "5"), and the side products of CsCl ("6" and "7") and SnO_2 ("8" and "9"). The presence of SnO_2 peaks indicate that other than the reactions in the vacuum-based method, some Sn (II) is transformed to Sn (IV) in solution-based method.

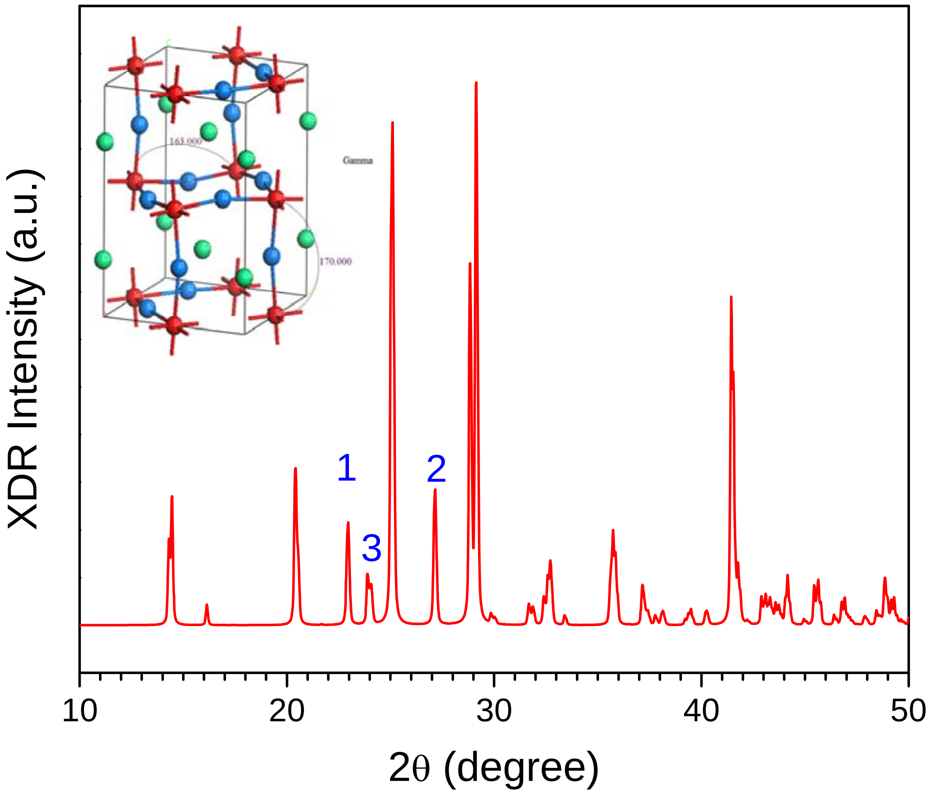

Figure 5.3: Calculated X-ray diffraction profile of the gamma crystal structure and its unit cell is also displayed as inset in the figure.

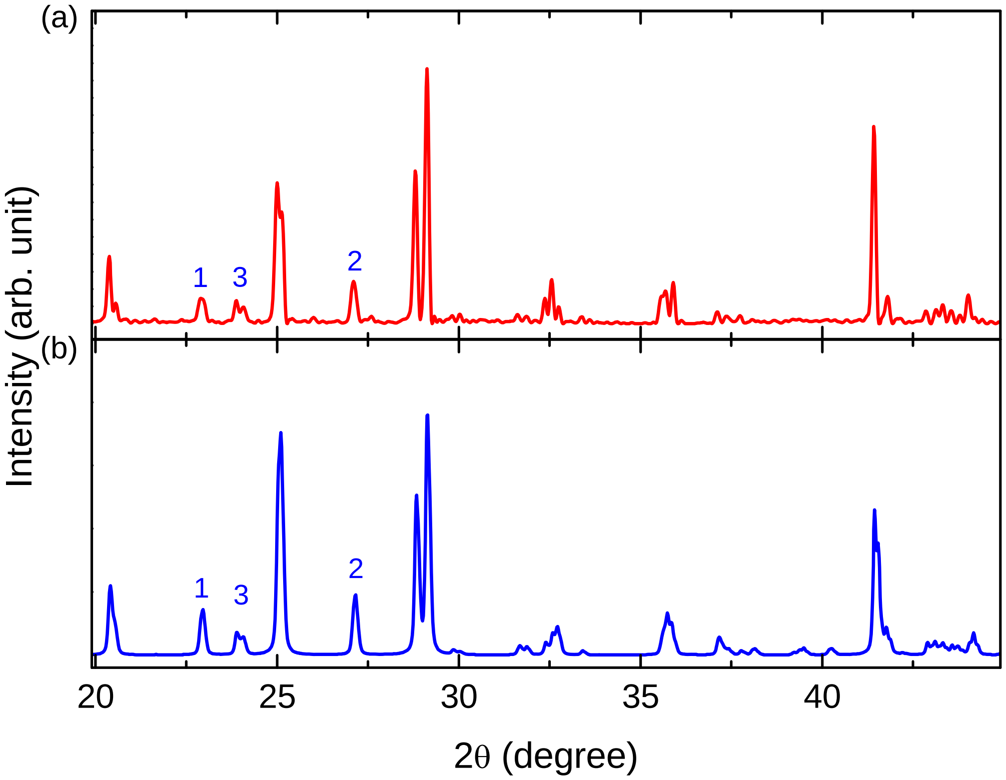

Figure 5.4: (a) Measured XRD intensity as 2θ from pure $CsSnI_3$ synthesized by binary compound fusion method is compared with calculated curve, all the features are matching. (b) Calculated γ-crystal structure $CsSnI_3$ XRD pattern.

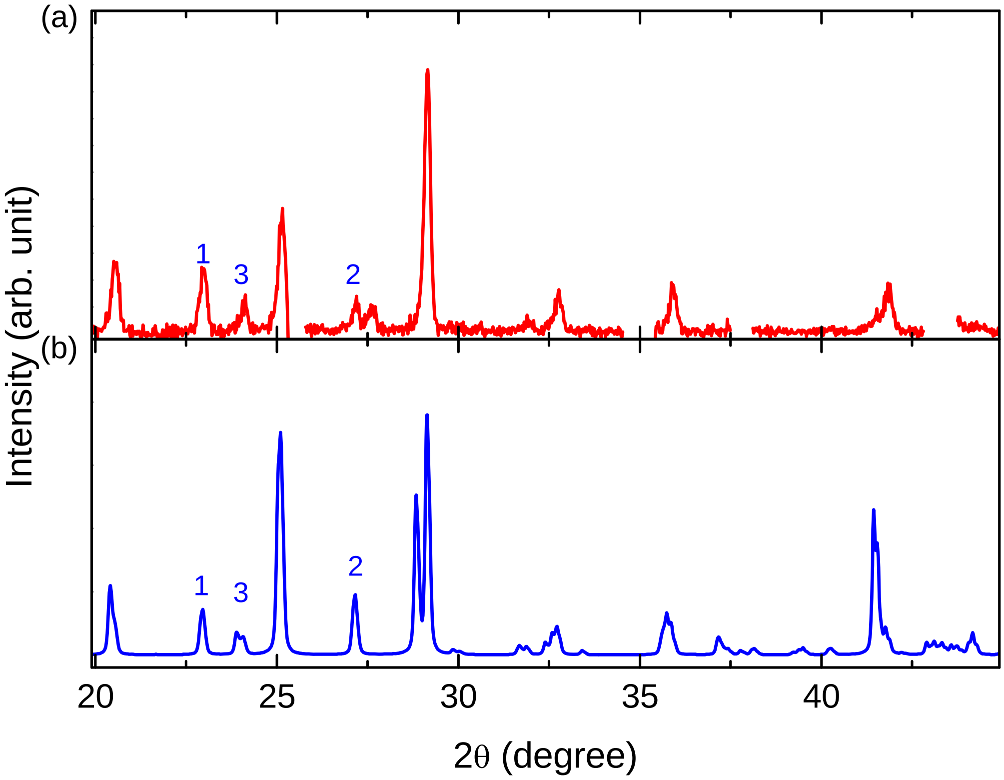

Figure 5.5: (a) Measured XRD intensity as 2θ from a sample synthesized by vacuum method is compared with calculated curve, main features of the γ-crystal structure of $CsSnI_3$ are matched including the tilted Sn-I-Sn bonds in xy-direction and z-direction as indicated by “1, 2, and 3”. The XRD peaks from the ceramic substrate are removed for clarity. (b) Calculated γ-crystal structure $CsSnI_3$ XRD pattern.

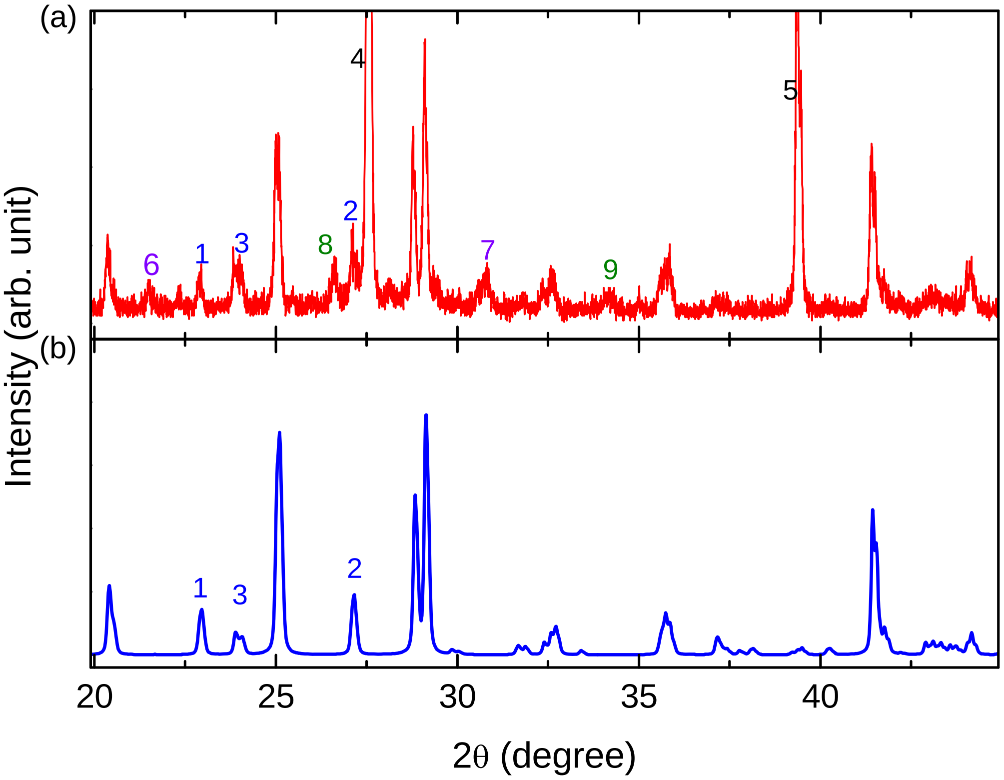

Figure 5.6: (a) Measured XRD pattern of solution-based $CsSnI_3$, main features of the γ-crystal structure of $CsSnI_3$ are matched including the tilted Sn-I-Sn bonds in xy-direction and z-direction as indicated by "1, 2, and 3"**.** Residue reactant and side products are also identified. (b) Calculated **γ**-crystal structure $CsSnI_3$ XRD pattern.

5.2.2 Black-α and -β Phase

Black $CsSnI_3$ was studied by Yamada *et al*[4] in 1991. It was demonstrated by differential thermal analysis and X-ray diffraction that during the cooling of the black $CsSnI_3$ from 450 K, its ideal cubic perovskite structure (B-α) deformed to a tetragonal structure (B-β) at 426 K, and became an orthorhombic structure (B-γ) below 351 K. Figure 5.7 shows the fitted profiles obtained by a Rietveld method together with the raw data obtained by Rigaku Rad-B system with a high temperature cell by Yamada et al.

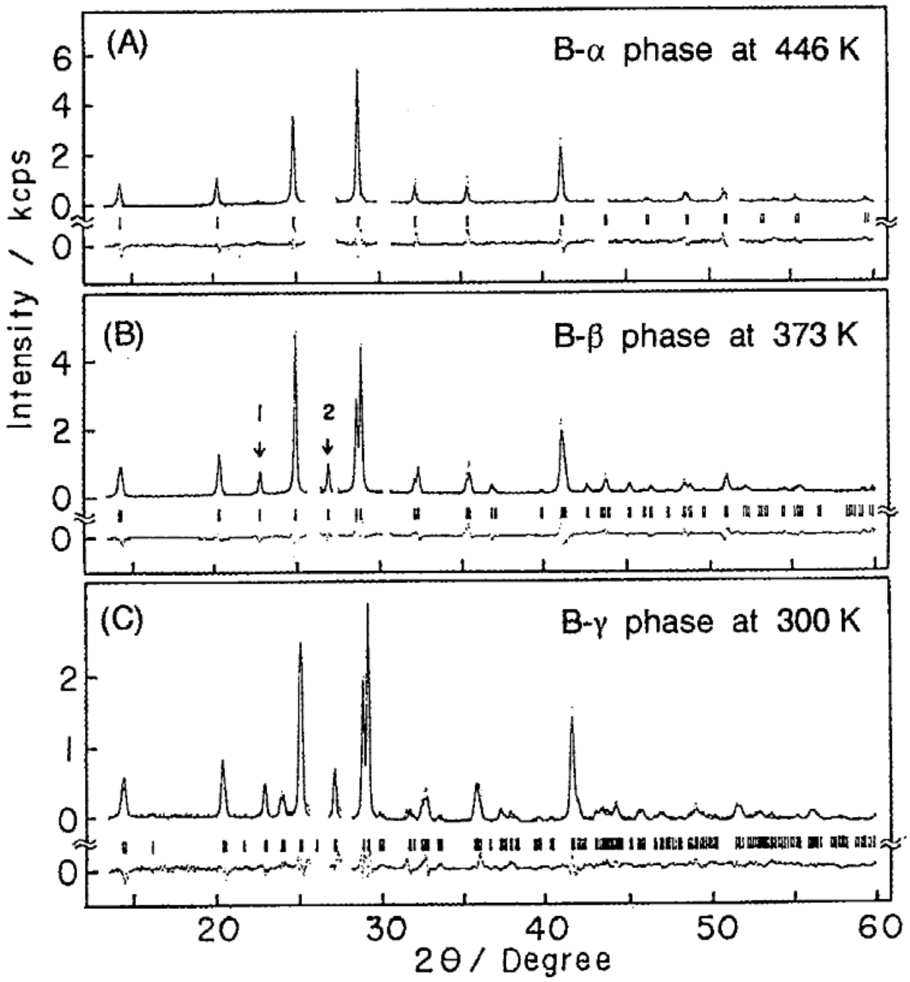

Figure 5.7: Results of the Rieveld refinements for (A) B-α phase, (B) B-β phase, and (C) B-γ phase.[4] The fitted profiles and the raw data are shown by solid-line and dots, respectively. The lower portion is a plot of the difference between them. The vertical marks below the profiles indicate the positions of all features included in the calculations.

CHAPTER 6: Experimental Determination of $CsSnI_3$ Band Structure

6.1 Absorption

Optical absorption spectra of $CsSnI_3$ thin films were measured at room temperature. A typical absorption spectrum of $SnCl_2$/CsI layered films deposited on ceramics is displayed in Figure 6.1 along with the PL spectrum taken from the same film. The absorption contribution from the substrate was removed and scatterings were considered through the integrating sphere. The absorption spectrum reflects the nature of the inhomogeneity of the film in terms of composition and domain sizes. The value of the absorption coefficient steeply takes off right after the peak of PL emission and is nearly zero below it. This behavior is a testimony for the direct band gap of $CsSnI_3$.[72] The shoulder riding on the absorption curve, ~ 50 meV away from the PL peak position, may associate with the second conduction band CB2 although more work is needed to fully understand the nature of absorption in $CsSnI_3$ thin films. It should be emphasized that the PL is very intense under a weak photo-excitation indicating very high quantum efficiency, which is supportive to our direct band gap assertion for the $CsSnI_3$ compound as predicted by calculations from the first principles. The PL line shape is inhomogeneously broadened with a spectral width of ~ 50 meV.

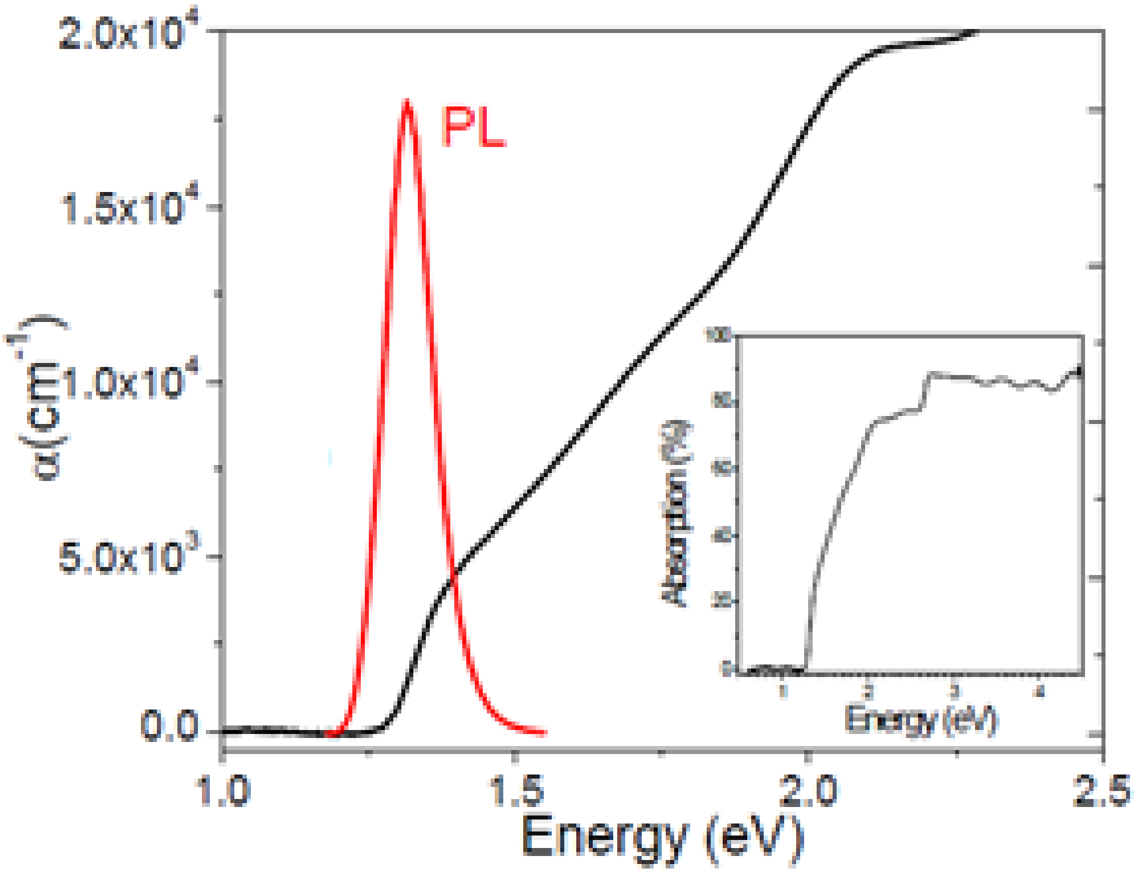

Figure 6.1: Absorption and PL spectra of $CsSnI_3$ film on a ceramic substrate measured at room temperature.

6.2 Emission mechanism of $CsSnI_3$

After a carefully study on the experimental results taken from this perovskite semiconductor compound, an exciton emission mechanism was identified.[73] The exciton binding energy of black-γ $CsSnI_3$ was deduced to be 18 meV, which is much larger than expected based on the empirical band gap energy scaling law. This suggests the motion of non-resonantly photo-excited excitons in $CsSnCl_3$ is two-dimensional in the 2D layers of SnI_4 tetragons. The determination of exciton binding energy in $CsSnI_3$ will be discussed in Chapter 7.

CHAPTER 7: Determination of Exciton Binding Energy in $CsSnI_3$

Wannier[74] excitons provide many desirable optical properties of semiconductors such as enhanced spontaneous emission efficiency over free electron-hole recombination,[75] low current thresholds for exciton or exciton-polariton lasers,[76-78] and fast and large electro-absorption change in electro-optic modulators.[79,80] Large exciton binding energy is required to operate many exciton-related devices at room temperature because of the thermal dissociation of excitons to separated electrons and holes. Exciton binding energy is an intrinsic property for a given bulk semiconductor; it is known to obey the empirical energy band gap scaling law, i.e., proportional to its energy band gap.[81,82] Relatively low band gap semiconductors such as GaAs, InP, InSb, and their alloys have small exciton binding energies compared to the thermal energy of 26 meV at room temperature. Spatial exciton confinement either in one dimension, two dimensions, or three dimensions increases the binding energy of excitons and is nowadays widely used to produce many optoelectronic devices used in optical communication and light display.

There are many methods used to determine exciton binding energies depending on different material systems. For example, the exciton binding energy of 4.2 meV for bulk GaAs was accurately determined by the low temperature absorption measurements in which 1s and 2s excitonic absorption peaks were identified.[83] For polycrystalline semiconductor materials, inhomogeneous spectral line broadenings are usually large; it is difficult to determine exciton binding energy from the spectral information contained in photoluminescence, absorption, photocurrent, modulated-reflection, or photo-excitation spectra.

7.1 Temperature dependence of steady state PL

Figure 7.1 displays the temperature dependent PL spectra from one of the best $CsSnI_3$ thin-film samples. It shows the decrease of PL peak intensity and the spectral line broadening with temperature from 10 to 300 K. The integrated PL over the full spectrum decreases with temperature as shown in Figure 7.2. The PL peak position monotonically shifts to higher energy as temperature increases, a different behavior as compared to the most of semiconductors. In other words, the energy band gap increases as temperature increases. The detailed discussion of this behavior will be presented in chapter 8. Apparently, it is common for the integrated PL to decline with increasing temperature, simply because non-radiative channels open up as temperature increases. What is unique for this compound and is also pivotal to simply determine exciton binding energy is the rate of PL decreasing. This rate is much slower than that from the most of common direct band gap semiconductors such as InGaAs and AlGaAs epitaxial layers grown even on lattice-matched crystalline substrates in a large temperature range 10-300 K. As quantitatively analyzed below, the slow PL decrease rate arises from the fact that in this compound, the thermal ionization of excitons is only comparable non-radiative process that competes with radiative exciton annihilation process.

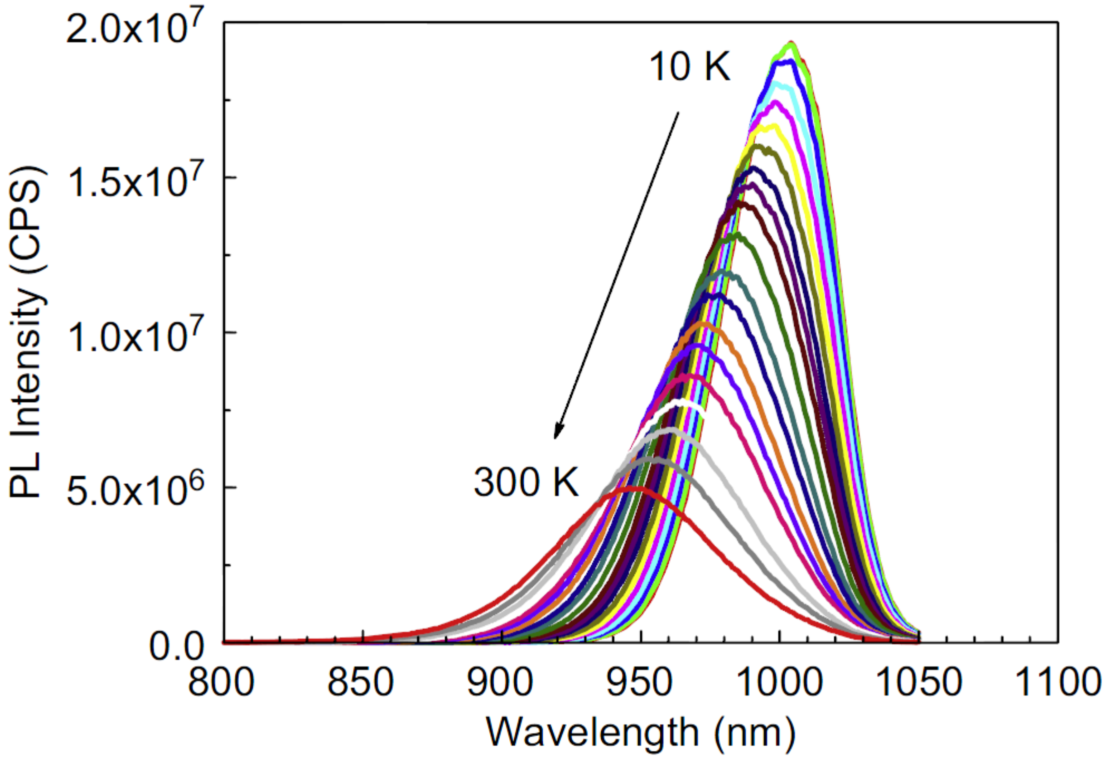

Figure 7.1: PL spectra from 10 to 300 K for one of the best samples we studied, excited by a Xe-lamp with the excitation power density of ~ 20 mWcm^{-2} at 500 nm with a 5 nm bandwidth.

When we assume that the measured PL arises from excitonic annihilations and the decrease in PL intensity is only due to the increase in thermal dissociation rate of excitons at higher temperatures, then the following rate equation should hold:

$$R_G = R_{spon} + Aexp\left(-\frac{E_{bx}}{K_B T}\right), \qquad [13]$$

where R_G is the exciton generation rate maintained by photo-excitation and R_{spon} is the spontaneous emission rate giving rise to PL; the last term in Eq. [13] is the thermal dissociation rate for excitons, with the exciton binding energy, E_{bx}, as the activation energy for ionization. With the limiting condition of $R_{spon} \rightarrow 0$ when $T \rightarrow \infty$, $A = R_G$, Eq. [13] becomes

$$R_{spon} = R_G\left[1 - \exp\left(-\frac{E_{bx}}{K_B T}\right)\right] \qquad [14]$$

Since R_{spon} is proportional to the integrated PL intensity, by fitting Eq. [14] to the experimental data displayed in Figure 7.2, the value of exciton binding energy, 18 meV, is determined based on this model. Before discussing this relatively large exciton binding energy value, it is necessary to provide additional evidence to validate the Eq. [13], i.e. to show the radiative exciton annihilation process dominates all non-radiative processes. Picosecond time-resolved PL technique is a direct and useful tool to deliver such a proof.

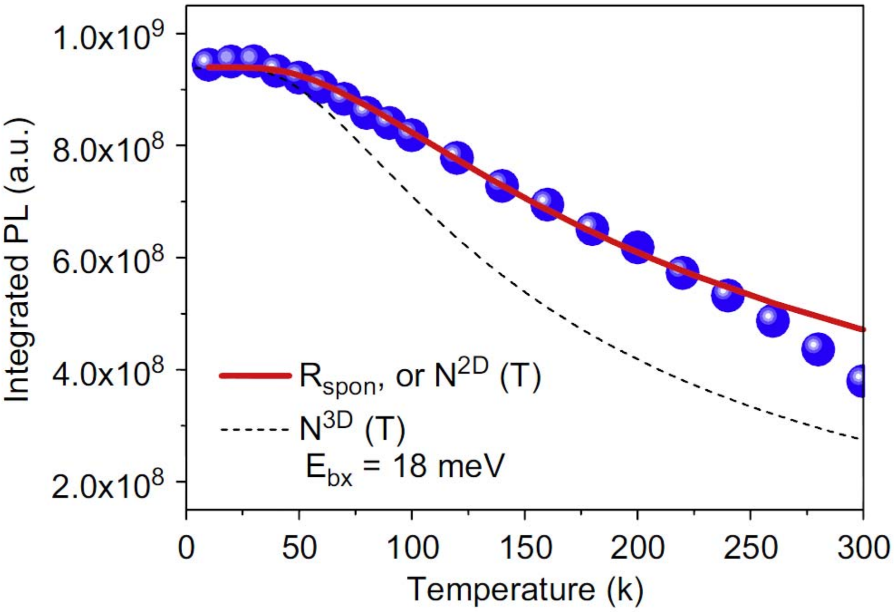

Figure 7.2: Integrated PL intensity from spectra shown in Figure 7.1 as a function of temperature. The red (solid) curve is calculated with the exciton binding energy of 18 meV using either Eq. [14] or Eq. [15]. The dashed curve plots the total number of excitons as a function of temperature using the 3D DOS.

7.2 Temperature dependence of time-resolved PL

Time-resolved PL data were taken in a temperature range of 10 to 300 K from the same sample we took the steady state PL spectra. They are shown in Figure 7.3. Each PL decay curve was fitted by a convolution of the system response function with a single exponential decay constant, τ_d. The fit at 100 K, as an example, is shown as a thin red curve. The value of the PL decay constant, inversely proportional to the PL decay rate, is normally dictated by radiative and non-radiative processes, i.e., $\tau_d = \tau_r / (1 + \tau_r/\tau_{nr})$, where τ_r and τ_{nr} are the respective decay constants for these two processes. The fact that decay constant, as shown in Figure 7.4, monotonically increases with temperature demonstrates that radiative exciton decay is indeed the dominant process, hence, $\tau_d \sim \tau_r$. This key evidence clearly supports the assumption used in the rate equation [13].

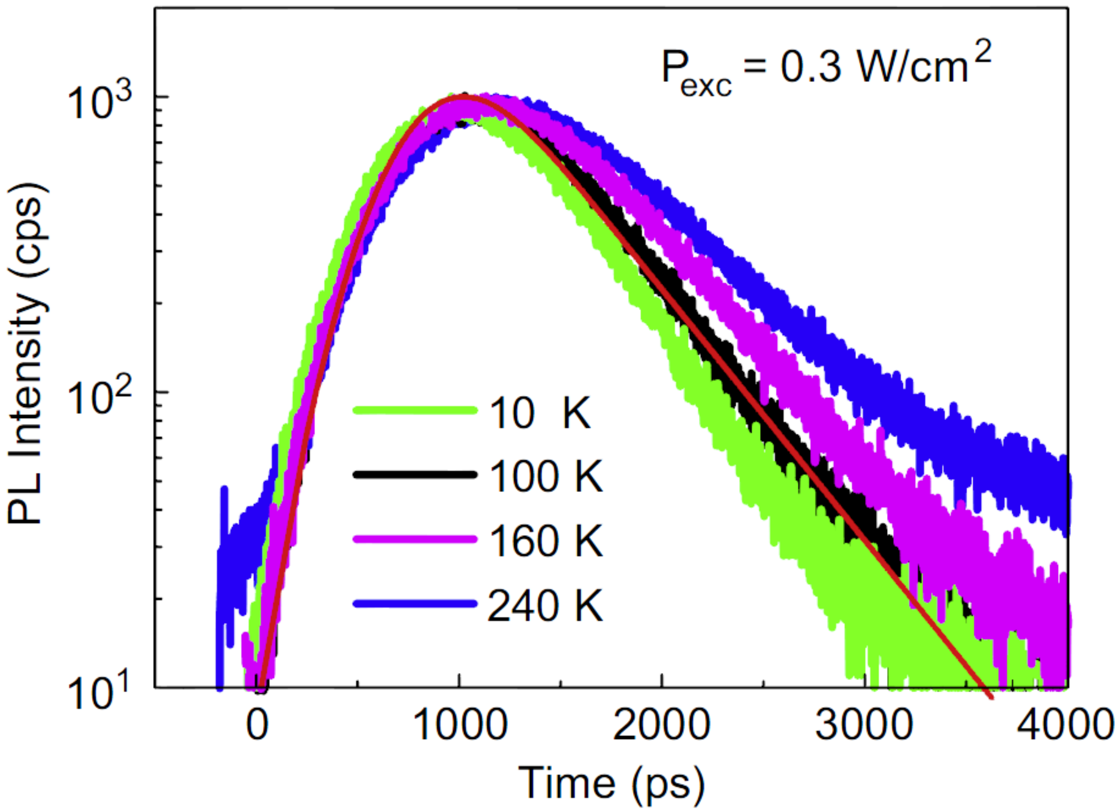

Figure 7.3: Time-resolved PL profiles at the emission peak at various temperatures. A thin (smooth) red curve shows a convolution fit at T=100 K by the Gaussian system response function and a single PL decay time of 515 ps.

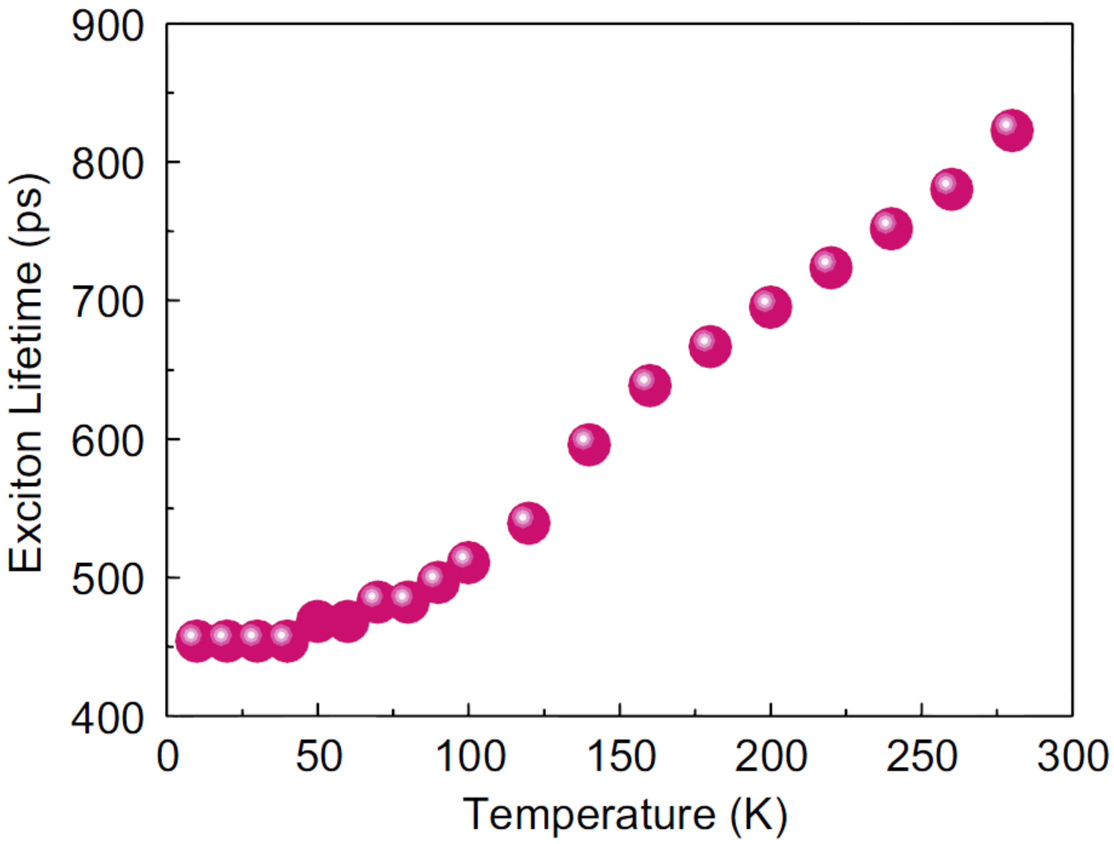

Figure 7.4: Measured exciton life time is plotted as spheres at various temperatures from 8k to room temperature.

A linear dependence of integrated PL intensity as a function of photo-excitation power at a given temperature is usually considered to be one of the necessary criteria for excitonic emissions. Figure 7.5 displays the PL spectra as the laser excitation power increases from 0.03 to 100 mW at 12 K. For this experiment, PL was collected and delivered through an optical fiber bundle manufactured by Ocean Optics. The PL spectra were not spectrally corrected since we were only interested in the relative integrated PL intensity as a function of increasing photo-excitation power. The integrated PL intensity vs. excitation power is displayed in Figure 7.6 showing near three orders of magnitude of the PL linearity over the excitation power. The thin solid line shows the gradient of one indicating constant PL efficiency over the four orders of magnitude change in photo-excitation power. This linear excitation power dependence further validates the exciton model manifested by Eq. [14].

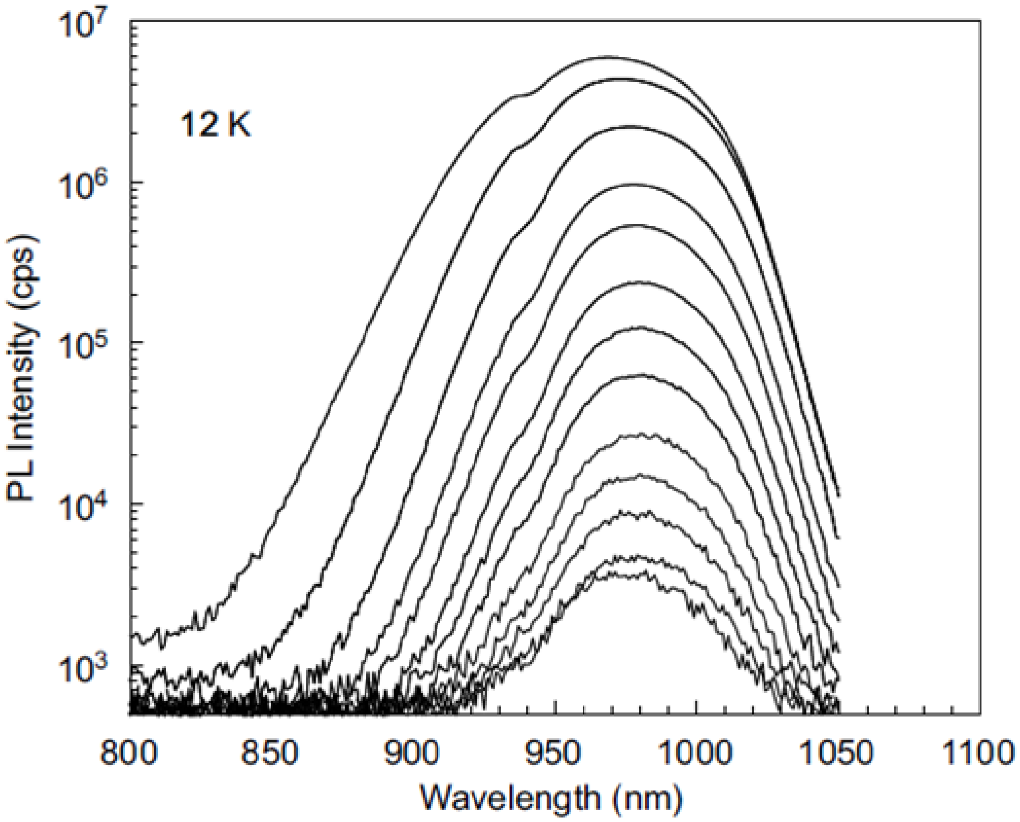

Figure 7.5: PL spectra at 12K with laser excitation power from 0.03 to 100 mW. The maximum exciton density is estimated to be on the order of 10^{16} cm^{-3}. Note the spectra are not spectrally corrected and small dip in the spectra at 945 nm is due to the fiber used to collect PL.

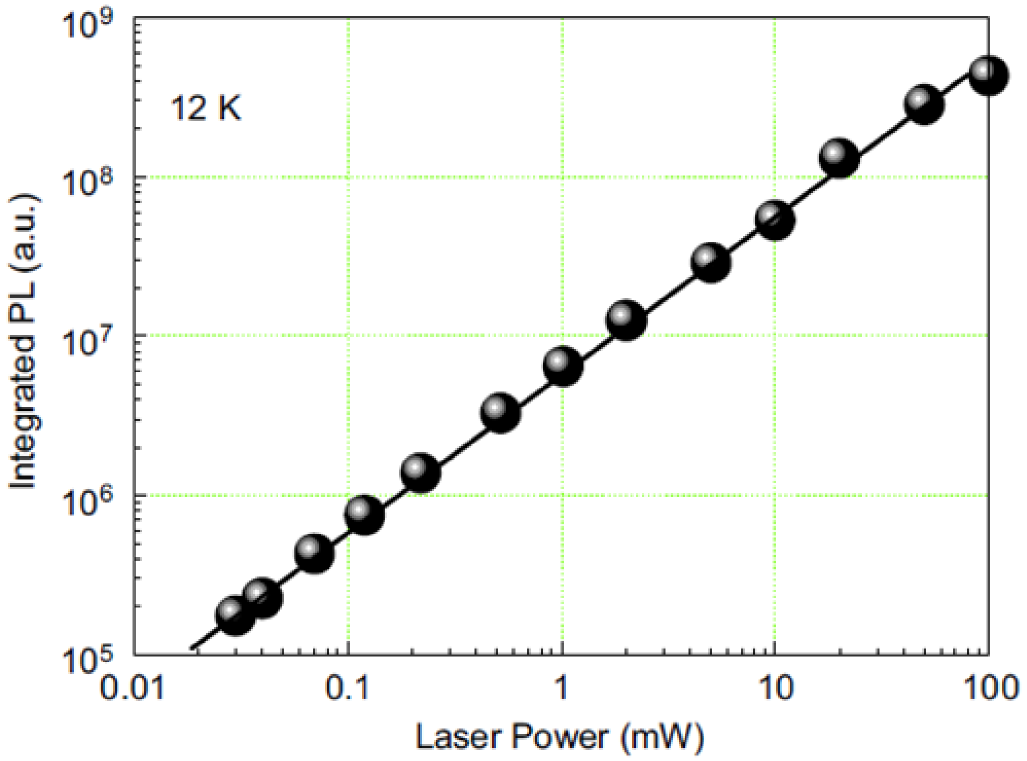

Figure 7.6: Integrated PL intensity shown in Figure 7.5 vs. excitation laser power. The thin line indicates the PL linearity with laser excitation power.

Although the PL linearity on photo-excitation power over the four orders of magnitude without saturation up to the maximum exciton density of ~ 10^{16} cm^{-3} suggests that the origin of PL is intrinsic rather than extrinsic, we provide more evidences next to confirm that the excitons in our exciton model are free excitons (FE), not a kind of bound excitons (BE) such as bound to neutral or ionized donors (acceptors) or even a combination of various types of bound excitons. A strong evidence of the FE assignment comes from the spectral shape of PL; it clearly shows a broad single peak with a high energy tail gradually developing as the sample temperature increases from 10 to 300 K. If the measured PL were from BE, we would expect a FE shoulder getting strength as the sample temperature increases while the relative strength of BE to FE decreases. This scenario of the temperature dependent PL from BE with an additional binding energy to impurities on an order of 20 meV has been observed for ZnO[84,85] and GaN[86,87]. The fact that we do not observe a shoulder on PL spectra is consistent with the intrinsic PL origin.

7.3 Mid-infrared absorption

According to Hayne's rule,[88] donor (acceptor) energy levels would be about 120 to 180 meV below (above) the conduction (valence) band edge if the deduced 18 meV were considered as an additional binding energy to these impurities. If there were a substantial amount of impurities, we would expect to observe one or more of the following impurity related optical transitions: (1) donor-electron to valence band hole, (2) conduction band electron to acceptor-hole, (3) donor electron to conduction band, and (4) valence band electron to acceptor hole. Since we did not measure any PL from 1050 to 1500 nm, the optical transition of (1) or (2) was not detectable. For the (3) or (4) transition, a Fourier transform infrared (FTIR) spectrometer was used to measure the impurity absorption features. As shown in Figure 7.7, other than a weak absorption spike at 83 meV[38] and a doublet at 290/293 meV[89,90] displayed in the inset due to residual CO_2, there are no other absorption features in the energy range of 65 to 325 meV on the measured absorbance spectrum at room temperature, taking from a 400 nm $CsSnI_3$ thin-film deposited on a CsI substrate. The absence of any optical transitions of (1)–(4) demonstrates that the density of impurities (if there are) is below the FTIR impurity detection limit of 0.03 ppm,[91] which is equivalent to an impurity density of ~ 10^{16} cm^{-3}.[92] This demonstration is consistent with the high PL efficiency even up to room temperature and further confirms our FE assignment.

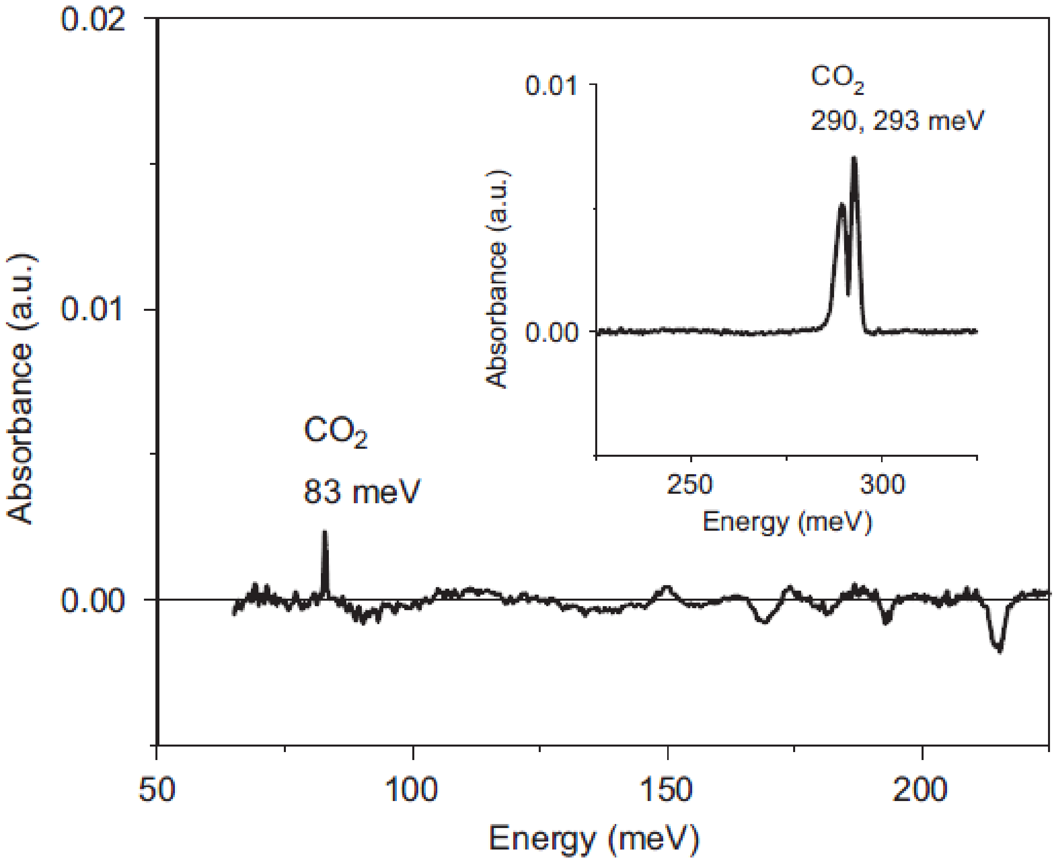

Figure 7.7: FTIR absorbance spectrum of $CsSnI_3$ thin film on CsI substrate at room temperature. A spike at 83 meV and a doublet at 290/293 meV displayed in the inset are due to residual CO_2 gas in the sample compartment. No infrared optical transitions were measured due to impurity states within the $CsSnI_3$ energy gap.

7.4 Two-dimensional exciton justification

We now turn to the discussion on why the exciton binding energy in this semiconductor compound is much larger than expected[81,82] based on its value of energy band gap, 1.32 eV at 300 K. As shown in Figure 7.8, the data point of 18 meV for $CsSnI_3$ as a filled circle appears to be an outlier. We start with the assumption that the photo-generated excitons in this material are two-dimensional (2D) excitons residing in the 2D layers of SnI_4 tetragons as suggested by the high resolution TEM image shown in Figure 5.2 (c). There are two verifiable outcomes based on this assumption. First, the energy independent 2D excitonic density of states (DOS) is distinctly different from the energy dependent DOS for one-dimensional or two-dimensional exciton motion. Using the 2D DOS and the Boltzmann distribution, the total number of excitons at a given temperature is given by

$$N^{2D}(T) = N_0\left[1 - \exp\left(-\frac{E_{bx}}{K_B T}\right)\right], \qquad [15]$$

where N_0 is the number of total excitons at 0 K. The temperature dependent integrated PL should be proportional to the total number of excitons that can be maintained in the film at a given temperature. Therefore, Eq. [15] can also be used to fit the data in Figure 7.2. As it is obvious just from the form of Eq. [15], the fit to the experimental data should be excellent, which supports the 2D exciton assumption from the view of energy-independent DOS. We also calculated the total exciton number as a function of temperature using the three-dimensional DOS to fit the data as shown in Figure 7.2 by dashed curve. It clearly fails to fit the data. Second, if the assumption is correct, a three-dimensional exciton binding energy for this compound would be one fourth of 18 meV, i.e., 4.5 meV. This number is consistent to the band energy gap scaling law for exciton binding energy, which is plotted as a solid line in Figure 7.8. Although there were reports on natural 2D excitons in PbI_{4^-}[93,94] and $PbCl_{4^-}$ based[95] inorganic–organic hybrid materials, the physical reasons why the excitons in this material prefer 2D motion awaits further investigations.

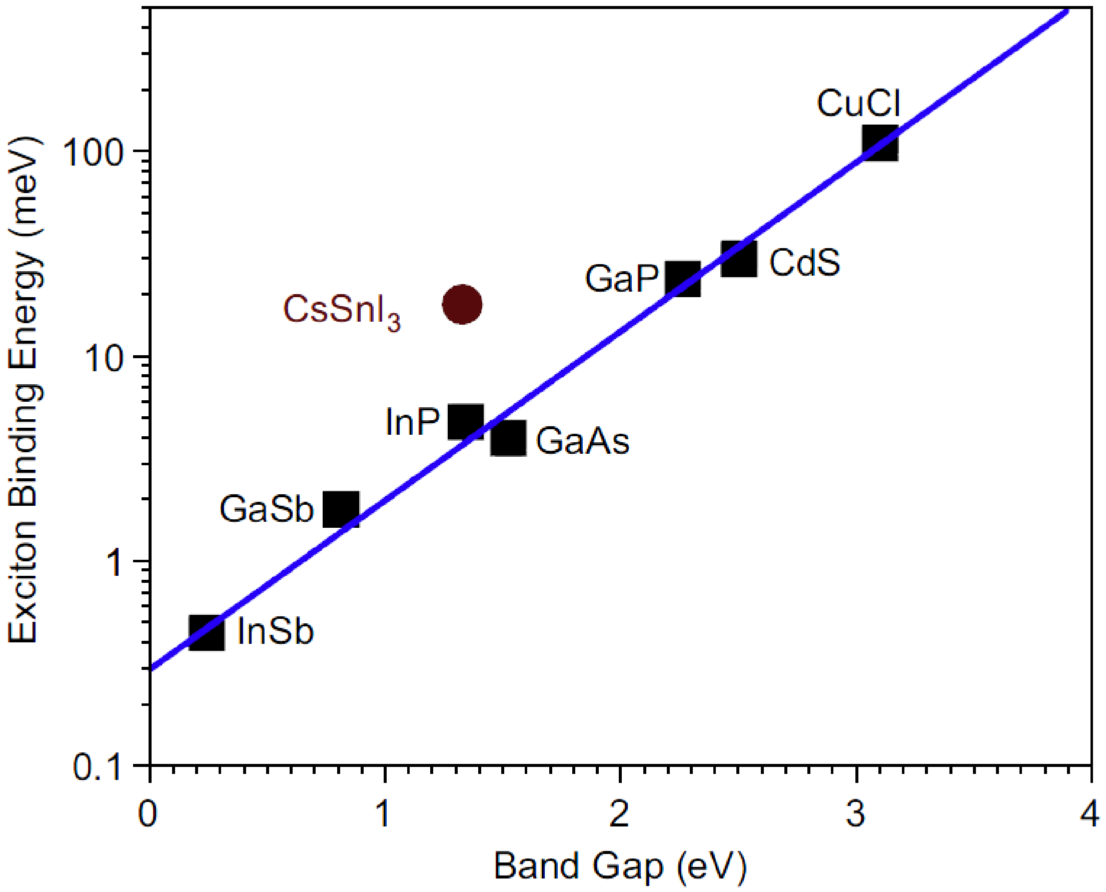

Figure 7.8: Exciton binding energies in various semiconductors (filled squares) plotted as their host semiconductor band gap energy, E_g. The exciton binding energy in $CsSnI_3$ is indicated as a filled circle. The linear line is calculated by the expression $E_{bx}(meV) = 0.3e^{1.9Eg(eV)}$.

CHAPTER 8: Temperature Dependence of $CsSnI_3$ Band Gap

The electronic band gap (E_g) is one of fundamental parameters of a given semiconductor in terms of its electric and optical properties. One of the interesting properties of $CsSnI_3$ is the strong and linear increase of the band gap with increasing temperature, which is opposite to what have been observed for the most of common semiconductors. Normal behavior in the temperature dependence of band gap is that measured E_g (T) curves show a monotonic decrease with temperature non-linearly at low T and linearly at high T. However, there are some exceptions which exhibit anomalous temperature behaviors. An early example is PbTe.[96] A blue energy gap shift was reported for this material in the temperature range from 100 to 300 K. In addition, the measured band gaps of CuBr and CuCl increase monotonically from near zero to room temperature.[97] More recently, a similar anomalous behavior has been observed for PbS.[98] The reason for this anomalous band gap behavior is not quite clear yet and needs to be further investigated. Exploring new materials with an anomalous temperature dependence of band gap remains interesting and helpful for fully understanding this fundamental problem.

PL experiments in this work were carried out by the NanoLog apparatus introduced in Chapter 4. A $CsSnI_3$ thin film sample (silicon substrate in this case) was mounted on the cupper finger of a closed-cycle optical cryostat, which is capable of having temperature variation from 9 to 350 K. Excitation wavelength was 500 nm with a pass band of 5 nm for steady state PL. Excitation power density was about 0.5 mW/cm^2. Spectra were corrected by using a standard light source purchased from Ocean Optics Inc.

Normalized PL spectra from 9 to 300 K are displayed in Figure 8.1. The full width at half maximum (FWHM) of each spectrum is shown in the inset of this figure. Two important features are readily identified: (1) PL peak shifts to shorter wavelength, and (2) PL spectrum broadens as the sample temperature increases from 9 to 300 K. We now turn to discuss how to deduce accurate band gaps from PL spectra at various sample temperatures. There are two contributions to the PL line width broadening. One is the temperature dependent asymmetric thermal broadening on the high energy tail of a spectrum arising from more energetic excitons. A constant two-dimensional density of states and a Boltzmann thermal distribution with an exciton temperature (T_x) were used for this part of line shape. The other one is due to the symmetric broadening resulting from both the inhomogeneous broadening because of the nature polycrystalline compound and the homogeneous broadening originated from e-p interactions. Main reasons for inhomogeneous broadening may include composition fluctuations and granular boundaries. We assume this symmetric broadening to be a Gaussian with a variance of σ. Combining the above mentioned two contributions, a PL spectrum at a given sample temperature can be fitted by the following convolution expression:

$$PL(E) = G(E,\sigma) * exp(-\frac{E-E_g+E_{bx}}{K_B T_x}) \qquad [16]$$

All measured PL spectra from 9 to 300 K were fitted by Eq. [16]. The calculated spectra are shown in Figure 8.1 (b). To demonstrate the quality of fitting, two measured PL spectra at 80 and 220 K (discrete symbols) are plotted in an intensity-log scale in the inset along with the calculated spectra (solid-line curves). The spectrum fit over three orders of magnitude is highly satisfied for all spectra except a small deviation at low energy side for a few spectra with temperature greater than 200 K. However, this deviation will not affect the accuracy of the band gap determination. Both fitting parameters σ and T_x are the sample temperature dependent. We will discuss these two parameters elsewhere. The focus point in this chapter is the deduced band gap at different temperature, which is summarized in Figure 8.2 as solid spheres. This plot presents a salient feature: the band gap follows a positive linear-dependence in the temperature range we studied although it tends to be flat at temperature below 20 K. This feature is referred as the anomalous behavior of band gap in literature,[97,98] and the reason still needs to be further investigated.

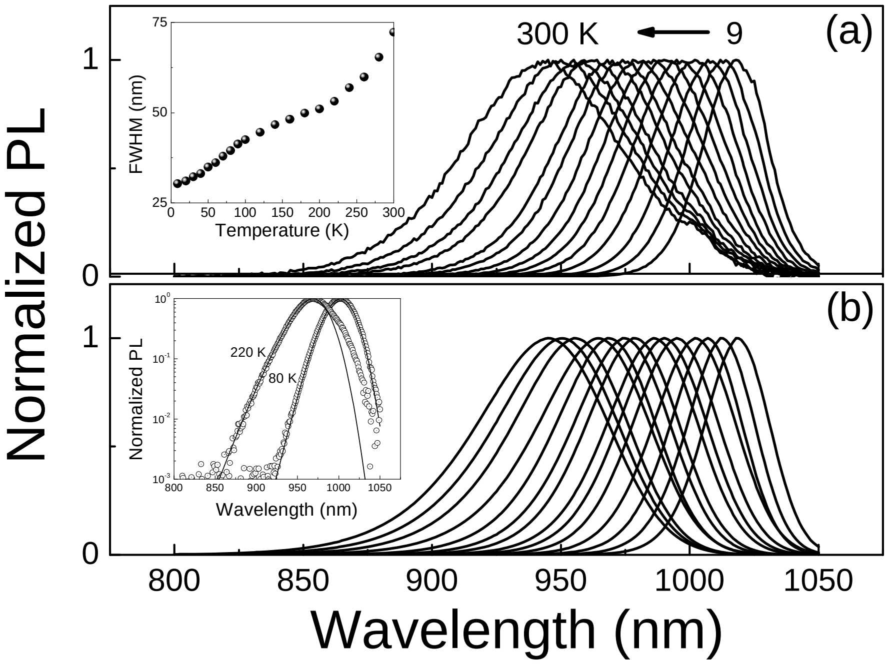

Figure 8.1: (a) Normalized PL spectra measured at various temperatures from 9 to 300 K. The inset shows the temperature dependence of the FWHM for the measured PL spectra. (b) Calculated PL spectra using Eq. [16], which were matched to each measured PL spectrum to obtain band gaps at different temperatures. The inset displays the two examples of spectrum fitting at 80 and 200 K. Discrete symbols represent the measured PL, while solid curves are calculated PL spectra.

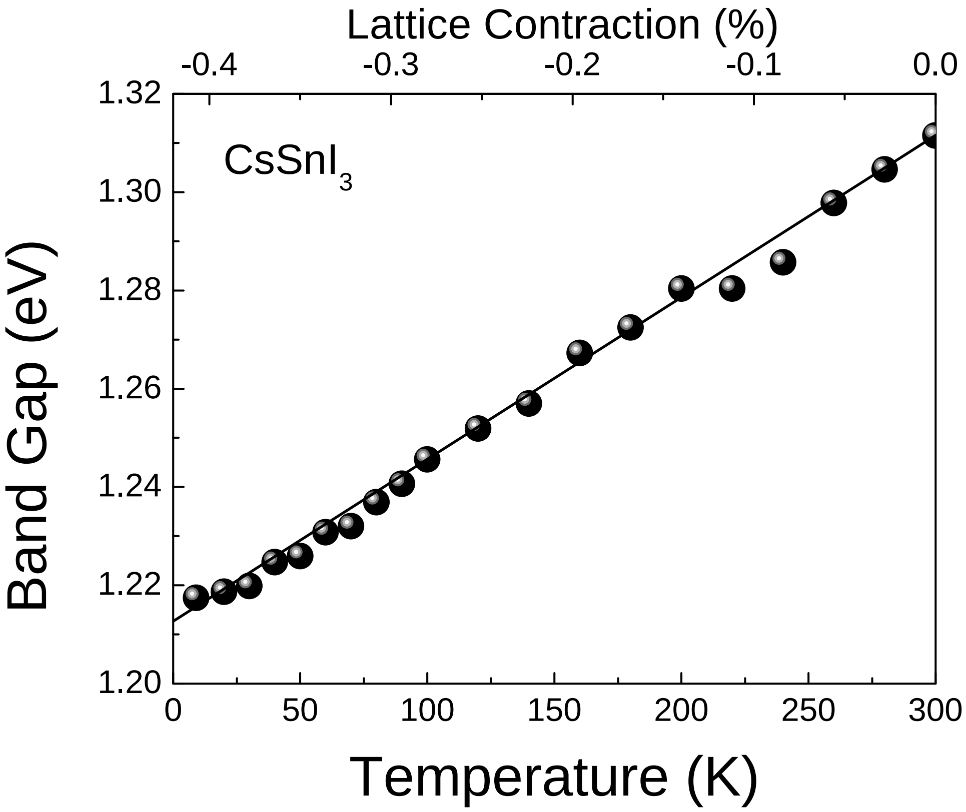

Figure 8.2: Band gaps of $CsSnI_3$ at various temperatures deduced from PL spectra (solid spheres with bottom axis) and the band gap variation with lattice contraction obtained from first-principles calculations (solid line with top axis). The top axis is the relative lattice contraction, $\Delta a/a_0$, where a_0 is the lattice constant at room temperature.

The solid line in Figure 8.2 shows the calculated E_g vs. $\Delta a / a_0$ (top axis). It can be seen that the band gap decreases linearly as lattice constant contracts from its room temperature values. It requires a linear lattice change of 0.42% from room temperature to 0 K to match the measured band gap variation with temperature. The top axis $\Delta a / a_0$ and bottom axis can be overlapped by assuming a constant linear thermal coefficient α_L with a value of 0.42/100/300 = 1.40×10^{-5} K^{-1}. Thus the solid line can be recognized as the calculated E_g vs. T due to thermal expansion or contraction. The calculated curve agrees with the experimental data very well except at low temperature less than 20 K. This agreement may support an assumption that the thermal expansion is proportional to temperature in this material and its effect dominates the variation of band gap with temperature.

CHAPTER 9: Schottky Solar Cells Based on $CsSnI_3$ Thin Films

9.1 Fabrication of Schottky solar cells based on $CsSnI_3$

The $CsSnI_3$ Schottky junction cell was fabricated on a Pyrex glass substrate. Thin metallic layers of Ti (100 nm) and Au (20 nm) were sequentially coated through the first shadow mask onto the glass substrate via E-beam evaporation. Six pairs of $SnCl_2$/CsI were deposited through the second shadow mask by E-beam (for CsI) and thermal (for $SnCl_2$) evaporation. The total thickness of the $SnCl_2$/CsI stack was about 750 nm. The sample was brought to the ambient conditions and annealed at 175 ^{o}C on a hotplate for 1 minute. The annealing process converts the $SnCl_2$/CsI stack to a black thin-film of $CsSnI_3$, which has intense PL peaking at ~ 950 nm.[99] The sample was then sent into a sputtering chamber to coat a thin ITO layer through the third shadow mask. The ITO film was measured to have a thickness of ~ 80 nm and a sheet resistance of ~ 50 ohm/square. A schematic diagram of the finished structure is shown in Figure 9.1. The active area between Ti/Au, $CsSnI_3$, and ITO is about 4 x 4 mm^2. The Ti/Au and ITO pads were used for the J-V measurements.

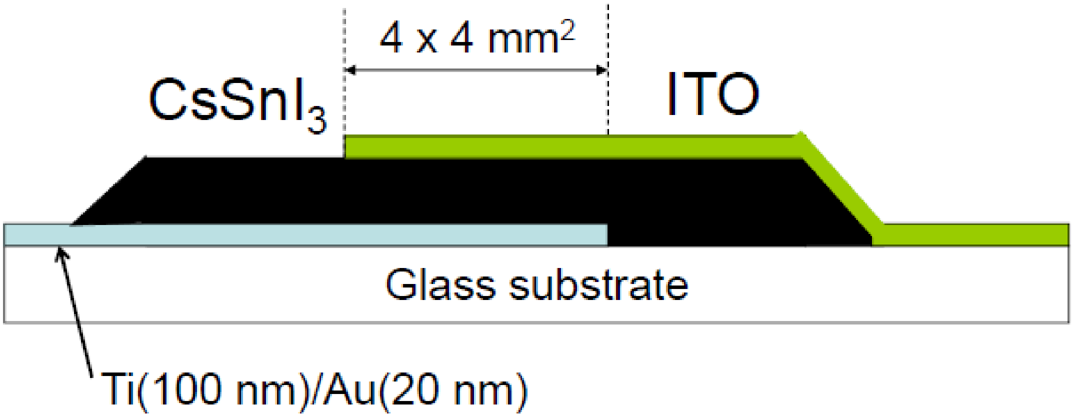

Figure 9.1: A schematic layer structure of the Schottky solar cell based on $CsSnI_3$.

9.2 Energy band diagram for Ti/Au/$CsSnI_3$/ITO

The detailed energy levels in reference to the vacuum level for individual materials of Ti, Au, $CsSnI_3$, and ITO are given in Figure 9.2 (a). The commonly used work-function values are given here although there is a small range of variation due to its crystalline orientation for Au and due to the exact ratio of indium and tin for ITO. For $CsSnI_3$, its energy band gap was determined by optical spectroscopic methods,[99] while the position of valence band maximum has been determined recently by ultraviolet photoemission spectroscopy.[100] When they are brought into contact as schematically depicted in Figure 9.1, a common Fermi level is established because of the occurrence of charge transfers at the three interfaces of Ti/Au, Au/$CsSnI_3$, and $CsSnI_3$/ITO as shown in Figure 9.2 (b). The exact value of built-in potential energy barriers at the Au/$CsSnI_3$ and $CsSnI_3$/ITO are unknown due to the lack of precise Fermi level position in reference to the valence band maximum in $CsSnI_3$. However, due to a work-function difference of 0.6 eV between the Au and ITO, it is expected the built-in potential energy barrier near the interface of Au/$CsSnI_3$ is much larger than that near the interface of $CsSnI_3$/ITO as indicated in Figure 9.2 (b). Since the exciton binding energy in $CsSnI_3$ is 18 meV,[73] about a half of photogenerated carriers is expected to form excitons initially even under the built-in electric field and another half is in form of free electrons and holes. The majority of excitons will be dissociated into free electrons and holes by the built-in electric field. They join other electrons and holes and are driven to the two opposite electrodes to established the open-circuit voltage, V_{oc}, when the cell is not connected to load, or to generate the short-circuit current density, J_{sc}, when the cell is shorted.

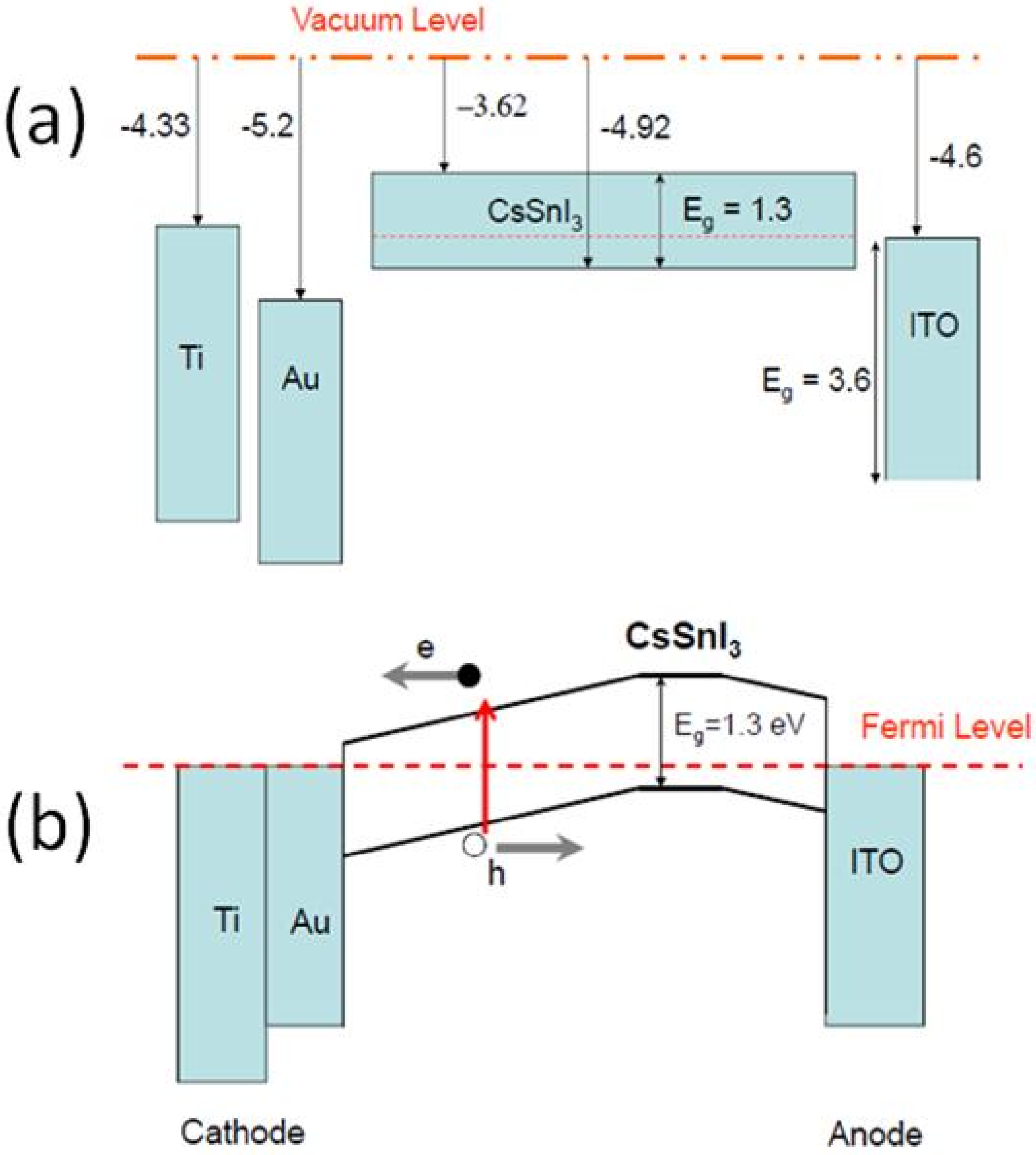

Figure 9.2: (a) Energy levels for Ti, Au, $CsSnI_3$, and ITO in reference to the vacuum level; and (b) the band diagram of the Schottky solar cell based on $CsSnI_3$. The unit of energy is eV.

9.3 Results on photocurrent density vs. voltage

In Figure 9.3, a typical set of IV curves in dark and under the light illumination of Xe lamp (Horiba, NJ) is shown. The light excitation power density (P_{exc}) was measured to be 50 mW/cm^2 (denoted as P_0) about a half of the standard air mass 1.5 (AM 1.5) sunlight radiation. The $V_{oc} = 0.42$ V and $J_{sc} = 4.80$ mA/cm^2 were obtained, respectively. The value of PCE is only about 0.9 % limited by the low filling factor of 22 %, mainly because of the low shunt resistance and large series resistance. It should be noted that the maximum photocurrent of 15 mA/cm^2 was measured at P_0, showing a great potential to improve J_{sc}. It can be as high as 30 mA/cm^2 under the AM 1.5 radiation, assuming that J_{sc} is proportional to the light intensity. Also indicated on the figure is the voltage (V_{flat}) at which the band bending disappears when the cell is operated at 0.62 V. This value is consistent with the work-function difference of 0.6 V between the anode and cathode.

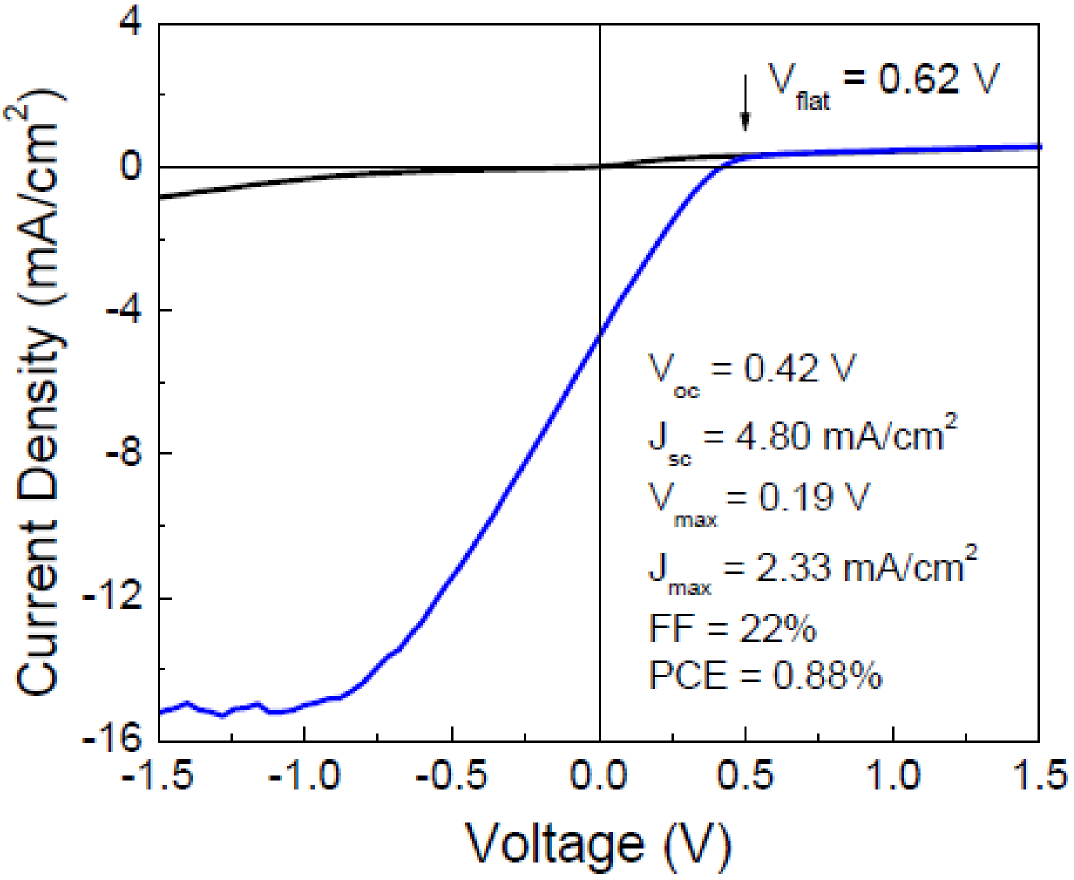

Figure 9.3: Photocurrent vs. voltage in dark (black) and under light illumination (blue) with a power density of 50 mW/cm^2, equivalent to the half of the intensity of AM 1.5 standard radiations.

9.4 Solar cell performance - dependence on light intensity

To understand the major carrier pathways and how the density of quasi-equilibrium carriers affects the band bending for the illuminated Schottky solar cell, the J-V curves were measured under various light excitation power densities as displayed in Figure 9.4. As P_{exc} increases, J_{sc} increases as expected since the number of carriers increases available for conduction. It may also indicate that a negligible fraction of excitons-carriers that are involved in nonlinear carrier trapping processes. The value of V_{oc} was measured to increases as P_{exc}

increases. Figure 9.5 (a) and (b) summarize the variations of J_{sc} and V_{oc} with P_{exc}. It is important to discuss the $\ln(P_{exc})$ dependence of V_{oc} since this relationship characterizes how ideal the Schottky junction is. The data points in Figure 9.5 (a) were linearly fitted (solid red line) with the expression of $V_{oc} \sim (nk_BT/q)\ln(P_{exc})$ according the Schottky junction model,[101] resulting a value of 2.8 for the ideality factor n. This relatively large value may be originated from the shunt parasitics[102] especially near the device edges, and may also be due to the interface states[103] near the interface of $CsSnI_3$/ITO.

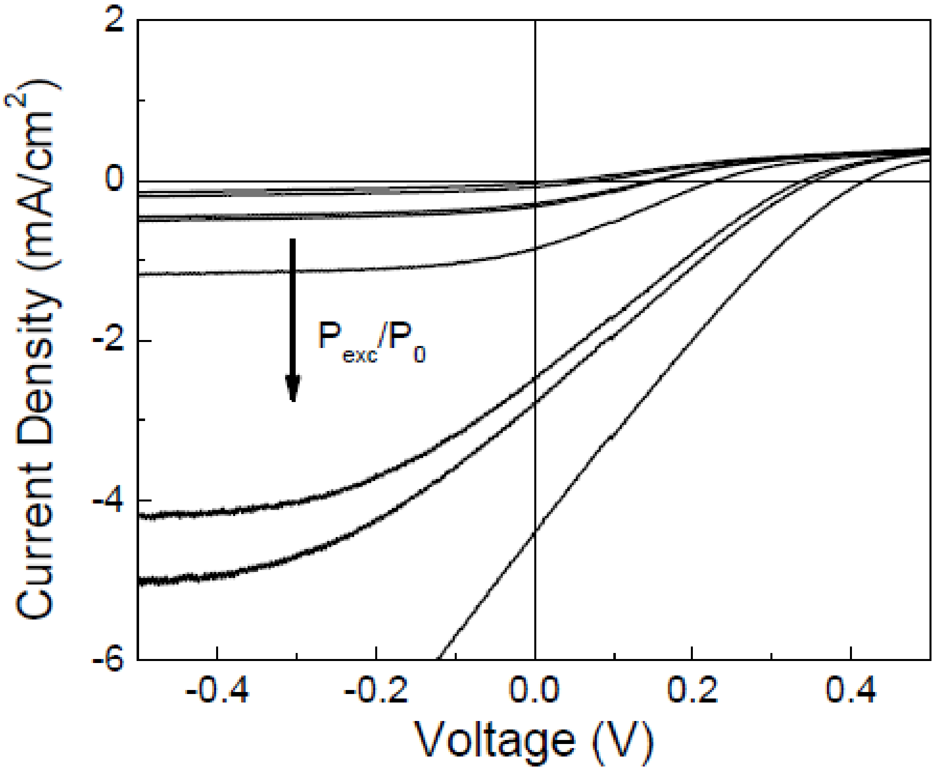

Figure 9.4: The Schottky solar cell I-V response curves measured at different light illumination power densities. P_0 = 50 mW/cm^2.

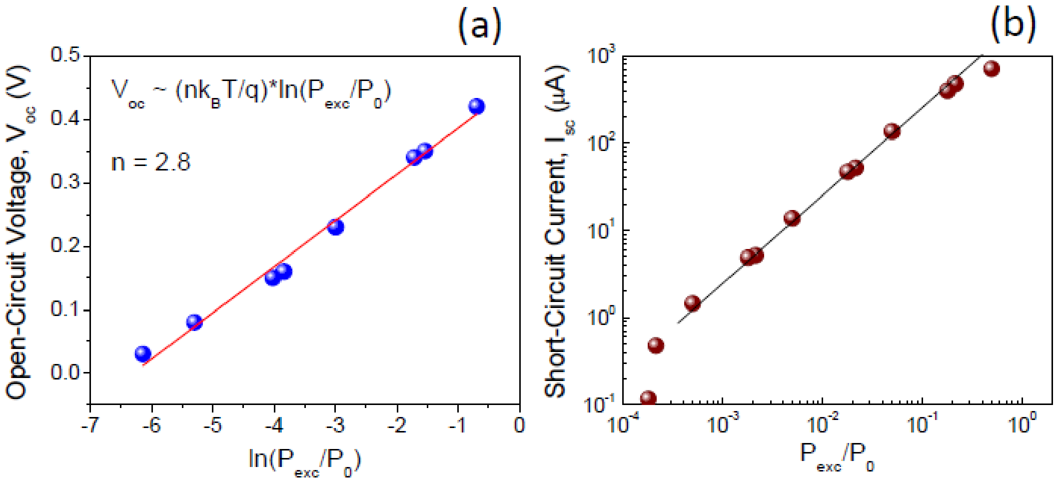

Figure 9.5: (a) Open-circuit voltage vs. $\ln(P_{exc}/P_0)$, and (b) short-circuit current vs. P_{exc}/P_0. The solid line in (a) is a linear fit to the data, while the solid line in (b) is to guide the eyes.

9.5 Spectrally resolved photocurrent and its comparison with PLE

Spectral response of a given solar cell should be fully understood in order to further improve the cell's PCE. For the $CsSnI_3$ based solar cell, since the band gap of $CsSnI_3$ is 1.3 eV at 300 K, right in the narrow region of optimal band gaps for the Shockley-Queisser maximum efficiency limit of a solar cell, it is particularly relevant to discuss its spectral response. Figure 9.6 displays the photocurrent under the light illumination with different colors, which was obtained from a combination of a Xe lamp and a calibrated monochromator (Horiba, NJ). The center wavelength of light illumination for each IV curve is indicated on the figure. A bandwidth of 5 nm was used for all color. The light intensity for each wavelength was measured, which was used to calculate the value of J_{sc} per μW for different wavelength displayed in Figure 9.7. Inspecting the data in Figure 9.7, there are two important features. First, it should be noticed that the IV curves under light excitation with the central wavelengths of 350 and 400 nm are shifted to the 2nd quadrant; while for all other colors are shifted to the 4th quadrant. This wavelength dependent IV shift can be understood only if the un-intentionally doped $CsSnI_3$ is a p-type material as illustrated by the band diagram in Figure 9.2 (b). For the photo-excitation with the wavelength of 350 and 400 nm, carriers are mainly generated near the $CsSnI_3$/ITO interface within 100 nm. Holes are collected by Ti/Au contact and electrons are collected by the ITO contact. For the photo-excitation with the central wavelength greater than 450 nm, the reverse carrier collection process is dominant; hence, it behaves as a conventional Schottky solar cell. Since all over contribution of ultraviolet light is much smaller than the major contribution from visible and near infrared light, the $CsSnI_3$/ITO contact can be considered as a quasi-ohmic-contact (anode). It should be mentioned here that the p-type characteristics of unintentionally doped, as-grown $CsSnI_3$ was directly determined by measuring the positive Seebeck coefficient and by Hall measurements.[104] The second feature is the spectral response of J_{sc} as shown in Figure 9.7. Each individual data point (sphere) represents the measured short-circuit current density divided by the light intensity for a given wavelength. The shaded area is used to guide eyes for all over the spectral response of the $CsSnI_3$ based solar cell. It effectively covers the visible and near infrared regions as we expected based on the band gap value of 1.3 eV for $CsSnI_3$.

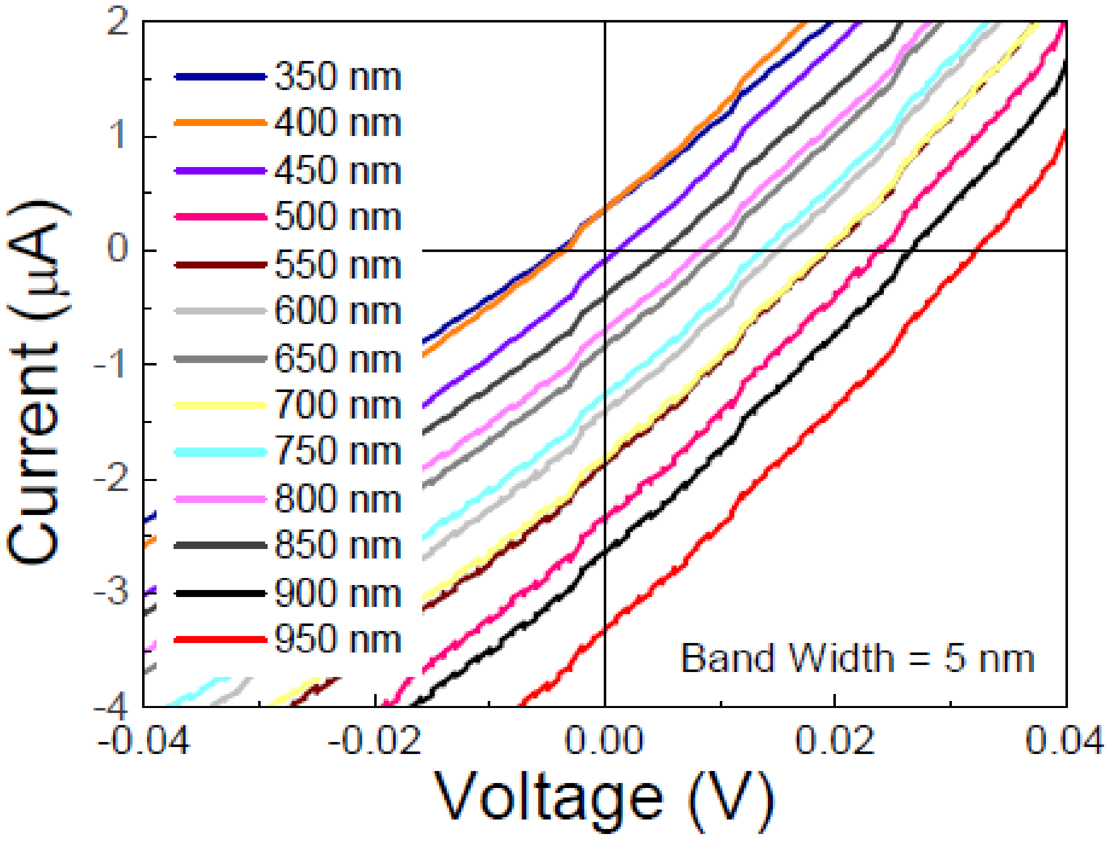

Figure 9.6: (Color online) Photocurrent vs. voltage at various light illuminations.

As we reported in our previous work,[99] $CsSnI_3$ has extremely high photoluminescence quantum efficiency. In order to confirm the mixed exciton-carriers system responsible for photoluminescence is also the origin for photocurrent. PLE spectrum was measured by the apparatus consists of the same combination of Xe-lamp/monochromator used for photocurrent measurements. PL at 950 nm, near the band edge, excited by the light illumination of different wavelengths, was selected through an emission spectrometer and collected by a photomultiplier tube (Hamamatsu P2658P), with an integration time of 0.5 s. The room temperature PLE spectrum is plotted in Figure 9.7. The intensity of PLE spectrum is inverted in order to compare it with the negative value of J_{sc}. Because of the similar spectral response of PLE and photocurrent, it can be concluded that the same relaxed carriers-excitons are responsible for high quantum yield photoluminescence and for photocurrent. It also confirms the spectral response in near infrared region is higher than that in the visible region. This particular feature may be useful for semi-transparent solar cell applications.

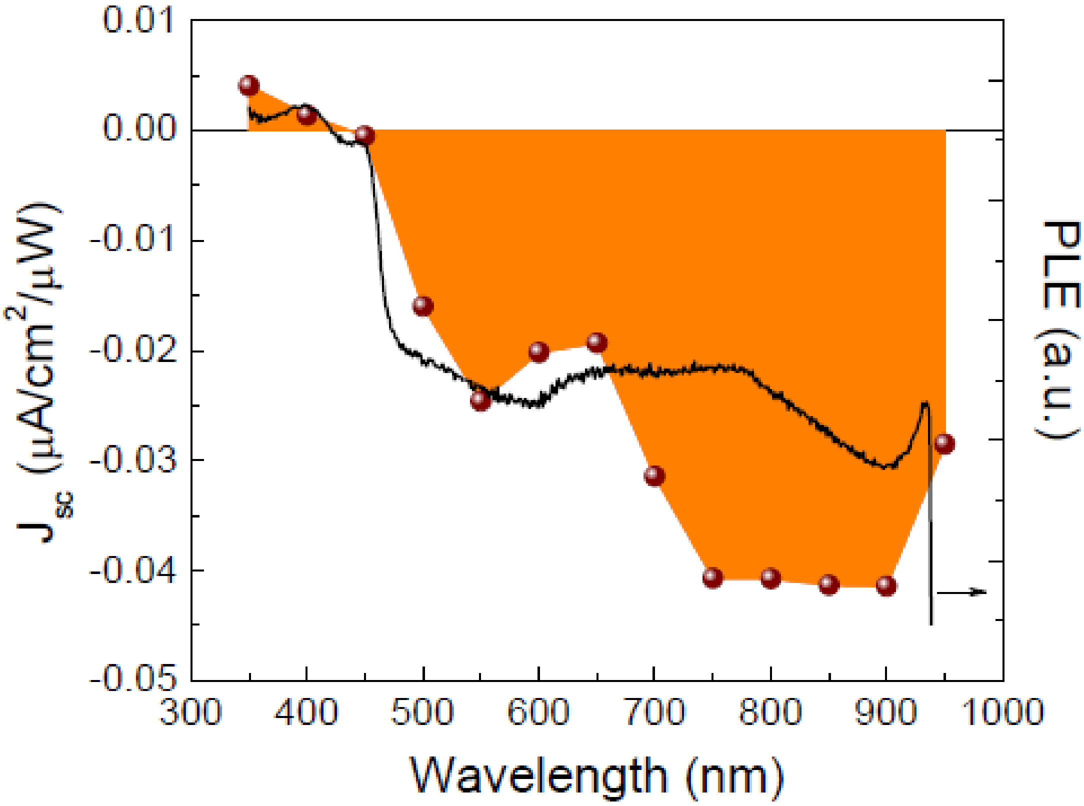

Figure 9.7: Short-circuit current density (left axis) divided by the light intensity used to generate it at different wavelengths, and PLE spectrum (right axis) with PL detection set at 950nm at room temperature.

CHAPTER 10: Challenges for Making Use of $CsSnI_3$

A big challenge of this promised material is the stability issue. In our Applied Physics Letters paper[99] we have reported that $CsSnI_3$ films synthesized by the vacuum method will degrade in a few days under a normal ambient condition without any protections. However, if they are stored in dry N_2 gas or encapsulated, they can be free of degradation. We believe this is because of oxygen and water. We observed that the black-γ phase $CsSnI_3$ films synthesized by the vacuum method will degrade to the yellow phase first, but if we re-annealed them in time, they will get back the black-γ phase again. This degradation process would be accelerated to around 1 min in water. As we prepared the “ink” for drop coating, we have the black ink first immediately when we mixed SnI_2 ethanol solution with CsI aqueous solution. The black precipitation was proved to be black-γ phase $CsSnI_3$ by PL measurement in a quartz cuvette. But the color of the precipitation changed to yellow in a few minutes. The exact phase transition time depends on the amount of water in the solution as discussed in Chapter 3. This is consistent with the assumption that water is a reason for degradation. Moreover, vibration and sonication would also accelerate the phase transition speed, which tells us oxygen may also involve in the degradation process.

A stability test of two $CsSnI_3$ film samples synthesized by the solution method is shown in Figure 10.1. The sample deposited by the drop-coating method was on a piece of microscope slide, and another one by the ultrasonic spray method was on a piece of ceramic. The integrated PL vs. time in days is plotted. Both of them followed an exponential degradation, and more importantly, the degradation coefficients were much smaller than the one from the vacuum method.

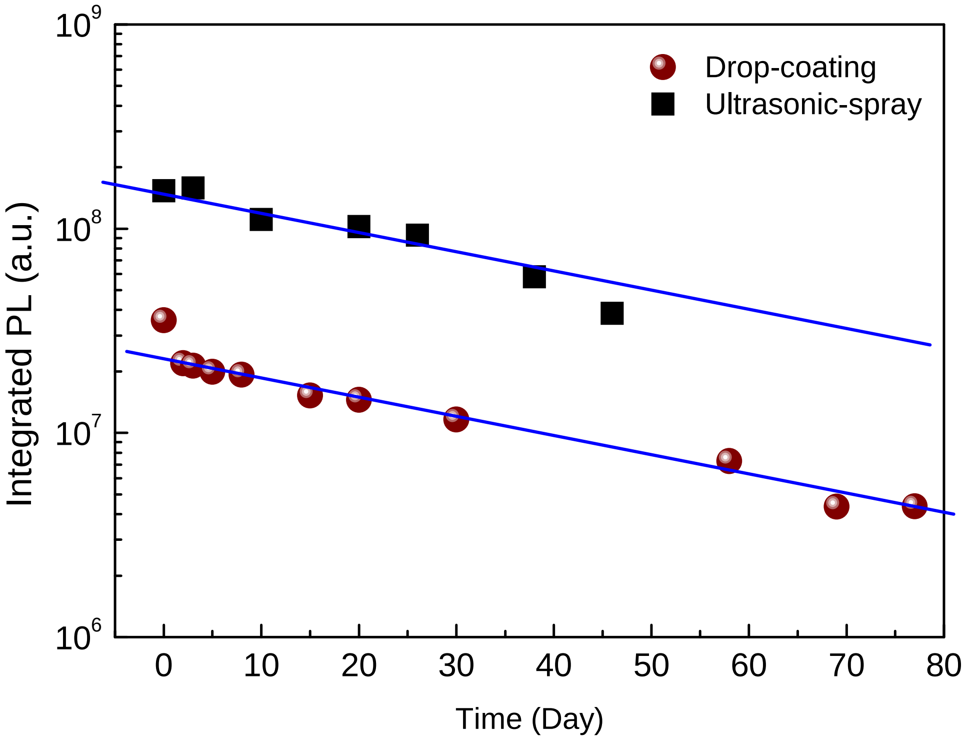

Figure 10.1: Stability test of a drop-coating sample on a piece of microscope slide (brown circles) and an ultrasonic-spray sample on a piece of ceramic (black rectangle). Integrated PL intensities at 950 nm are plotted in y-log-scale vs. day in ambient environment.

A comparison of SEM images between the vacuum and solution method are shown in Figure 10.2. This tells us the difference between the two kinds of films. The grain size measured from Figure 10.2 (a) (vacuum) was about 150 nm while in Figure 10.2 (b) (non-vacuum) was 2.5 μm, around 17 times larger. Inspecting the cross-sectional images for both of these two samples shown in Figure 10.2 (c) and (d), we can see a lot of shining dots indicating residue material and side products were all around the grains. The XRD profile in Figure 5.5 also indicates there are a considerable amount of residual CsI and CsCl. Sometimes due to non-uniform distribution or temperature on the sample during annealing, some area of the sample may have residue $SnI_2/SnCl_2$ instead of CsI. The problem is that all these materials absorb waters from air. The absorbed water will accelerate the degradation of $CsSnI_3$ films from black-γ phase to yellow phase. Therefore, as the "absorbers" are around the grains, the absorbed water will affect the $CsSnI_3$ grains. Since the films from the vacuum method have relatively small grain size, these $CsSnI_3$ grains are easily affected and will activate the phase transition in a relatively short time period. In contrast, the phase transition process (degradation) for ultrasonic-sprayed films will be relatively slow because of small grain size. When we took the PL measurement for ultrasonic-sprayed films left in ambient environment for days, PL came from the black-γ $CsSnI_3$ laid on deeper levels inside the grains. The color change of the films also supported this conclusion. The color for all fresh annealed films is shiny black, but after one day, vacuum-based films became totally yellow, while the solution-based films were just a little yellowish-black, more like a few tiny yellow dots on a black film. The yellow dots became more as time passed, and after a couple months, the films were like yellow dots mixed with black dots on the surface. Pictures are shown in Figure 10.3. Figure 10.3 (a) is a fresh annealed $CsSnI_3$ thin film deposited by ultrasonic spray on a piece of ceramic. Figure 10.3 (b) is the same sample but 3 months after annealed.

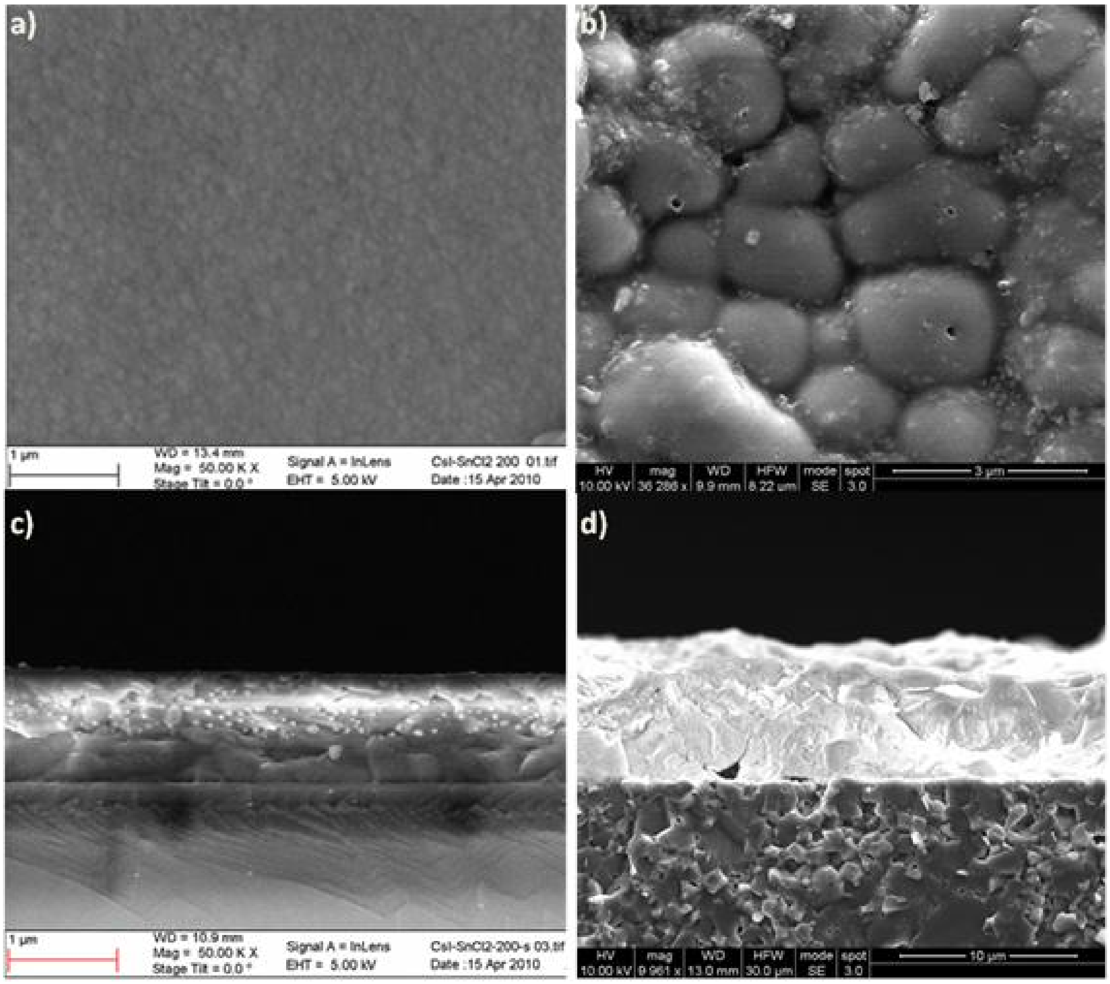

Figure 10.2: (a) SEM image for a $SnCl_2$/CsI sample deposited by the vacuum method and annealed at 200 °C on a hotplate in air. The grain size is around 150 nm. (b) SEM image for a $SnCl_2$/CsI sample deposited by the ultrasonic spray method, and annealed at 200 °C on a hotplate in air. The grain size is around 2.5 µm (c) Cross-sectional SEM image for the sample in (a). (d) Cross-sectional SEM image for the sample in (b).

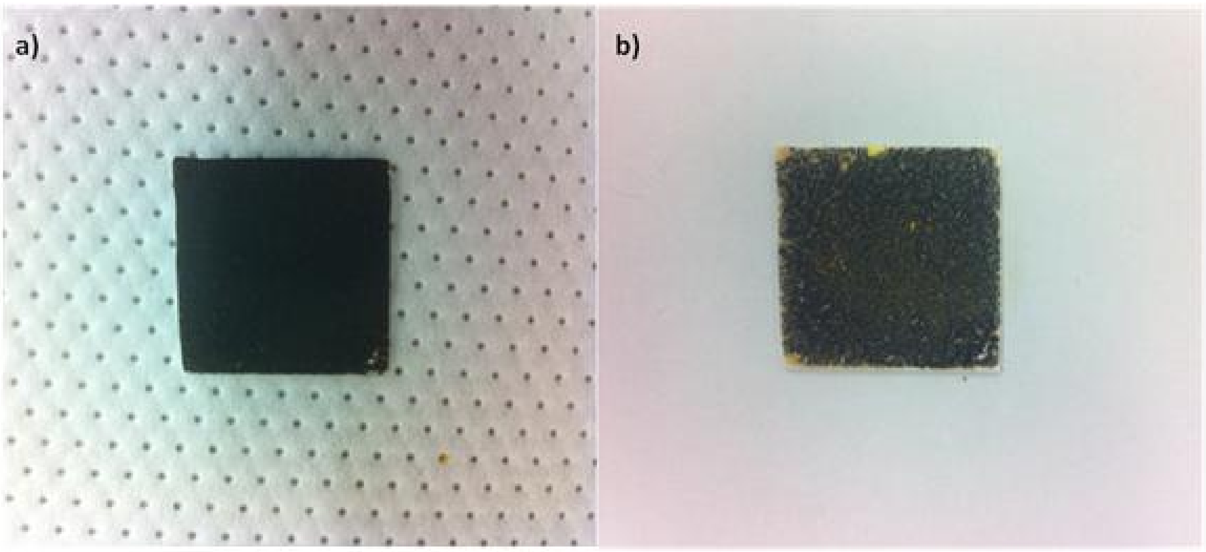

Figure 10.3: (a) An ultrasonic-sprayed $SnCl_2$/CsI sample on a piece of ceramic annealed at 200 °C. (b) The sample in (a) left in an ambient environment for 3 months.

CHAPTER 11: Future Work

To further improve the $CsSnI_3$ based solar cells, the key direction is to improve the material quality. One of ways is to use SnI_2 as the precursor material instead of $SnCl_2$ to eliminate the side product of CsCl. Another way is to purify the products based on their different solubility in ethanol. In-situ thermal annealing may also improve the crystal quality.

Based on our current design of the solar cell, we can also substantially reduce the series resistance. For example, the sheet resistance of ITO can be reduced to be less than 50 ohm/square. Detailed study of $CsSnI_3$/ITO interface is needed to reduce the series resistance and to enhance the shunt resistance.

Another direction is to find a suitable material candidate as an n-type semiconductor, to form a hetero-junction with $CsSnI_3$, similar to the technologies of CdTe and CIGS solar cells.

Last one is to control the doping so that the $CsSnI_3$ based homo-pn-junction can be fabricated, fully utilizing the optimal band gap of $CsSnI_3$.

References

1. W. Shockley and H. J. Queisser. “Detailed balance limit of efficiency of p-n junction solar cells.” J. Appl. Phys. **32**, 510 (1961).

2. D. E. Scaife, P. F. Weller, and W. G. Fisher. “Crystal preparation and properties of cesium tin(II) trihalides.” J. Solid State Chem. **9**, 308 (1974).

3. P. Mauersberger and F. Huber. “Structure of caesium triiodostannate(II).” Acta Cryst. B **36**, 683 (1980).

4. K. Yamada, S. Funabiki, H. Horimoto, T. Matsui, T. Okuda, and S. Ichiba. “Structural Phase Transitions of the Polymorphs of $CsSnI_3$ by Means of Rietveld Analysis of the X-Ray Diffraction.” Chem. Lett. **20**, 801 (1991).

5. I. Borriello, G. Gantele, and D. Ninno. “Ab initio investigation of hybrid organic-inorganic perovskites based on tin halides.” Phys. Rev. B **77**, 235214 (2008).

6. CASTEP simulation tool was used for this work: http://www.accelrys.com/. The computational results on the total potential energy and electronic states of a given crystal structure were based on the density functional module CASTEP. Prior to the energy band structure calculation of a crystal structure, the type of crystal structure was determined by an energy minimization procedure in which the potential energy was calculated by varying a lattice scaling factor, by fine-tuning the Sn-I-Sn (or Sn-Cl-Sn) titling angles in *ab*-plane and in *c*-direction, as well as by changing Cs positions.

7. J. P. Perdew, K. Burke, and M. Ernzerhof. “Generalized Gradient Approximation Made Simple.” Phys. Rev. Lett. **77**, 3865 (1996).

8. A. M. Glazer. “Simple ways of determining perovskite structures.” Acta Cryst. A**31**, 756 (1975).

9. W. W. Wendlandt. “Thermal Methods of Analysis.” John Wiley & Sons Inc., New York (1974).

10. M. E. Brown. “Introduction to Thermal Analysis: Techniques and Applications.” Springer, New York (2001).

11. A. W. Coats and J. P. Redfern. “Thermogravimetric analysis. A review.” Analyst **88**, 906 (1963).

12. H. H. Horowitz and G. Metzger. “A new analysis of thermogravimetric traces.” Anal. Chem. **35**, 1464 (1963).

13. E. Mansfield, A. Kar, T. P. Quinn and S. A. Hooker. “Quartz crystal microbalances for microscale thermogravimetric analysis.” Anal. Chem. **82**, 9977 (2010).

14. J. -M. Ntep, S. Said Hassani, A. Lusson, A. Tromson-Carli, D. Ballutaud, G. Didier, and R. Triboulet. “ZnO growth by chemical vapour transport.” J. Cryst. Growth, **207**, 30 (1999).

15. M. Shiloh and J. Gutman. “Growth of ZnO single crystals by chemical vapour transport.” J. Cryst. Growth, **11**, 105 (1971).

16. J. R. Szczech, A. L. Schmitt, M. J. Bierman, and S. Jin. “Single-crystal semiconducting chromium disilicide nanowires synthesized via chemical vapor transport.” Chem. Mater. **19**, 3238 (2007).

17. G. Calestani, J. C. Spirlet, and W. Müller. “Single crystal and film growth of actinide pnictides by chemical vapour transport.” J. Phys. Colloq. **40**, C4 (1979).

18. K. S. Sree Harsha. “Principles of Physical Vapor Deposition of Thin Films.” Elsevier Science & Technology, Great Britain (2006).

19. J. George. “Preparation of Thin Films.” Marcel Dekker, Inc., New York (1992).

20. R. C. Jaeger. “Introduction to Microelectronic Fabrication.” Upper Saddle River: Prentice Hall, New Jersey (2002).

21. T. A. Kuku. “Physical properties of thin SnO_2 and SnO_2:Sb films obtained by a photolytic method.” Thin Solid Films **142**, 241 (1986).

22. T. A. Kuku and M. Green. “Photochemical fabrication of SnO_2 and thin micropatterns from SnI_2 thin films.” Thin Solid Films **144**, L119 (1986).

23. K. X. Steirer, M. O. Reese, B. L. Rupert, N. Kopidakis, D. C. Olson, R. T. Collins, and D. S. Ginley. “Ultrasonic spray deposition for production of organic solar cells.” Solar Energy Mater. Solar Cells **93**, 447 (2009).

24. C. J. Curtis, M. van Hest, A. Miedaner, J. Nekuda, P. Hersh, J. Leisch, and D. S. Ginley. “Spray deposition of high quality $CuInSe_2$ and CdTe films.” In Proc. IEEE Photovolt. Special. Conf. **33**, 1065 (2008).

25. S. Buecheler, D. Corica, D. Guettler, A. Chirila, R. Verma, U. Müller, T. P. Niesen, J. Palm, and A. N. Tiwari. “Ultrasonically sprayed indium sulfide buffer layers for $Cu(In,Ga)(S,Se)_2$ thin-film solar cells.” Thin Solid Films, **517**, 2312 (2009).

26. Z. Chen, P. Liu, C. Yu, Y. Ren, and K. Shum. “Solution-based synthesis and characterization of $CsSnI_3$ thin films.” Submitted.

27. H. O. Pierson. “Handbook of Chemical Vapor Deposition: Principles, Technology and Applications.” William Andrew, New York (1999).

28. A. Sherman. “Chemical Vapor Deposition for Microelectronics: Principles, Technology, and Applications.” Noyes, New York (1987).

29. K. L. Choy. “Chemical vapour deposition of coatings.” Prog. Mater. Sci. **48**, 57 (2003).

30. R. Gordon. “Chemical vapor deposition of coatings on glass.” J. non-cryst. solids **218**, 81 (1997).

31. M. L. Hammond. “Introduction to Chemical Vapor Deposition.” Solid State Technol. **22**, 61 (1979).

32. H. Xiao. “Introduction to Semiconductor Manufacturing Technology.” Upper Saddle River: Prentice Hall, New Jersey (2001).

33. J. M. Hollas. “Modern Spectroscopy.” Wiley, New York (2004).

34. D. C. Harris and M. D. Bertolucci. “Symmetry and Spectroscopy: An Introduction to Vibrational and Electronic Spectroscopy.” Dover Publications, New York (1989).

35. P. F. Bernath. “Spectra of Atoms and Molecules.” Oxford University Press, USA (2005).

36. D. A. Skong and D. M. West. “Principles of Instrumental Analysis.” Saunders College, Philadelphia PA (1980).

37. J. M. Palmer and B. G. Grant. “The Art of Radiometry.” SPIE Publications, USA (2009).

38. R. Paschotta. “Encyclopedia of Laser Physics and Technology.” Wiley-VCH, USA (2008).

39. L. A. Whitehead and M. A. Mossman. “Jack O'Lanterns and integrating spheres: Halloween Physics.” Amer. J. Phys. **74**, 537–541 (2006).

40. A. Ducharme, A. Daniels, E. Grann, and G. Boreman. “Design of an integrating sphere as a uniform illumination source.” Education, IEEE Transactions on **40**, 131 (1997).

41. P. Nostell, A. Roos, and D. Rönnow. “Single-beam integrating sphere spectrophotometer for reflectance and transmittance measurements versus angle of incidence in the solar wavelength range on diffuse and specular samples.” Rev. Sci. Instrum. **70**, 2481 (1999).

42. F. J. J. Clarke and J. A. Compton. “Correction methods for integrating-sphere measurement of hemispherical reflectance.” Color Res. Appl. **11**, 253 (2007).

43. Application Note: “Quantitation of Single Beam Substitution Correction in Reflectance Spectroscopy Accessories.” Labsphere, New Hampshire (1998).

44. A. D. McNaught and A. Wilkinson. “Compendium of Chemical Terminology.” Blackwell Science, Oxford (1997).

45. G. A. Crosby and J. N. Demas. “The Measurement of Photoluminescence Quantum Yields. Review.” J. Phys. Chem. **75**, 991 (1971).

46. K. Bohm and B. Fischer. “Photoluminescence at dislocations in GaAs and InP.” J. Appl. Phys. **50**, 5453 (1979).

47. D. D. Sell, S. E. Stokowski, R. Dingle, and J. V. DiLorenzo. "Polariton reflectance and photoluminescence in high-purity GaAs." Phys. Rev. B **7**, 4568 (1973).

48. B. Monemar. "Fundamental energy gap of GaN from photoluminescence excitation spectra." Phys. Rev. B **10**, 676 (1974).

49. H. Ennen, J. Wagner, H. D. Müller, and R. S. Smith. "Photoluminescence excitation measurements on GaAs:Er grown by molecular - beam epitaxy." J. Appl. Phys. **61**, 4877 (1987).

50. J. F. Ryan, R. A. Taylor, A. J. Turberfield, A. Maciel, J. M. Worlock, A. C. Gossard, and W. Wiegmann. "Time-resolved photoluminescence of two-dimensional hot carriers in GaAs-AlGaAs heterostructures." Phys. Rev. lett. **53**, 1841 (1984).

51. D. C. Reynolds, D. C. Look, B. Jogai, J. E. Hoelscher, R. E. Sherriff, M. T. Harris, and M. J. Callahan. "Time-resolved photoluminescence lifetime measurements of the Γ 5 and Γ 6 free excitons in ZnO." J. Appl. Phys. **88**, 2152 (2000).

52. E. E. Nyein, U. Hommerich, J. Heikenfeld, D. S. Lee, A. J. Steckl, and J. M. Zavada. "Spectral and time-resolved photoluminescence studies of Eu-doped GaN." Appl. Phys. Lett. **82**, 1655 (2003).

53. K. W. Sun, A. Kechiantz, B. C. Lee, and C. P. Lee, "Ultrafast carrier capture and relaxation in modulation-doped InAs quantum dots." Appl. Phys. Lett. **88**, 163117 (2006).

54. W. K. Metzger, D. Albin, D. Levi, P. Sheldon, X. Li, B. M. Keyes, and R. K. Ahrenkiel. "Time-resolved photoluminescence studies of CdTe solar cells." J. Appl. Phys. **94**, 3549 (2003).

55. M. Paillard, X. Marie, E. Vanelle, T. Amand, V. K. Kalevich, A. R. Kovsh, A. E. Zhukov, and V. M. Ustinov. “Time-resolved photoluminescence in self-assembled InAs/GaAs quantum dots under strictly resonant excitation.” Appl. Phys. Lett. **76**, 76 (2000).

56. A. Yamamoto, T. Kido, T. Goto, Y. Chen, T. Yao, and A. Kasuya. “Time-resolved photoluminescence in ZnO epitaxial thin films studied by up-conversion method.” J. Cryst. Growth **214-215**, 308 (2000).

57. K. Shum, Y. Takiguchi, J. M. Mohaidat, R. R. Alfano, K. Adomi, and H. Morkoc. “Effect of valence-subband structure on the energy relaxation dynamics of electrons in GaAs quantum wells grown on Si.” Phys. Rev. B **44**, 4044 (1991).

58. K. Shum, Y. Takiguchi, J. M. Mohaidat, F. Liu, and R. R. Alfano. “Picosecond hole dynamics in GaAs grown on silicon.” Appl. Phys. Lett. **56**, 2328 (1990).

59. W. K. Metzger, R. K. Ahrenkiel, P. Dippo, J. Geisz, M. W. Wanlass, and S. Kurtz. “Time-resolved photoluminescence and photovoltaics.” NREL/CP-520-37028, 5 (2005).

60. K. Okamoto, I. Niki, A. Scherer, Y. Narukawa, T. Mukai, and Y. Kawakami. “Surface plasmon enhanced spontaneous emission rate of InGaN/GaN quantum wells probed by time-resolved photoluminescence spectroscopy.” Appl. Phys. Lett. **87**, 071102 (2005).

61. K. C. A. Smith, and C. W. Oatley. “The scanning electron microscope and its fields of application.” Brit. J. Appl. Phys. **6**, 391 (1955).

62. M. A. Hayat. “Principles and Techniques of Scanning Electron Microscopy: Biological Applications.” Van Nostrand Reinhold, New Jersey (1975).

63. R. Egerton. “Physical principles of electron microscopy: an introduction to TEM, SEM, and AEM.” Springer, New York (2005).

64. R. D. Heidenreich. “Fundamentals of transmission electron microscopy.” Interscience Publishers, New York (1964).

65. E. Zeitler and M. G. R. Thomson. “Scanning transmission electron microscopy.” Optik **31**, 359 (1970).

66. A. V. Crewe, J. Wall, and L. M. Welter. “A High-Resolution Scanning Transmission Electron Microscope.” J. Appl. Phys. **39**, 5861 (1968).

67. G. Thomas and M. J. Goringe. “Transmission Electron Microscopy of Materials.” Wiley, New York (1979).

68. B. E. Warren. “X-ray Diffraction.” Courier Dover Publications, New York (1969).

69. H. P. Klug and L. E. Alexander. “X-Ray Diffraction Procedures: For Polycrystalline and Amorphous Materials, 2nd Edition.” Wiley-Interscience, New York (1974).

70. C. P. Gazzara and D. R. Messier. “Determination of phase content of Si_3N_4 by X-ray diffraction analysis.” Amer. Ceram. Soc. Bull. **56**, 777 (1977).

71. D. M. Moore and R. C. Reynolds. “X-ray diffraction and the identification and analysis of clay minerals.” Oxford University Press, USA (1989).

72. J. I. Pankove. “Optical Processes in Semiconductors.” Dover, New York (1971).

73. Z. Chen, C. Yu, K. Shum, J. J. Wang, W. Pfenninger, N. Vockic, J. Midgley, and J. T. Kenney. "Photoluminescence study of polycrystalline $CsSnI_3$ thin films: Determination of exciton binding energy." J. lumin.**132**, 345 (2012).

74. G. H. Wannier. "The Structure of Electronic Excitation Levels in Insulating Crystals." Phys. Rev. **52**, 191 (1937).

75. G. W. Hooft, W. A. J. A. Van der Poel, L. W. Molen, and C. T. Foxon. "Giant oscillator strength of free excitons in GaAs." Phys. Rev. B **35**, 8281 (1987).

76. H. Deng, G. Weihs, D. Snoke, J. Bloch, and Y. Yamamato. "Polariton Lasing vs. Photon Lasing in a Semiconductor Microcavity." PNAS **100**, 15318 (2003).

77. S. Christopoulos, G. Baldassarri Höger von Högersthal, A. J. D. Grundy, P. G. Lagoudakis, A. V. Kavokin, and J. J. Baumberg. "Room-Temperature Polariton Lasing in Semiconductor Microcavities." Phys. Rev. Lett. **98**, 126405 (2007).

78. S. Chu, M. Olmedo, Z.Yang, J. Kong, and J. Liu. "Electrically pumped ultraviolet ZnO diode lasers on Si." Appl. Phys. Lett. **93**, 181106 (2008).

79. D. A. B. Miller, D. S. Chemla, T. C. Damen, A. C. Gossard, W. Wiegmann, T. H. Wood, and C. A. Burrus. « Band-Edge Electroabsorption in Quantum Well Structures : The Quantum-Confined Stark Effect." Phys. Rev. Lett. **53**, 2173 (1984).

80. E. A. De Soza, L. Carraresi, G. D. Boyd, and D. A. B. Miller. "Analog differential self-linearized quantum-well self-electro-optic-effect modulator." Optics Lett. **18**, 974 (1993).

81. H. Haug and S. W. Koch. "Quantum Theory of the Optical and Electronic Properties of Semiconductor." World Scientific, Singapore (1990).

82. D. C. Reynolds and T. C. Collins. “Excitons: their Properties and Uses.” Academic Press, New York (1981).

83. D. D. Sell. “Resolved Free-Exciton Transitions in the Optical-Absorption Spectrum of GaAs.” Phys. Rev. B **6**, 3750 (1972).

84. D.W. Hamby, D.A. Lucca, M.J. Klopfstein, and G. Cantwell. “Temperature dependent exciton photoluminescence of bulk ZnO.” J. Appl. Phys. **93**, 3214 (2003).

85. P. Misra, T.K. Sharma, L. M. Kukreja. “Temperature dependent photoluminescence processes in ZnO thin films grown on sapphire by pulsed laser deposition.” Curr. Appl. Phys. **9**, 179 (2009).

86. W. Shan, X. C. Xie, J. J. Song, B. Goldenburg. “Time-resolved exciton luminescence in GaN grown by metalorganic chemical vapor deposition.” Appl. Phys. Lett. **67**, 2512 (1995).

87. L. Eckey, J. –Ch. Holst, P. Maxim, R. Heitz, A. Hoffmann, I. Broser, B. K. Meyer, C. Wetzel, E. N. Mokhov, and P. G. Baranov. “Dynamics of bound – exciton luminescences from epitaxial GaN.” Appl. Phys. Lett. **68**, 415 (1996).

88. J.R. Haynes. “Experimental Proof of the Existence of a New Electronic Complex in Silicon.” Phys. Rev. Lett. **4**, 361 (1960).

89. F. A. Settle. “Instrumental Techniques for Analytical Chemistry.” Upper Saddle River: Prentice Hall, New Jersey (1997).

90. T. Schweizer, D. W. Hewak, B. N. Samson, and D. N. Payne. "Spectroscopic data of the 1.8-, 2.9-, and 4.3-μm transitions in dysprosium-doped gallium lanthanum sulfide glass." Opt. Lett. **21**, 1594 (1996).

91. R. R. Mattews and L. A. Melton. "Determination of carbon in trichlorosilane by metastable transfer emission spectrometry." Anal. Chem. **58**, 807 (1986).

92. W. J. Moore, J. A. Freitas, G. C. B. Braga, R. J. Molnar, S. K. Lee, K. Y. Lee, and I. J. Song. "Identification of Si and O donors in hydride-vapor-phase epitaxial GaN." Appl. Phys. Lett. **79**, 2570 (2001).

93. K. Tanaka, T. Takahashi, T. Kondo, T. Umebayashi, K. Asai, and K. Ema. "Image charge effect on two-dimensional excitons in an inorganic-organic quantum-well crystal." Phys. Rev. B **71**, 045312 (2005).

94. G. Lanty, J. S. Lauret, E. Deleporte, S. Bouchoule, and X. Lafosse. "UV polaritonic emission from a perovskite-based microcavity." Appl. Phys. Lett. **93**, 081101 (2008).

95. S. Zhang, G. Lanty, J. –S. Lauret, E. Deleporte, P. Audebert, and L. Galmiche. "Synthesis and optical properties of novel organic-inorganic hybrid nanolayer structure semiconductors." Acta Mater. **57**, 3301 (2009).

96. C. Keffer, T. M. Hayes, and A. Bienenstock. "PbTe Debye-Waller Factors and Band-Gap Temperature Dependence." Phys. Rev. Lett. **21**, 1676 (1968).

97. A. Göbel, T. Ruf, M. Cardona, C. T. Lin, J. Wrzesinski, M. Steube, K. Reimann, J. -C. Merle, and M. Joucla. "Effects of the isotopic composition on the fundamental gap of CuCl." Phys. Rev. B **57**, 15183 (1998).

98. H. J. Lian, A. Yang, M. L. W. Thewalt, R. Lauck, and M. Cardona. “Effects of sulfur isotopic composition on the band gap of PbS.” Phys. Rev. B **73**, 233202 (2006).

99. K. Shum, Z. Chen, J. Qureshi, C. Yu, J. J. Wang, W. Pfenninger, N. Vockic, J. Midgley, and J. T. Kenney. “Synthesis and characterization of $CsSnI_3$ thin films.” Appl. Phys. Lett. **96**, 221903 (2010).

100. I. Chung, B. Lee, J. He, R. P. H. Chang, and M. G. Kanatzidis. “All-solid-state dye-sensitized solar cells with high efficiency.” Nature **485**, 486 (2012).

101. L. J. A. Koster, V. D. Mihailetchi, R. Ramaker, and P. W. M. Blom. “Light intensity dependence of open-circuit voltage of polymer: fullerene solar cells.” Appl. Phys. Lett., **86**, 123509 (2005).

102. R. Kind, R. A. C. M. M. van Swaaij, F. A. Rubinelli, S. Solntsev, and M. Zeman. “Thermal ideality factor of hydrogenated amorphous silicon p-i-n solar cells.” J. Appl. Phys. **110**, 104512 (2011).

103. C. van Berkel, M. J. Powell, A. R. Franklin, and I. D. French. “Quality factor in a – Si:H nip and pin diodes.” J. Appl. Phys. **73**, 5264 (1993).

104. I. Chung, J. -H. Song, J. Im, J. Androulakis, C. D. Malliakas, H. Li, A. J. Freeman, J. T. Kenney, and M. G. Kanatzidis. “CsSnI3: Semiconductor or metal? High electrical conductivity and strong near-infrared photoluminescence from a single material. High hole mobility and phase-transitions.” J. Am. Chem. Soc. **134**, 8579 (2012).